UNIVERSITY OF CALIFORNIA, IRVINE

MINATURIZED PLATFORMS FOR ANALYZING MITOCHONDRIAL BIOENERGETICS

DISSERTATION

submitted in partial satisfaction of the requirements for the degree of

DOCTOR OF PHILOSOPHY

in Biomedical Engineering

by

Ted Dong-Anh Pham

Dissertation Committee
Professor Peter Burke, Chair
Professor Abraham Lee
Professor William Tang

2016

TABLE OF CONTENTS

LIST OF FIGURES

LIST OF TABLES

LIST OF ABBREVIATIONS

$\Delta\Psi_m$ – mitochondrial membrane potential

ADP – adenosine diphosphate

AFM – atomic force microscope

APTES - (3-Aminopropyl)triethoxysilane

ATP – adenosine triphosphate

BSA – Bovine serum albumin

C – Centigrade

CCCP - Carbonyl cyanide *m*-chlorophenyl hydrazone

CCD – charge-coupled device

CNT – carbon nanotube

CNTFET – carbon nanotube field effect transistor

DMSO –dimethyl sulfoxide solution

DNA – deoxyribonucleic acid

ETC – electron transport chain

Heb7A – HeLa-derived cell line

HMDS – Hexamethyldisilazane

IPA – Isopropanol

ISE – ion-selective electrode

min – minute

MMP – mitochondrial membrane permeabilization

MTG – MitoTracker Green

mtDNA – mitochondrial DNA

mtPTP – mitochondrial permeability transition pore

NADH – nicotinamide adenine dinucleotide (reduced)

ND1 and ND2 – NADH dehydrogenase subunit 1 and 2

OXPHOS – oxidative phosphorylation

PDMS - Polydimethylsiloxane

Pi – inorganic phosphate

PM – pyruvate and malate

PTP – permeability transition pore

PVC – Polyvinyl chloride

redox – reduction-oxidation

ROS – reactive oxygen species

Si- Silicon

SNR – signal to noise ratio

SWCNT – single walled carbon nanotube

THF - Tetrahydrofuran

TMRE – tetramethylrhodamine ethyl ester

TMRM – tetramethylrhodamine methyl ester

TPP^+ - tetraphenylphosphonium

ACKNOWLEDGEMENTS

I would like to thank my thesis advisor, Professor Peter Burke, for his continual support, insight, and motivation. I also wish to express my gratitude to Professor Douglas Wallace and Dr. Anthony Letai for their invaluable inputs. I would like to thank my committee members, for their valuable discussions and advices on my dissertation.

The members of UCI NanoBio Lab have contributed immensely to my time at UC Irvine. The group has been a source of friendships as well as good advice and collaboration. Thanks to Tae-Sun Lim, Katie Zand, Will Wang, Weiwei Zhou, Phi Pham and Jinfeng Li. I am also grateful to the team at INRF and CalIT2.

Lastly, I dedicate this thesis to my parents, sister, brothers and sisters-in-law for all their love and encouragement and most importantly my amazing wife, Hoa, without whose constant support, understanding and unconditional love, I never would have finished this work.

CURRICULUM VITAE

Ted Dong-Anh Pham

2009 B.S. in Electrical Engineering, University of California, Los Angeles
Cum laude, School of Engineering Scholarship

2014 M.S. in Biomedical Engineering, University of California, Irvine

2016 Ph.D. in Biomedical Engineering
NSF IGERT Lifechips and Department of Education GAAN fellowships

Field of Study

Microscale Biosensors of Mitochondrial Functions

ABSTRACT OF THE THESIS

Miniaturized Platforms for Analyzing

Mitochondrial Bioenergetics

by

Ted Pham

Doctor of Philosophy in Electrical Engineering and Computer Science

University of California, Irvine, 2016

Professor Peter Burke, Chair

Mitochondrial bioenergetics converges at the mitochondrial inner membrane and encompasses the proton gradient, mitochondrial membrane potential and respiration. Measuring these parameters can assess the mitochondrial functional state and consequently, the effectiveness of pharmacological manipulation of diseases involving mitochondrial dysfunctions. However, available technologies to assay mitochondrial functions are primarily limited to ensemble measurements, which mask the functional dynamics and variability of single mitochondria. These dynamics could provide a better understanding of mitochondrial bioenergetics and diseases related to mitochondrial dysfunctions. This thesis describes three developments to improve mitochondrial functional assays, with an ultimate goal of achieving single mitochondrial resolution.

The first development is single mitochondrial respirometers that require only 1.5 pL of assay buffer and can measure respiration from one mitochondrion. The micro-respirometers consist of micron sized chambers etched out of glass substrates and coated with an oxygen sensitive phosphorescent dye Pt(II) meso-tetra(pentafluoropheny)porphine (PtTFPP). Sealing the chambers

with a polydimethylsiloxane layer coated with oxygen impermeable Viton rubber enables detection of single mitochondrial respiration.

The second development is the fabrication of nanochannels capable of trapping single mitochondria for fluorescence analysis of their membrane potential. The use of these channels significantly reduces background noise and allows the ease of experimental buffer exchange. Experimental results show fluctuations of membrane potential at the single mitochondrial level.

Finally, an integrated platform to detect extra-mitochondrial pH of isolated mitochondria is described. This platform was based on tethering mitochondria to one-atom thin graphene. The mitochondria are tethered via graphene bound antibodies, which recognize the mitochondrial outer membrane protein TOM20. Graphene is an excellent conductor and changes in the pH surrounding the mitochondria can change the graphene conductance and can be detected electrically. Being transparent, the graphene layer also permits optical interrogation of the mitochondria concurrent with the analysis of pH. Hence, this system permits the simultaneous monitoring of changes in extra-mitochondrial pH through graphene conductance and inner membrane potential using fluorescence. In addition, the integrated graphene system offers a unique scalability down to one mitochondrion without loss of electrical sensitivity.

CHAPTER 1: INTRODUCTION

Mitochondrial Bioenergetics

The mitochondrion possesses an inner membrane specialized for energy transduction. This unique capability stems from the membrane's exquisite impermeability to protons and a collection of densely packed proteins of oxidative phosphorylation (Figure 1.1). Among these proteins are the complexes and electron carriers of the electron transport chain, which stepwise extract energy from high potential electrons by transferring them through one complex to the next and to the terminal receiver oxygen.

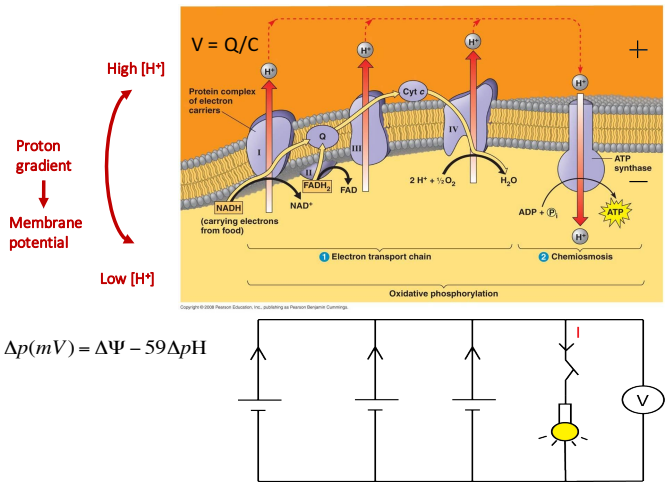

Figure 0.1: Overview of the mitochondrial electrical circuit

Using the extracted energy, complex I, III, and IV translocate protons out of the inner membrane space i.e. from the matrix to the inter membrane space, creating a proton gradient across the inner membrane. Due to the low capacitance and proton impermeability of the lipid bilayer membrane, the proton gradient (or charge separation) creates a potential difference or mitochondrial membrane potential. The proton gradient and the membrane potential make up the proton motive force which provides a favorable passive force for protons to flow back to the inner membrane through complex V ATP synthase whenever the complex is open. At this complex, the energy derived the protons movement turns into mechanical and chemical energy to drive the synthesis ATP from ADP and Pi. Electron transport chain and ATP synthase is tightly

coupled, meaning the electron transport chain cannot run unless there is a demand for ATP synthesis or the availability of ADP and Pi. However, when there is no demand for ATP or there is no ADP available, the proton leak across the inner membrane dictates the rate of the electron transport chain. Shown in Figure 1.1 is a simple representation of the ETC and ATP synthase along with mobile electron carriers ubiquinone and cytochrome c. An analogous electrical circuit is also shown in figure 1.1[1]. The voltagQe source represents the proton motive force across the membrane, indicating the potential to do work while the light bulb models the ATP synthase complex which provide a pathway for the flow of current and power consumption. From the simple circuitry, to accurately quantify the functional states of a mitochondrion requires the measurements of both the voltage and the current. In other words, one would need a compatible voltmeter and ammeter to assess the functional states a mitochondria. As in any circuit, knowledge of the current is more informative than voltage.

Most of what we know about mitochondria has been obtained from studying the organelles in isolated forms. The ability to control the substrate level and add various inhibitors of the electron transport chain and ATP Synthase has been invaluable. In term of respiration for isolated mitochondria, Chance and Williams[2] defined the five respiration states for isolated mitochondria (table 1). By measuring the oxygen consumption rate of different states, metrics can be calculated to analyze the functional response of the investigated mitochondria.

Factors	State 1	State 2	State 3	State 4	State 5
Oxygen	Present	Present	Present	Present	Absent
ADP level	Low	High	High	Low	High
Substrate level	Endogenous - low	Approaching 0	High	High	High
Respiration Rate	Slow	Slow	Fast	Slow	Absent
Rate-limiting factor	Phosphate Acceptor	Substrate	Respiratory chain	Phosphate Acceptor	Oxygen

Table 0.1: State of respiration for isolated mitochondria

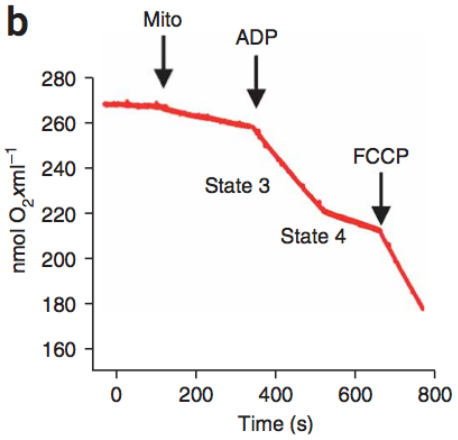

Figure 0.2: A typical respiration measurement

For example, respiratory control ratio (RCR), measured as the oxygen consumption rate of state 3 over state 4, is usually used to indicate the quality of coupling for a mitochondrial preparation. An example in Figure 1.2, adapted from [3] shows an approximate RCR of 3. Another parameter is the P/O ratio, which specifies the amount of ATP produced per oxygen molecule. Using these parameters and a set of substrates and inhibitors of oxidative phosphorylation (will be detailed in Methods), mitochondrial functions or lack thereof can be pinpointed to one of the individual OXPHOS protein complex.

The roles of mitochondria in controlling programmed cell death or apoptosis has recaptured researchers' attention and studies on mitochondrial bioenergertics during apoptosis are underway. This thesis aim to developed improved technologies to study the various aspects of mitochondrial dynamics, namely respiration, membrane potential and pH.

The Principles of Oxygen sensing

Predominant biological oxygen sensing techniques comprise Clark-type oxygen electrodes and oxygen-quenched luminescent probes. Oxygen sensors based on Clark-type oxygen electrode relies on the amperometric electrochemical reaction between a coated Pt-electrode and dissolved molecular oxygen. In other words, these sensors detect oxygen concentrations by reducing the analyte at the electrode interface, and in effect producing a proportional current to a reference electrode[4]. Even though commercial systems[3,5,6] based on Clark-type oxygen electrodes are commonly used to obtain a polarographic curve for respiration in isolated mitochondria, whole cells, and tissues, the use of Clark-type electrodes can be unsuitable toward integrated miniature systems and low oxygen concentrations (an aim of this proposal). The difficulties in miniaturizing the electrodes arise from the facts that the electrodes themselves consume oxygen, resulting in loss of the analyte, reduced sensitivity, and signal inconsistencies, that at small scales the electrode drifts and membrane fouling are both significant, and that incorporated flows interfere with the electrodes and cause signal variation[7]. Furthermore, even though integrated and planar Clark-type electrodes have been demonstrated[8], the requirement of a reference electrode demands device estate and limits how small the system can be.

In contrast, oxygen-sensitive luminescent probes do not consume oxygen and offer advantages toward miniaturization for biomedical applications. Besides nonchemical interaction with oxygen, these probes offer fast response times down to miliseconds, high sensitivity and specificity[9], and demonstrated compatibility with biological samples[10]. The sensing principle of the oxygen-sensitive luminescent probes is based on the dynamic quenching of the dyes' luminescent intensity and lifetime[11]. Specifically, oxygen molecules collide with the

luminophores, deactivating them from their lowest excited state to the ground state[12]. The relationship of this quenching effect is described by the Stern-Volmer equation:

$$\frac{I_o}{I} = \frac{\tau_o}{\tau} = 1 + K_{sv}[O_2] \qquad (Eqn. 1)$$

I_o and τ_o are the reference values in the absence of oxygen, whereas I and τ are the measured intensity and lifetime. The ratio of $\frac{I_0}{I}$ and $\frac{\tau_0}{\tau}$ are expressed linearly in terms of the Stern-Volmer constant K_{sv} and the concentration of O_2 in the solution. Equation 1 is alternatively expressed in terms of the partial pressure of oxygen, which is related to the concentration of O_2 in solution via Henry's law. Typical oxygen assays based on luminescent dyes will begin with constructing a calibration curve for 3 to 5 different concentrations of oxygen with the choice of detected signal of either luminescent intensity or lifetime. If the selected measurement is intensity, the problems with photobeaching and optical interference from biological samples should be considered. As the probe's luminescence degrades after repeated exposure with excitation light source, the intensity-correlated measurement of oxygen concentration becomes unreliable. The use of a concurrent oxygen-insensitive dye has been employed to compensate for photobleaching[13]. Conversely, luminescent lifetime is immune from photobleaching and optical interference because the lifetime, which is the average time the luminophore stays in the excited state, is an inherent property of each probe. The choice of an oxygen optical probe rests significantly on this inherent lifetime of exponential signal decay. The tradeoff here is between lifetime i.e. response time and sensitivity: longer lifetimes often mean higher sensitivity but will result in longer response times[12].

Besides lifetime, another criterion to choosing an appropriate luminescent probe is whether the probe is in solid state or water-soluble. Although water-soluble probes are quite easy

to use and can penetrate the cells to report intracellular oxygen, solid state probes are more promising as to measure the absolute oxygen consumption rate from extracellular or extra mitochondrial environments without interfering with the physiological activities of the cell or the mitochondrion under investigation. For solid-state dyes, a Pt-porphyrin is usually incorporated with polystyrene and deposited on a solid surface. Chapter 1 describes microrespirometers with the phosphorescent solid state sensor PtTFPP for the measurement of single mitochondrial respiration.

Principles of Membrane Potential Measurement

The mitochondrial inner membrane potential can be measured with lipophilic cations whose distribution across the inner membrane is governed by the Nernst equation in accordance with the membrane potential. The readout mode depends on the cation used. On one hand, with probes analogous to tetraphenylphosphonium (TPP+), ion selective electrode can monitor the TTP concentration outside, which can be carefully calibrated to the membrane potential. On the other hand, fluorescence readout can monitor both the inside and outside distribution of fluorescent stains that can distribute themselves across the inner membrane. Some stains such as JC-1 yield dual color depending on the magnitude of the membrane potential e.g. green means low while red indicate high. For these dyes, the ratio of emission colors is often used. Other stains such as TMRE and TMRM only emit one color but careful measurement of the inside and outside fluorescence intensity can give a quantitative analysis of the potential. However, the inside intensity is often used as a sufficient qualitative metric. Tradditional methods in studying the inner membrane potential suffer from high background noise and require large sample size. Chapter 2 describes a new method to assay the membrane potential.

The principles of pH sensing

The pH levels at the intermembrane space and inside the matrix can be monitored with genetically encoded mitochondrial pH sensors. Fluorescence microscopy is used to calibrate and measure the pH reported by these sensors and the time as well as pH resolutions primarily depends on the detection system e.g. spinning confocal microscope has significant higher resolution than an inverted microscope. These probes have been used to elucidate the pH difference between the mitochondrial compartments. However, uncertainties in the fluorescence calibration have led to different opinions about the role of pHs during apoptosis. In addition, these probes are limited to established transformed cell lines.

Other pH sensors based on field effective sensing and nano-material have been demonstrated[14–16]. From the Nernst equation, the theoretical sensitivity of a pH sensing surface is around 60 mV/pH. Our computed sensitivity is 8 mV/pH. This limit is, however, not directly related to the detection limit of the platform. The detection limit cannot be computed without accurate noise measurements[17]. To complicate that matter further, while higher sensitivity in terms of mV/pH is generally desired for higher pH resolution, lower mV/pH lowers the charge threshold for detection[18]. Collectively, while the pH sensitivity of semiconducting materials and graphene are promising in biosensing applications, the criterion to assess their performance is still a matter of further research.

Chapter 4 explores and demonstrates the use of graphene in detecting extramitochondrial pH during apoptosis.

CHAPTER 2: MICROCHAMBERS WITH SOLID-STATE PHOSPHORESCENT SENSOR FOR MEASURING SINGLE MITOCHONDRIAL RESPIRATION

Overview

It is now well established that, even within a single cell, multiple copies of the mitochondrial genome may be present (genetic heteroplasmy). It would be interesting to develop techniques to determine if and to what extent this genetic variation results in functional variation from one mitochondrion to the next (functional heteroplasmy). Measuring mitochondrial respiration can reveal the organelles' functional capacity for Adenosine triphosphate (ATP) production and determine mitochondrial damage that may arise from genetic or age related defects. However, available technologies require significant quantities of mitochondria. Here, we develop a technology to assay the respiration of a single mitochondrion. Our "micro-respirometer" consists of micron sized chambers etched out of borofloat glass substrates and coated with an oxygen sensitive phosphorescent dye Pt(II) meso-tetra(pentafluorophenyl)porphine (PtTFPP) mixed with polystyrene. The chambers are sealed with a polydimethylsiloxane layer coated with oxygen impermeable Viton rubber to prevent diffusion of oxygen from the environment. As the mitochondria consume oxygen in the chamber, the phosphorescence signal increases, allowing direct determination of the respiration rate. Experiments with coupled vs. uncoupled mitochondria showed a substantial difference in respiration, confirming the validity of the microchambers as single mitochondrial respirometers. This demonstration could enable future high-throughput assays of mitochondrial respiration and benefit the study of mitochondrial functional heterogeneity, and its role in health and disease.

Introduction

Mitochondria play a multitude of roles in cell life and death[19–21]. In cell life, mitochondria produce the majority of cellular energy Adenosine triphosphate (ATP) and sequester harmful reactive oxygen species; in cell death, mitochondria play an active role in the so-called

"intrinsic" pathway of apoptosis or programmed cell death[21,22]. It logically follows that mitochondrial dysfunctions resulting in defective energy metabolism and resistance to apoptosis have been linked to various disorders such as Alzheimer's disease, cardiovascular diseases, diabetes, Parkinson's disease, and cancer [23]. To assess mitochondrial dysfunction, current state-of-the-art experiments often report the mitochondrial respiration rate because it directly reflects the functional status and the health of the mitochondrion [24].

Convincing evidence exists that mitochondria have genetic heteroplasmy at multiple levels: as an organism ages, genetic (especially mitochondrial DNA based) defects in mitochondrial function become more prevalent, resulting in a heterogeneous distribution of mitochondrial DNA within the organism and within a given tissue [25]. During germline maturation, defective mitochondria are screened through unknown mechanisms to prevent offsprings from carrying serious mutations [26]. While technologies for assaying genetic variation among mitochondria are relatively mature [27,28], technologies to measure *functional* heteroplasmy are still lacking. One of the most significant functional assays, the quantification of the oxygen consumption rate, is usually reported as an average of thousands of cells or isolated mitochondria[24,29]; hence, the dynamics and variability of respiration rate from single cells or single mitochondria are lost. Furthermore, rare cell behavior such as stem cells or circulating tumor cells [25,30,31] is masked in such an ensemble approach.

To this end, we have developed a technology to assay the respiration of a single mitochondrion. Our "micro-respirometer" consists of micron sized chambers etched out of borofloat glass substrates and coated with an oxygen sensitive phosphorescent dye Pt(II)-meso-tetra(pentafluorophenyl)porphine (PtTFPP) mixed with polystyrene. The chambers are sealed with a polydimethylsiloxane (PDMS) layer coated with oxygen impermeable Viton rubber to prevent

diffusion of oxygen from the environment. As the mitochondria consume oxygen in the chamber, the phosphorescence signal increases, allowing direct determination of the respiration rate. Experiments with coupled vs. uncoupled mitochondria showed a significant difference in respiration, confirming the validity of the microchambers as single mitochondrial respirometers. This demonstration could enable future high-throughput assays of mitochondrial respiration and benefit the study of mitochondrial functional heterogeneity, and its role in health and disease.

Materials and Methods

Mitochondrial Isolation

The mammalian cell line HeLa (American Type Cell Culture) was maintained in the log growth phase using minimum essential medium (MEM) supplemented with 10% fetal bovine serum (FBS). All cell culture related supplies were obtained from Thermofisher Scientific (Waltham, USA). 10^7 cells were typically harvested for mitochondria isolation.

Before isolation, the confluent cells were stained with 100 nM MitoTracker Green FM for one hour. The cells were then washed with fresh media. Our complete isolation buffer contains 225 mM mannitol, 75 mM sucrose, 0.5 mM EGTA, 20 mM HEPES, 0.5% (*w*/*v*) Bovine Serum Albumin (BSA), 1X protease inhibitor, pH 7.2 with 1 M KOH. All buffer chemicals were purchased from Sigma Aldrich (Saint Louis, USA). The stock isolation buffer was prepared without BSA and protease inhibitor and stored at 4 °C. Mitochondria from the cultured cells were isolated using differential centrifugation. After collection, the cells were transferred to a glass homogenization tube in 3 mL complete isolation buffer and homogenized with 30 strokes on ice. The cells were then transferred into 2-mL Eppendorf tubes and centrifuged at a low speed of 2000 × *g* for 4 min at

4 °C. The resulting supernatant was collected and centrifuged at a high speed of 12,000 × *g* × 10

min at 4 °C. The supernatant as well as the light-colored fluffy sediment containing damaged mitochondria were aspirated and the resulting pellet was resuspended in respiration buffer (140 mM KCl, 2 mM $MgCl_2$, 10 mM NaCl, 0.5 mM EGTA, 0.5 mM KH_2PO_4, 2 mM HEPES, 5 mM succinate,

2 μM rotenone, pH 7.2 adjusted with KOH). However, for mitochondria protein analysis, the mitochondria were resuspended in KCl buffer without EGTA. The protein analysis was done with BCA assay kit supplied by Thermo Fisher Scientific, and the result indicated a typical yield of 140 μg mitochondrial protein. As a quality control, we used a Hansatech Oxytherm to measure the respiratory control ratio of a typical mitochondrial preparation with this protocol and found the ratio to be around 3.1,which is good for cultured cells [32].

Microchambers Fabrication

Borofloat glass wafers (3″ × 3″ × 0.7 mm) with a pre-deposited 120 nm Cr layer were supplied by TELIC Company (Valencia, USA). On top of the Cr layer, there was also a 530 nm preprocessed layer of AZ1500 positive photoresist. Using photolithography, Cr etching, and 48% HF wet etching, we created microchambers in the borofloat glass substrate with a depth of 7.5 μm and a surface diameter of 15 μm. The chamber's depth was measured by a Dektak 3 surface profilometer.

The oxygen-sensitive dye was obtained from Frontier Scientific (Logan, USA) (Catalog # PtT975) and was incorporated with polystyrene (PS), average M_w 280,000 Sigma Aldrich (Saint Louis, USA) (Catalog# 182427). The PtTFPP/PS oxygen sensing mixture was prepared in toluene with 150 μM PtTFPP and 64 μM PS final concentrations. A few drops of this mixture were quickly transferred onto the substrate containing the microchambers using a cotton swab and the wafer was heated at 120 °C for 1 min. Immediately after the wafer was sufficiently

cooled, we used scotch tape to extract the dye from the wafer surface, leaving PtTFPP only at the bottoms of the microchambers. Due to the capillary effect [33], the deposited dye formed a ring around the bottom of each chamber.

PDMS and Viton-Coated Top Insulating Layer

PDMS was prepared according to the manufacturer's (Dow Corning, Midland, USA) recommendation in 10:1 ratio with the curing agent. The PDMS were prepared into 3 cm × 2 cm × 3 mm slabs. Viton rubber was obtained from Pelseal Technology (Bensalem, USA) (PLV 2000) company and mixed with its accompanying accelerator #4 in 44:1 ratio. Viton was paint brushed onto the top and the sides of each PDMS slab and allowed to cure at room temperature (25 °C) overnight.

Oxygen Calibration and Sealing Test

An inverted microscope Olympus IX71 was used to capture the phosphorescent intensity from PtTFPP/PS when exposed to 0% O_2 (from 100% N_2 standard laboratory line), 21% O_2 (composition of O_2 was assumed from the standard laboratory house air line), and 100% O_2 (from an industrial cylinder). The air was flown approximately 5 cm from the top of the devices. Each gas was connected to a separate tubing and could be switched quickly. The microscope was equipped with a 395 nm excitation LED and the appropriate filter cube for 650 nm emission capture by QImaging QIClick camera.

To test the effectiveness of the insulating layer, oxygen sealing test was carried out by periodically exposing the microchambers with 100% O_2 and measuring the changes in the phosphorescent intensity. Three tests were performed: (1) Microchambers; (2) Microchambers

covered with a PDMS slab; (3) Microchambers covered with a Viton coated PDMS slab. Measurements were performed in the dark at room temperature (25 °C).

Experimental Procedure

Experiments were done at the UCI optical biology core with a Zeiss LSM 780 confocal scanning microscope. Excitation wavelengths were 405 nm and 488 nm by lasers for PtTFFP/PS and Mitotracker Green, respectively. The LSM 780 can simultaneously monitor both red and green channels. Exposure time was set at 200 ms and images were taken every one second.

Microscope focus to the bottom of the chambers were first achieved before mitochondria deposition. Following the addition of 50 μM ADP to the mitochondrial suspension to initiate respiration, 2 μL of 0.2 μg/mL of mitochondrial protein was dropped and spread to the wafer's surface. After the mitochondria were deposited, a Viton coated PDMS slab was quickly placed on the wafer, effectively sealing and separating the microchambers. We then performed image acquisition for the durations specified in the results. To decouple the mitochondria or to induce maximal respiration rate, carbonyl cyanide 3-chlorophenylhydrazon (CCCP) was added along with ADP. Measurements were performed in the dark at room temperature (25 °C).

Up to 15 chambers were visible in the field of view. The chambers were separated into two groups: (1) with mitochondria and (2) without. Image processing was done with ImageJ. The average red intensity and green intensity (when applicable) were measured for each chamber. The data were processed in IGOR software. To minimize the effect of photobleaching, the red intensity was divided by the average green intensity from all applicable chambers. These data were further normalized by the initial processed intensity. The linear fit feature in IGOR was used to fit a line to the plotted data.

Results

Device Characterization

We fabricated our microchambers using a simple photolithography and wet etching process. To minimize oxygen permeability, we picked borofloat, which is generally considered oxygen impermeable. The process is briefly overviewed in Figure 1a. First, we replicated the surface (top) geometry of the microchambers from a predesigned photomask to the photoresist. After a few etching steps, the top glass surface of the microchambers was exposed and a depth could be created with 48% HF etching. One minute 48% HF etch created on average a 7.5 μm depth in the borofloat wafer. The etch undercut expanded the diameter of our chambers' top surface from 10 μm (mask design) to 15 μm. Finally, the PtTFPP dye incorporated in polystyrene were deposited at the bottom of the microchambers. To test the behavior of our sensing PtTFPP/PS layer, we exposed the layer to light streams of gas containing different concentrations of oxygen. Similarly, we also tested the effect of the Viton coated PDMS slab on sealing the top by quantifying the signal changes under alternating normal air and 100% oxygen gas. These tests were performed with an inverted microscope (Olympus IX71, Olympus America Inc., Center Valley, USA) equipped with an LED excitation source at 395 nm and a long pass emission filter at 650 nm.

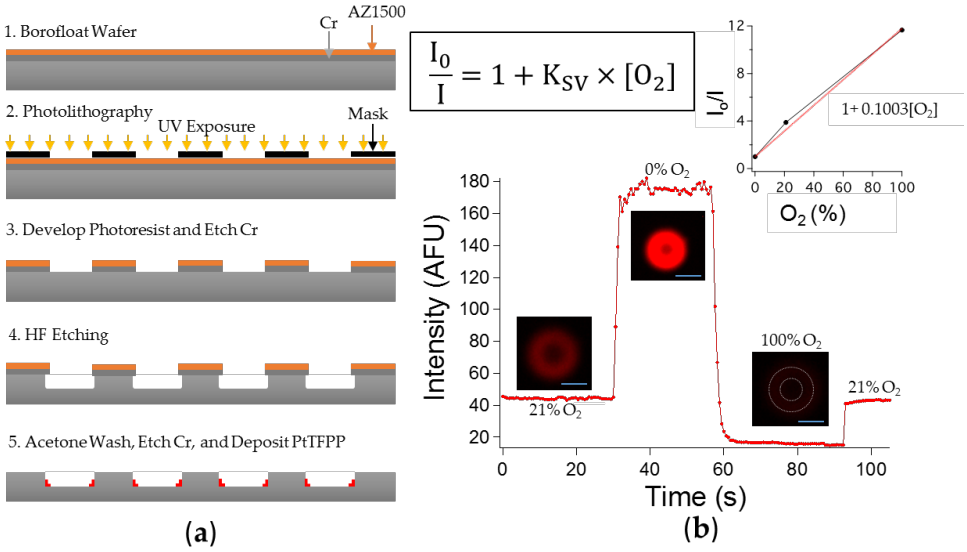

Figure 0.1: a) Overview of the device fabrication scheme; (b) Testing the oxygen sensitivity of a device by measuring the phosphorescent intensity. Three gas lines were used: 21% O_2 (house air), 0% O_2 (100% N_2), and 100% O_2. The top left inset is the Stern-Vollmer equation, outlining the inverse relationship between the intensity and the oxygen concentration with I_0 representing the intensity at 0% O_2. Images of the microchamber were set at the same contrast level. At 100% oxygen, the red intensity was indiscernible at the chosen contrast level so an outline of the chamber was included. Top right inset is the plotted average measured intensities (I_0/I with I_0 being the intensity at 0% O_2) at three different oxygen concentrations and the fitted line for Stern-Vollmer relationship. Scale bar is 10 µm.

Sensitivity to Oxygen: Oxygen Quenches PtTFPP Phosphorescence

We directly flew normal air (21% O_2), 0% O_2, and 100% O_2 sequentially at about 5 cm above the top of the microchambers. The gas lines could be switched quickly because we used individual tubings. A base line was established first with normal air (21% O_2). The response of our fabricated PtTFPP/PS sensing layer was as expected. The higher the oxygen concentration, the lower the phosphorescence intensity. Figure 2.1b shows the respective intensities under normal air, 0% oxygen, and 100% oxygen. The intensity and oxygen concentration could be fitted with a Stern-Vollmer linear relationship which shows that the intensity is inversely proportional to the oxygen concentration. We observed some delays (5–6 s) from 21% oxygen to 0% oxygen and to 100% oxygen and 1 s delay switching from 100% oxygen to 21% oxygen. Even though, these time delays could seem fast, they are expected because the time constant of PtTFPP is within the microseconds range [34,35], and when factoring experimental errors from

manual gas switching, the time delays were reasonable. In summary, these observations show that our microchambers were indeed sensitive to oxygen.

Effect of Viton Coating

To seal the top of the chamber, we tested a flexible sealing layer made of Viton covered PDMS. Viton is a black fluoroelastomer with exclusive impermeability to gases including oxygen. Viton has been used previously in microfluidics but mainly for chemical resistance instead of gas impermeability[36]. Viton's permeability to oxygen ranges from 0.6 to 1.3 Barrer (10^{-10} $cm^3 \cdot cm \cdot s^{-1} \cdot cm^{-2} \cdot cmHg^{-1}$) [37,38], significantly lower than that of PDMS which is 781 Barrer[39]. The use of Viton, which is black, also prevents light leakage from excitation source and maximizes the acquisition of the emitted light. Figure 2.2 shows that under intermittent 21% and 100% oxygen exposure, minimal change was observed in the phosphorescence intensity from the chamber covered with Viton-coated PDMS. In contrast, the uncovered microchamber exhibited intensity fluctuations during the gas exchange test. Minimal delay, in fractions of a second, in gas exchange was achieved by using different tubings for the gas streams. Adding a layer of PDMS on top of the microchamber partially sealed the sensing layer from being directly exposed to 100% O_2. However, because PDMS is still oxygen permeable, repeated exposure to 100% oxygen allows gradual migration of oxygen into the chamber resulting in the observed gradual decrease in signal intensity.

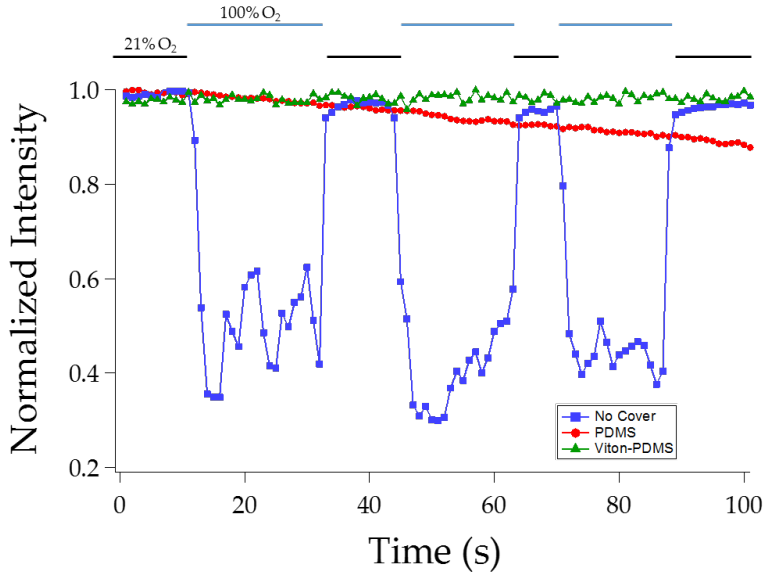

Figure 0.2: Normalized intensity (measured intensities divided by the corresponding maximum intensity) vs. time to summarize the effect of covering the chambers with 1. No Cover; 2. A PDMS slab; 3. A PDMS slab coated with Viton rubber. The microchamber was exposed to alternating normal air (21% O_2) and 100% O_2 gas. At each exposure outlined by the top two lines, multiple measurements were taken as indicated by the data points.

Single Mitochondrial Respiration

After demonstrating the oxygen sensitivity of our microchambers and the sealing capability of the Viton-PDMS layer, we performed respiration experiments on individual mitochondria. For these experiments, we utilized a confocal microscope LSM780 (Zeiss, Pleasanton, USA) which can monitor both the red phosphorescence from PtTFPP and the green fluorescence from Mitotracker Green used to stain the mitochondria. To minimize the effect of photobleaching, we used the ratio between the green and the red intensity as the metric and further normalize the signal to the initial reading.

Chambers with Mitochondrion vs. Empty Chambers

Figure 2.3 summarizes representative results of a single mitochondrial respiration experiment. This experiment was done in triplicate with two successful trials. Figure 2.3a shows that up to 15 microchambers could be viewed in the same field of view. Mitochondria were

distributed randomly, thus some chambers contained mitochondria while others did not. Our results show that in the chambers with mitochondria, the signal (the inverse of PtTFPP intensity) gradually decreased. This decrease means that oxygen was being depleted from the chambers, so we reasoned that the oxygen was being consumed by our deposited mitochondrion and this resulted in a slight decrease in the signal readout. The microchambers without any mitochondria, on the other hand, exhibited a slight increase in the signal readout, which we attributed to residual photobleaching not fully accounted for by the ratiometric method. Figure 3c shows the representative signal readout from a microchamber with a mitochondrion and another without; data points were averaged every 10 s in Figure 2.3c curves. Consequently, the oxygen consumption rate by individual mitochondria can be roughly represented by the slope at which oxygen was being depleted in individual microchambers. Figure 2.3c summarizes the distribution of such slopes or deduced oxygen consumption rates, with the negative slopes representing oxygen consumption rate from microchambers with a mitochondrion and vice versa with the positive slopes indicating empty microchambers. From the six microchambers with a mitochondrion, the inferred rates of respiration fluctuated (Figure 2.3c), indicative of functional heterogeneity even at this modest level. The scalability of our microchambers then make our technology an attractive platform for high-throughput study of mitochondrial functional heterogeneity. One potential complication in our measurement is that because the microchambers all interact with the PDMS slab's bottom surface, which is not coated with Viton, diffusion of oxygen from one chamber to the neighboring ones could be possible, but our results showed this effect could be ignored. There were also mitochondria outside of the chambers because the deposition was nondeterministic. These mitochondria were most likely pressed between the glass surface and the PDMS. Since PDMS is hydrophobic and we observed that the sealing layer

adhered well to the glass surface, we are confident that most of the experimental liquid were inside the microchambers

(Figure 2.3b). Similar observations were also reported in single cell respiration experiments [40].

Chambers with One Mitochondrion vs. Two vs. One Treated with CCCP

To further substantiate our demonstration of single mitochondrial respirometers, we compared the oxygen depletion in a chamber with one mitochondria against one chamber with two mitochondria and another with one mitochondrion treated with CCCP. As expected, the rate at which oxygen was being depleted in the chamber with two mitochondria was higher than that in the chamber with only one mitochondrion. Furthermore, CCCP is known to decouple the electron transport chain and ATP synthase, allowing the electron transport chain to run at its maximal rate. This translates into more oxygen being reduced at complex IV to water. We expected the oxygen depletion rate in chambers with CCCP treated mitochondrion would be higher than the non-treated counterpart and our result confirmed this expectation (Figure 2.4). This experiment was done on the same mitochondrial preparation and devices from the same batch. The calculated slopes here differ from those in Figure 2.3 because the devices used were from two different batches. Even though devices' behaviors are similar within a batch, from one batch to another, to accurately compare data, we would need a more robust calibration method (Supplemental Information).

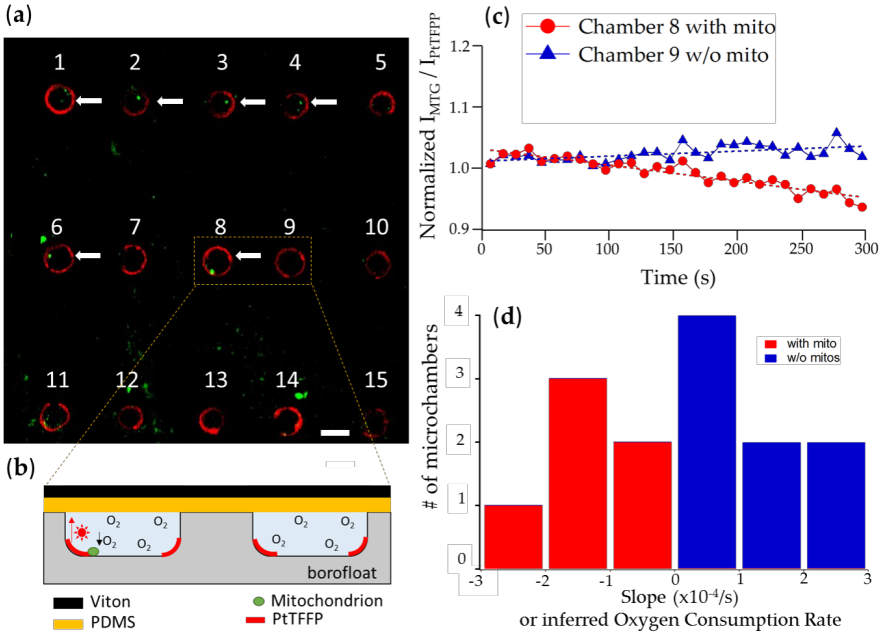

Figure 0.3: Up to 15 microchambers could be viewed in the same field of view. After mitochondria deposition and Viton-PDMS sealing, some microchambers contained mitochondria (indicated by the white arrows) and others did not. Scale bar is 15 µm; (b) Zoomed in, side-view cartoon of chambers 8 and 9; (c) Normalized intensity (radiometric measurement divided by the initial measurement) measurement of a representative microchamber with mitochondria and another chamber without mitochondria. The result for chamber 8 indicates a gradual decrease in signal signifying a depletion of oxygen while the result for chamber 9 displays a small positive slope probably due to unaccounted photobleaching. Data points were averaged every 10 s; (d) The histogram showing the calculated slopes of the measured intensities from chambers 1 to 14. Chambers 1, 2, 3, 4, 6, 8 were the ones with mitochondria. Chamber 15 was not included in the analysis due to insufficient signal readout. The slopes are directly related to the oxygen consumption rates.

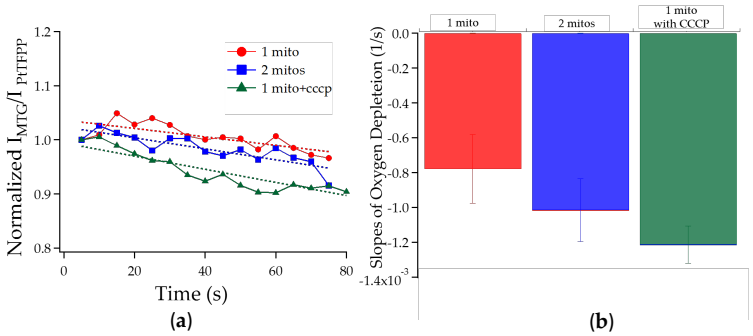

Figure 0.4: (a) Plotted PtTFPP normalized phosphorescent intensity from chambers with one mitochondrion, with two mitochondria, and with one mitochondrion treated with CCCP. Data points were averaged every 5 s; (b) The slopes of the fitted lines in (a) are plotted. Results indicated that the rates of oxygen depletion in the corresponding microchambers. The errors were obtained from fitting the data.

Discussion

We have demonstrated a simple, robust technology to assay respiration of individual mitochondria. The proof of concept shows that measurement of functional heteroplasmy (that is, functional differences between mitochondria) is possible. This is significant because heteroplasmy in the mitochondrial DNA content has been shown, but techniques to assay the functional differences are poorly developed.

How does this compare to existing technology? Broadly speaking, two methods are dominantly used to measure respiration: Electrochemical (Clark type electrodes) and luminescent readouts. Oxygen sensors based on a Clark-type oxygen electrode rely on the amperometric electrochemical reaction between a coated Pt-electrode and dissolved molecular oxygen, and have challenges for miniaturization such as consumption of oxygen by the sensor itself, and the requirement for a reference electrode [4–8,32]. Our approach in this paper has been to use oxygen-sensitive phosphorescent probes, which do not consume oxygen and offer high sensitivity, specificity, fast response times down to milliseconds[9], and demonstrated compatibility with biological samples[10].

Table 1 summarizes the features of selected state of the art commercially available instruments (Oroboros [5], Warner[6,41], Hansatech[42], Seahorse[24,43], MitoXpress[44,45]), as well as those demonstrated in research labs (Cantebury[46,47],MIT[7], and UWash[40,48]).

Company/Group	O_2 Reporter	Detection Method	Chamber Size	Sealed?	Fluid Handling	Adhesion?	# of cells	Amount of mitos	Throughput	Cost
Oroboros[24]	Clark	Electrical	2 mL	X	X	-	10^6	1 mg	low	high
Warner[25,30]	Clark	Electrical	100 µL	X	-	-	-	20 µg	low	mid
Hansatech[31]	Clark	Electrical	1 mL	X	-	-	10^7	5 mg	low	mid
Seahorse[6,11]	Luminescence	Intensity	5 µL	-	X	X	-	10 µg	high	high
MitoXpress[32,33]	Luminescence	Intensity, Lifetime	200 µL	X	-	-	-	60 µg	high	mid
Canterbury[34,35]	PtOEPK	Intensity	-	X	X	X	-	-	-	low
MIT[26]	PtOEPK	Lifetime	20 nL	-	X	-	-	-	-	low
Uwash[22,36]	Pt-porphyrin	Lifetime	80 pL	X	-	-	1	-	mid	low
This work	PtTFPP	Intensity	1.5 pL	X	-	-	-	1 pg	mid	low

Table 0.1: Comparison to selected available respirometers

Due to the diffusion of O_2, measuring the absolute oxygen consumption rate of any biological sample requires a completely sealed and isolated chamber. The available commercial Clark-type electrode systems offer excellent sealing chambers but require a large amount of sample and as discussed previously, they are not suitable for miniaturization. For the systems based on phosphorescent probes, commercial companies offer alternatives to sealing chambers. MitoXpress uses a layer of mineral oil to minimize to back diffusion of O_2; however, this approach is limited to assessing treated versus non-treated sample and still does not solve the sealing problem. Seahorse Biosciences, on the other hand, employs a semi-closed chamber and develops a complex mathematical model to calculate the O_2 back diffusion, which is deducted from their final measurements. Oxygen sensing has also been integrated in microfluidic channels[7,46,49]; yet, these channels were designed to monitor the oxygen level in tissue cultures

and not for the purpose of detecting oxygen consumption rate. Single-cell respiration with a set of sealed micro-wells have been demonstrated by UWash[50], however, this setup requires an external pressure by a piston. Our microchambers, in contrast, require no piston for sealing and can achieve single mitochondrial resolution, which translates to approximately 1 pg worth of mitochondrial protein[51]. In addition, our micro-chambers are only 1.5 pL, the smallest in size to our knowledge with the next smallest being 80 pL from UWash. These attributes present considerable improvements of our microchambers over the compared technologies.

While our approach demonstrates proof of concept, additional work is required to make the technology broadly useful in studies of mitochondrial heteroplasmy. First, the noise of the system needs to be critically assessed to determine the ultimate limits of respiration. At this point, while the integration time required for measurement (~10 s) is slightly better than existing technologies (~one minute), the signal to noise is inferior. One method to improve this would be to use phosphorescence lifetime rather than intensity measurement, which typically suffers from lower drift and improved signal to noise. We have demonstrated the feasibility of this approach for measuring oxygen tension in our chambers (Supplemental Information), so this is a clear possible next step. Second, a method needs to be developed to more practically introduce reagents into the chamber over time, rather than seal the chamber only once for the entire assay. Third, the instrument needs to be built out for turnkey operation, rather than requiring a skilled operator. This should be straightforward with appropriate off the shelf electronics, optics, and control software. Finally, the technology needs to be validated against existing biological models. Such a validation demonstration, of course, would only be possible for ensemble respiration measurements, as biological models for functional heteroplasmy of mitochondria are

only now possible to assess based on the prototype devices presented here. Of course, these four additional tasks are beyond the scope of this proof of concept prototype demonstration.

Intracellular probes for measuring oxygen concentrations have recently advanced in single cell applications[52–54]. However, these probes are still a matter for further research[55].

Conclusions

Overall, we have developed a proof-of-concept microchambers capable of detecting respiration at the single mitochondrial level. We achieved this by etching the microchambers out of borofloat glass (an oxygen impermeable material), depositing a phosphorescent sensing layer made of PtTFPP and polystyrene, and applying a sealing layer made of Viton coated PDMS to minimize oxygen diffusion.

Acknowledgments

This work was made possible, in part, through access to the confocal facility of the Optical Biology Shared Resource at UCIrvine. Peter J. Burke acknowledges funding from NIH National Cancer Institute Grant 1R21CA143351-01.

Additional Discussion

Qualitative vs. Quantitative Measurement of Respiration

What this study has not accomplished is to quantify the absolute oxygen consumption rate. In order to do that, careful calibrations of oxygen concentrations in liquid must be carried out. The calibrations done with simple gas streams were only to demonstrate the sensitivity of the sensing layer. However, the detection of single mitochondrial respiration was done in solutions, reflecting the relative oxygen concentrations in liquid rather than in air. Hence, to

obtain an accurate calibration of the sensors, we will need to expose the microchambers to solutions with known oxygen concentrations. Another way to improve on the existing detection method is to utilize the phosphorescent lifetime of PtTFPP instead of the intensity. The sensing principle of the oxygen-sensitive phosphorescent probes (PtTFPP included) is based on the dynamic quenching of the dyes' phosphorescent intensity and lifetime[11]. Specifically, oxygen molecules collide with the luminophores, deactivating them from their lowest excited state to the ground state[12]. The relationship of this quenching effect is described by the Stern-Volmer equation:

$$\frac{I_o}{I} = \frac{\tau_o}{\tau} = 1 + K_{sv}[O_2] \qquad \text{(A1)}$$

I_o and τ_o are the reference values in the absence of oxygen, whereas I and τ are the measured intensity and lifetime. The ratio of $\frac{I_o}{I}$ and $\frac{\tau_o}{\tau}$ are expressed linearly in terms of the Stern-Volmer constant K_{sv} and the concentration of O_2 in the solution. Equation (A1) is alternatively expressed in terms of the partial pressure of oxygen, which is related to the concentration of O_2 in solution via Henry's law. Typical oxygen assays based on phosphorescent dyes will begin with constructing a calibration curve for three to five different concentrations of oxygen with the choice of detected signal of either phosphorescent intensity or lifetime. If the selected measurement is intensity, the problems with photobeaching and optical interference from biological samples should be considered. As the probe's phosphorescence degrades after repeated exposure with excitation light source, the intensity-correlated measurement of oxygen concentration becomes unreliable. To mitigate this effect, one can utilize a concurrent oxygen-insensitive dye[13] (in our case, Mitotracker green). Conversely, phosphorescent lifetime is immune from photobleaching and optical interference because the lifetime, which is the average

time the luminophore stays in the excited state, is an inherent property of each probe. We have developed a preliminary setup to detect the phosphorescent lifetimes of PtTFPP and the results are promising. By relying on the phosphorescent lifetime, we could completely eliminate the effect of photobleaching and could also operate free from a microscope.

The system is outlined in Figure 2.5 and the preliminary measurement is summarized in Figure 2.6.

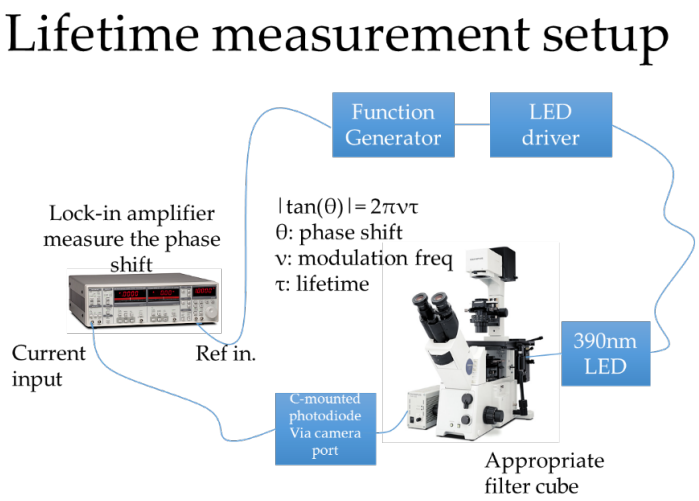

Figure 0.5: Photobleaching independent measurement setup for the phosphorescent lifetime of PtTFPP oxygen sensitive dye. The phase shift between the signal from the photodiode and the source excitation wavelength can be used to calculate the lifetime.

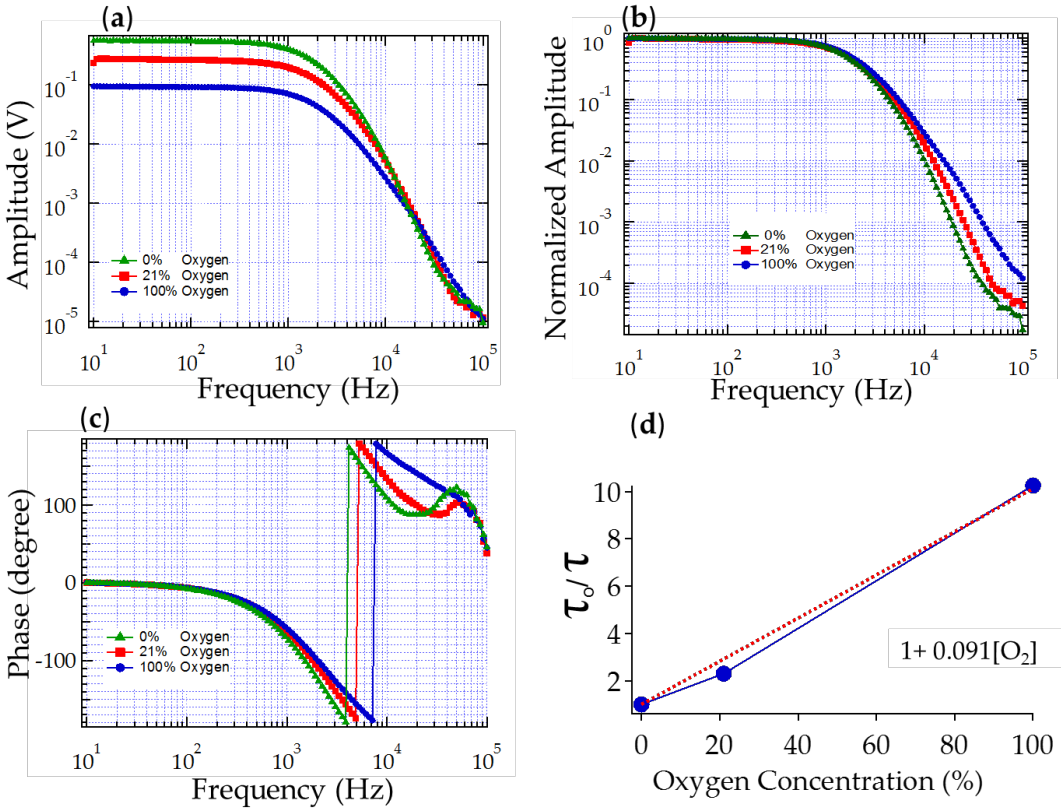

Figure 0.6: . Spectral characterization of the oxygen sensing microchambers. (a) Amplitude was measured in V for three oxygen concentrations; (b) Normalized amplitude vs. frequency; (c) The phase vs. frequency behavior. The lock-in SR830 displays phase output from −180° to 180° hence the jump at around 3 kHz; (d) Due to a considerable difference in the phase shift, we chose 10 kHz as the reference frequency and calculate the phosphorescent lifetimes from the phase readouts. The plot of τ_o/τ exhibits a linear Stern-Vollmer relationship. Our measured lifetime for 0%, 21%, 100% O_2 are 43.7 µs, 19.0 µs, and 4.26 µs, respectively. All of these values are consistent with what have previously been reported[34,35].

Proper Interpretation of Single Mitochondrial Respiration Data

Mitochondria vary in size, shape, mtDNA content, and thus (presumably) function[56,57]. Although extensive technology exists to measure their size, shape, and mtDNA content, technology to assess mitochondrial functional heterogeneity is still lacking. This has motivated our goal of assaying heterogeneity in mitochondrial function. In fact, ours is the first technology to determine functional respiration of intact, vital mitochondria. Therefore, this is a method to determine function, and may lead in the future to understanding of structure-function relationships of individual mitochondria. Unfortunately, such a comparison of single mitochondria is still not possible. In traditional ensemble experiments, the respiration rate is

typically normalized to the total "amount" of mitochondria, typically measured as the amount of mitochondrial protein measured by a BCA assay. However, such a normalization is not possible in our case, since the technology to measure the amount of protein in a single mitochondrion does not exist yet. A careful study of volume of mitochondria might be possible in future generations of this technique using advanced light microscopy, but has not been developed in this work. Advanced electron microscopy (such as TEM microscopy [47]) can determine structure, but the mitochondria are not functional once they have been fixed. Nonetheless, our technique can measure variation from one mitochondria to the next, which no other technique can do. In contrast to existing technology which allows for study of mitochondrial *content* (*typically mtDNA*) or *structure* (typically with ultra-high resolution electron microscopy), this work opens a new window to understanding and studying variability in biological *function* from one mitochondria to the next.

For our purpose, we would assume that all mitochondria have similar size and shape. The same assumption was implied in measuring the functional heterogeneity of membrane potential in individual mitochondria[56,58].

Lighting Conditions

Because mitochondria are also sensitive to light exposure[59], all mitochondria in this study were exposed to the same amount of excitation light with a dark isolated measurement environment during the experiments with confocal microscopy, which is still a recognized standard in studying single mitochondrial dynamics[60].

CHAPTER 3: FLUORESCENCE ANALYSIS OF SINGLE MITOCHODNRIAL WITH NANOFLUIDIC CHANNELS

Overview

Single mitochondrial assays are uncovering a new level of biological heterogeneity, holding promises for a better understanding of molecular respiration and mitochondria-related diseases. Here, we present a nanoscale approach to trapping single mitochondria in fluidic channels for fluorescence microscopy. We fabricate the nanofludidic channels in polydimethylsiloxane and bond them onto a glass slide, creating a highly reproducible device that can be connected to external pumps and mounted to a microscope. Having a unique nanoscale cross-section, our channels can trap single mitochondria from a purified mitochondrial preparation flown across. Compared with the traditional fluorescence method to monitor single mitochondrial membrane potential with glass slides and open fluidic chambers, our nanofluidic channels reduce background fluorescence, enhance focus, and allow ease in experimental buffer exchanges. Hence, our channels offer researchers a new effective platform to test their hypotheses on single mitochondria.

Introduction

There are many research and clinical motivations driving the development of high throughput techniques to study the biophysical and biochemical properties of individual (rather than ensemble) mitochondria. These motivations arise fundamentally from the established relationship between mitochondrial dysfunction and hereditary disorders as well as age-related diseases. Furthermore, while there is a growing body of evidence that mitochondria do not all behave identically, even within the same cell, and that this functional heterogeneity has important clinical manifestations, the advent of high throughput techniques can aid in quantifying and studying this heterogeneity among different patients, organs, tissues, and even

cells, under different chemical conditions, as well as a function of the age of an organism.

A wide range of degenerative disease symptoms have been linked to mitochondrial disorders. It has become increasingly evident that mitochondrial dysfunction contributes to a variety of age-related human disorders, ranging from neurodegenerative and neuromuscular diseases, stroke, and diabetes to ischemia-reperfusion injury and cancer[61,62]. Multiple diseases have been identified that result from mutations in the mitochondrial DNAs (mtDNAs) (see our website: http://mitomap.org). These genetic diseases have a very different genetics because each human cell contains hundreds of mitochondria and thousands of copies of mtDNAs, which are inherited through the oocyte cytoplasm and thus are maternally transmitted. Furthermore, the mtDNA has a high mutation rate, undoubtedly due to its direct exposure to mitochondrial ROS. When a new mtDNA mutation arises in a cell, this creates a mixed intracellular population of mtDNAs, a state termed heteroplasmy [28]. As the percentage of mutant mtDNAs increases, the mitochondrial energetic capacity declines, ROS production increases, and propensity for apoptosis increases. Consequently, diseases of the mitochondria have a delayed-onset and progressive course[61]. Since the mitochondria are the major endogenous source of ROS and ROS is thought to damage cells and DNA during the aging process, damage to the mitochondria and the mtDNA are likely to be the aging clock[63,64].

The empirical link between a genetic defect in an electron transport chain (ETC) component and a clinical pathology (specifically Leber's Hereditary Optical Neuropathy, LHON, a neurological disease) was discovered by one of us in 1988[65]. Since that time, researchers around the world have identified numerous genetic causes of ETC deficiencies, and genetic mitochondrial disease is now thought to occur in 1 in 5000 births[66]. 1 in 200 individuals is thought[67] to harbor deleterious mutations in ETC coding genes, which do not present clinically,

because the heteroplasmy of mitochondria allows both defective as well as healthy ETC mtDNA to exist in the same individual, and even the same cell[28].

In Parkinson's diseases it has been demonstrated that mitophagy, a cellular process that eliminates damaged mitochondria with low membrane potential, is compromised [68,69]. However, the pathways leading to mitophagy as well as compromising the process are not completely understood and studies are underway.

These three examples (aging, hereditary mitochondrial disorders, and neurodegenerative diseases) provide strong motivation for methods to study the properties of mitochondria at the individual mitochondria level in a platform compatible with high throughput screening. In this chapter, we present a platform in an attempt to forward the effort of such technology. Specifically, we aim to address the current technological obstacles in studying mitochondrial functional heterogeneity such as background fluorescence, photobleaching, mitochondria movement out of the plane of focus, and difficulties in precise delivery of substrates. Our solution comprises nanofluidic channels whose suitable topography can trap single mitochondria for fluorescence analysis [70]. Using a single step soft-lithography, we create channels with a multiple height profile including a trapezoidal cross section of 500 nm high and 2 μm wide. This particular geometry of our channel can mechanically trap single mitochondria while reducing background fluorescence and eliminating the out-of-focus issue. Connected to an external pump, our channels can deliver controlled amounts of respiratory substrates and inhibitors to the trapped mitochondria. As a result, we present an improved platform to monitor single mitochondrial membrane potential by performing first a quick trapping step then fluorescence microscopy. Interested researchers applying this simple methodology can perform similar assays on single mitochondria using different experimental buffers.

Fabrication process

Use ultrapure water with resistivity of at least 18.2 MΩ to prepare all solutions.

Nanofluidic channel components

1. Chrome photomask with channel patterns (*see* **Note 1**).

2. Four-inch silicon wafer (University Wafer, Boston, MA, USA).

3. Piranha solution: 3 parts sulfuric acid and 1 part hydrogen peroxide (*see* **Note 2**)

4. Hexamethyldisilazane , Sigmacote (Sigma-Aldrich, St. Louis, MO, USA)

5. Positive photoresist Microposit SC1827, Microposit MF-319 developer (MicroChem, Newton, MA, USA)

6. Silicon elastomer and curing agent (Sylgard 184, Dow Corning, Midland, MI, USA).

7. 0.025 OD x 0.017 ID, 0.500" length stainless steel pins (New England Small Tube, Litchfield, NH, USA)

Fabrication Equipment

1. KarlSuss MA-6 aligner

2. Oxygen Plasma Cleaner (Harrick Plasma, Ithaca, NY, USA)

3. Spin Coater (Laurell Technologies, North wales, PA, USA)

4. Hexamethyldisilizane (HMDS) priming oven (YES, Livermore, CA, USA)

Cell Culture Components

1. Hela Cells (ATCC, Manassas, VA, USA).

2. Culture media: Minimum essential medium, 10 % fetal bovine serum. Add 50 mL fetal bovine serum to 500 mL minimum essential medium. Store at 4°C. 1% penicillin-streptomycin (ATCC, 30-2300) is optional.

3. 0.25% Trypsin-EDTA 1X phenol red. Store at -20°C.

4. Phosphate buffered saline pH 7.2 without Calcium and Magnesium

5. Vented tissue culture T-75 flasks

6. Dounce Homogenizer: Pyrex 5mL Potter-Elvehjem tissue grinder with PTFE pestle (Corning, Tewksbury, MA, USA)

6. Isolation buffer: 210 mM mannitol, 70 mM sucrose, 1 mM EGTA, 5 mM HEPES, 0.5% BSA, pH 7.2 (*see* **Note 3**). Store at 4°C.

7. Basal respiration buffer: 2 mM $MgCl_2$, 10 mM NaCl, 140 mM KCl, 0.5 mM EGTA, 0.5 mM KH_2PO_4, 20 mM HEPES, pH 7.2 (*see* **Note 4**). Store at 4°C.

8. Stock solutions of respiratory substrates and inhibitors: 2 mM rotenone, 500 mM succinate, 500 mM malate, 20 mM CCCP, 10 mM ADP (*see* **Note 5**).

9. Protease inhibitor cocktail (Thermo Scientific, Waltham, MA, USA) (*see* **Note 6**).

10. Pierce™ BCA protein assay kit (Thermo Scientific, Rockford, IL, USA)

Fluorescent Dyes

Obtain all dyes from Life Technologies, Grand Island, NY, USA.

1. JC-1 assay kit: Store at 4°C. Make 200 μM JC-1 with DMSO immediately prior use.

2. TMRM: Make and divide 10 mM TMRM in DMSO to 4 μL aliquots. Store at -20°C.

3. Mitotracker® Green (MTG): The dye comes in 20 aliquots of 50 μg. Store at -20°C. Prepare fresh by first thawing then adding 74 μL of DMSO to 1 mM. Diulte in experimental buffer to 100 nM final concentration.

Microscope Setup

Experiments can be performed with any comparable set-up to the following:

1. Inverted microscope Olympus IX-71 with 4X, 20X, 60X objectives

2. TRITC & FITC filter sets

3. X-Cite 120PC Q fluorescence light source (Lumen Dynamics, Mississauga, Ontario, Canada).

4. 12-bit monochromatic QIclick-F-M-12 CCD camera (QImaging, Surrey, British Columbia, Canada)

4. NE-4000 programmable double syringe pump (Pump Systems, Farmingdale, NY, USA)

Methods

Perform all procedures at room temperature unless otherwise noted. Use a chemical fume hood to handle hazardous chemicals and a biosafety cabinet for biological samples.

Silicon Mold Fabrication

1. Clean a silicon wafer with 120°C Piranha solution for 1 hour. Rinse the wafer thoroughly with ultrapure water. Dry the wafer with nitrogen gas stream and dehydrate it at 120°C on a hot plate for 1 hour.

2. Prime the wafer with hexamethyldisilizane to improve photoresist adhesion (*see* **Note 7**).

3. Spin coat Microposit SC1827 positive photoresist at 3500 rpm for 30s. The photoresist should cover 75% of the wafer prior to spincoating. Prebake at 90°C for 30 min in a convection oven.

4. Load the prebaked wafer and the chrome photomask into Karl Suss MA6 mask aligner. Use soft contact setting and exposure dosage at 160 mJ/cm^2.

5. Use 300 mL Microposit MF-319 in a glass beaker to develop the exposed wafer. Swirl the beaker gently to promote the developing process. The developing should take around 25 s. Perform occasional checking of the patterns with a microscope and adjust the developing time to ensure accurate developing the first time.

6. Postbake is not necessary. The mold is ready to use at this point (**Fig 3.1a**).

PDMS device fabrication

1. Mix silicone elastomer and curing agent thoroughly at a 10:1 weight to volume ratio. Degas PDMS for 40 min in a vacuum desiccator. We use 40 g of silicon elastomer and 4 mL of curing agent.

2. Place the silicon mold into a Petri dish. Use a disposable plastic pipet to dispense a few drops of Sigmacote onto the mold and let it dry in a fume hood for 40 min. This step aids with the release of PDMS from the mold later.

3. Pour degased PDMS onto the mold. Blow away any surface bubbles with a plastic pipet. Place the mold in a 60°C curing oven overnight.

4. After curing, cut and peel individual PDMS devices from the mold (**Fig 3.1c,d**). Use steel cylinders with diameter of 0.63 mm to punch out inlet and outlet holes in PDMS using a 23 gauge stainless steel needles with inner diameter of 0.017'' and outer diameter of 0.025''.

5. Clean glass slides with Piranha solution at 120°C for 1 hour on the same day with cutting PDMS devices.

6. To promote adhesion between glass surface and PDMS slaps containing the channels, expose the two surfaces to 70 W oxygen plasma treatment at 100 mTorr for 20 s. Immediately bond the PDMS slap and the glass slide and leave them in 70°C for 20 min (*see* **Note 8**).

Cell Culture and Mitochondria Isolation

1. Grow Hela cells in T-75 flasks. Replace cell culture media every 2 days and passage 1 to 4 every 4 days. Keep the cells in exponential growth phase.

2. Harvest cells at 95% confluence in 2 T-75 flasks on the days of experiment.

3. Wash the cell pellet with phosphate buffered saline. Perform all subsequent steps on ice at 4°C.

4. Replace PBS with 1 mL isolation buffer and transfer the solution containing cells to a Dounce homogenizer.

5. Use 30 downward and circular strokes to shear the cells. Do this slowly and on ice (*see* **Note 9**).

6. Add 3 mL isolation buffer to the homogenizer and transfer the homogenate to two 2-mL Eppendorf tube.

7. Spin at 2000xg for 4 min at 4°C and discard the pellet.

8. Transfer the resulting supernatant to two new eppendorf tubes.

9. Centrifuge at 12,000xg for 10 min at 4°C and discard the supernanant.

10. Resuspend the pellet in each tube with 300 μL isolation buffer and combine into one tube.

11. Centrifuge at 12,000xg for 10 min at 4°C. There will be a light-colored sendiment containing damaged mitochondria surrounding a brownish-color pellet. Carefully rid the light-colored sendiment with a 1-10 μL micropipette tip from the pellet. Discard the super nant.

12. Resuspend the purified pellet with 1 mL isolation buffer and centrifuge at 12,000xg for 10 min.

13. Resuspend the pellet with 100-200 μL basal respiration buffer in a small tube (*see* **Note 10**).

14. Dilute to a final protein concentration of around 50 μg/mL.

15. Label mitochondria with fluorescent dyes: add JC-1 or TMRM to the mitochondrial suspension to a final concentration of 300 nM or 100 nM respectively. MitoTracker® Green can also be used concurrently with TMRM (*see* **Note 11**).

3.4 Typical Experiment Setup

1. Insert a 0.025 OD x 0.017 ID, 0.500" length stainless steel pin in the inlet hole of the PDMS chip for chip to tube interface.

2. Connect the chip to the syringe pump using a Tygon tube with ID 0.02" and OD 0.06".

3. Initially pump respiration buffer to fill the channel. Set the flow rate at 10 μL/h (*see* **Note 12**).

4. Examine the device under a bright field microscope. Once the channel is filled and the flow is uniform, introduce mitochondrial solution into the channel (**Fig 1e**).

5. Monitor the nanochannels with fluorescence microscope, mitochondria will gradually get trapped. Start taking images with the fluorescence microscope (*see* **Note 13**) (**Fig 2**).

6. After about 2 minutes, there will be a few mitochondria immobilized in each channel.

7. To investigate the effect of OXPHOS substrates on the membrane potential, swap and pump in the experimental buffer of choice, decrease the flow rate to avoid dislodging the trapped mitochondria. Let the solution flow for a few minutes before taking images (*see* **Note 14**).

Image Acquisition and Analysis

1. We use μ-Manager software to control image acquisition and ImageJ to analyze the data.

2. A typical experiment usually lasts 10 min with continuously imaging every 5 s and 2.5 s exposure time.

3. Load time-lapsed data into ImageJ. Use a 3x3 median filter to remove noise.

4. Draw and define regions of interest by tracing the perimeter of each mitochondrion. Use the same area of a region of interest and define three background areas in the vicinity of each mitochondrion.

5. Measure the intensity for each mitochondrion and subtract the averaged background noise.

6. For JC-1 assay, it is useful to establish red-to-green intensity ratio to qualitatively compare the mitochondrial membrane potential (*see* **Note 15**) (**Fig 3**).

7. For TMRM assay, co-staining the mitochondria with MitoTracker® Green helps with the

trapping visualization in green channel. Once trapping is established, switch to red channel and perform time-lapse experiments (*see* **Note 16)** (**Fig 4**)

Notes

1. We draw the channel design in L-Edit, a computer-aided design software and send the exported graphic design system ("*.gds") file to a photomask foundry e.g. Photosciences Inc. A chrome photomask is necessary due to the smallest feature size of 2 μm, which is too small for transparent papermask and flood exposure to render faithfully. Our design and gds files can be provided upon request (**Fig 1b**).

2. Piranha solution is extremely corrosive and must be handled with care and inside a chemical fume hood. Wear adequate and correct personal protective equipment. To clean one silicon wafer, we use 60 mL sulfuric acid and 20 mL hydrogen peroxide. Always add hydrogen peroxide to acid. The hot plate should be set at 120°C and run for an hour. Bubbles will occur, indicating the cleaning action in effect.

3. To make 250 mL isolation buffer, use 10.25 g mannitol, 6.42 g sucrose, 0.05 g EGTA, 1.192 g HEPES. Add 200 mL ultrapure water, adjust pH to 7.2 with 1M KOH. Fill more ultrapure water to make up 250 mL. Sterile filter the solution. Make 0.5% BSA by filling 5 g of fat-free BSA (part number) with ultrapure water to 100 mL. On days of experiment, add 1 mL 0.5% BSA to 9 mL isolation buffer to achieve 0.05% BSA. Store at 4°C.

4. To make 250 mL basal respiration buffer, use 0.1 g $MgCl_2$, 0.15 g NaCl, 2.609 g KCl, 0.02 g EGTA, 0.017 g KH_2PO_4, 1.19g HEPES. Add 200 mL ultrapure water, and adjust pH to 7.2 with 1M KOH. Fill more water to make up 250 mL. Sterile filter the solution.

5. CCCP is extremely hazardous, make a stock solution with absolute ethanol immediately upon receipt and store at -20°C. Prepare rotenone, succinate, and ADP stock solutions with ultrapure

water and make aliquots of 100 μL for later use. Except rotenone stored at room temperature, other chemicals should be stored at -20°C. Dilute stock solutions with basal respiration buffer.

6. Because proteases released from the disrupted cells can digest mitochondria, adding the cocktail prolongs the isolated mitochondria's viability and intactness. Add protease inhibitor cocktail to the isolation buffer prior to cell lysing. The stock cocktail comes 100X, use 1 part of stock and 99 parts of the isolation buffer.

7. Hexamethyldisilazane is used before photoresist spinning to make the Si substrate hydrophobic and improve the adhesion between the photoresist and the substrate. HMDS can be spin coated on the substrate or applied onto the substrate by vapor priming method. Best results are achieved by the vapor priming method.

8. Plasma treatment converts PDMS surface from being hydrophobic to hydrophilic. This helps with the adhesion to the glass slide and promotes fluid flow through the nanochannels. Plasma treatment is not, however, permanent. Hence, the devices should be used as soon as they are bonded. To further prolong the hydrophilicity, prime the channels with polyvinyl alcohol and then wash with ultrapure water.

9. Other cell lines will require different number of homogenizing strokes. Perform a simple lysing experiment to determine an optimal number for your cell lines. Alternatively, use a motorized homogenizer [32].

10. We store the final crude mitochondria isolation in a small tube to minimize exposure to surface oxygen. Once isolated, the mitochondria have a short useable lifetime of 1-2 hours. At this point, mitochondrial protein quantification can be performed. However, because BSA and EGTA interfere with protein measurements, prepare and use an isolation buffer without BSA and resuspend the mitochondrial pellet with basal respiration buffer without EGTA. Use at least 100

μL of sample for the protein assay.

11. Because TMRM and JC-1 are dynamic dyes, whose distribution across the mitochondrial inner membrane is dependent on the mitochondrial membrane potential, experimental buffers should contain the same dye concentration. In contrast, MitoTracker® Green is also mitochondrial specific but does not depend on the mitochondrial membrane potential; hence, other than an additional incubation with the isolated mitochondria for 10 min before use, the dye is not necessary in experimental buffers. The addition of MitoTracker® Green to assays with TMRM is useful to visualize the mitochondria because some of them might not be energized enough for TMRM fluorescence.

12. Use the pump in WITHDRAW mode that is the syringe serves as a waste reservoir, pulling solution away from the vials containing experiential buffers and through the channels. We find that this approach is easier than pushing the solutions into the channels and also allows us to quickly change the experimental buffers by swapping out vials instead of syringes.

13. Use a fast exposure time e.g. 100-500 μs to monitor the efficiency of trapping. Initially, to get acquainted with the trapping process, use fluorescently labeled microbeads with diameter of 1 um (Life Techonologies, Grand Island, NY, USA).

14. To investigate complex II, for example, flow in 100 nM TMRM, 2 uM rotenone and 10 mM succinate. To initiate mitochondrial respiration, add 50 μM ADP and to uncouple ATP synthase and the electron transport chain, use 100 nM. We recommend prepare experimental buffers with the basal respiration buffer. For other components of oxidative phosphorylation process, respective experimental buffer solutions can be strategically used [71].

15. Since we have only one detector, we image the red and green signals from JC-1 assays asynchronously by manually adjusting the filter cubes. For time-lapse fluorescence imaging, the

filter is set to capture the red fluorescence only. If two detectors are available, simultaneous monitoring of Red and Green fluorescence can be performed.

16. From our experience, JC-1 works well with comparing mitochondria in treated vs. non-treated assessments. In other applications, JC-1 might not be suitable because of its slow response time and its high propensity to photobleaching [72]. We observe a larger extent of photobleaching in using JC-1 compared with TMRM. TMRM has a faster response time but can easily bind to PDMS if the channels' surface is not hydrophilic enough, increasing the interfering background fluorescence. This observation is one weakness of our channels. Optimization steps such as fine tuning oxygen plasma treatment and priming the channels with polyvinyl alcohol might reduce the hydrophobicity of PDMS and thus potentially mitigating the problem. If absolute determination of mitochondrial membrane potential is desired, the interested readers can refer to our previous work [73] and others [74].

Results and Discussion

Mitochondria Trap Devices

The goal of this project was to design a nanochannel device with dimensions small enough to trap individual mitochondria as a demonstration platform for manipulation and interrogation under controlled conditions at the single mitochondrial level. Mitochondrial morphology is varied, both *in vivo* and *in vitro*. A typical morphology is a cigar shape of width from 200 nm to 1 μm.[75] For this, standard photolithographically defined PDMS channels have not yet been pushed to the submicron scale,[76] while nanochannel technology based on etching[77] is too small to pass single mitochondria.

The mitochondria trapping device is a nanochannel array, with two access channels and two access holes for fluid inlet/outlet as shown in Figure 3.1. The nanochannels have a trapezoid cross-section that is 3.5 μm at base and gradually narrows down to around 400 nm. The average width of the channels (the width at middle of the trapezoid) is around 2 μm which is larger than the diameter of mitochondria (0.2-1.2 μm) [75] and the height of the nanochannels at its highest point (0.45-0.75 μm) is almost equal to the average diameter of the mitochondria (terminology nanochannel has been used to describe channels with dimensions smaller than 1μm.[78] These dimensions are measured from AFM images. The nanochannels are 500 μm long and are connected to two 100 μm wide, 2 μm high access channels. The device is fabricated using simple, economic and high throughput soft lithography of PDMS.

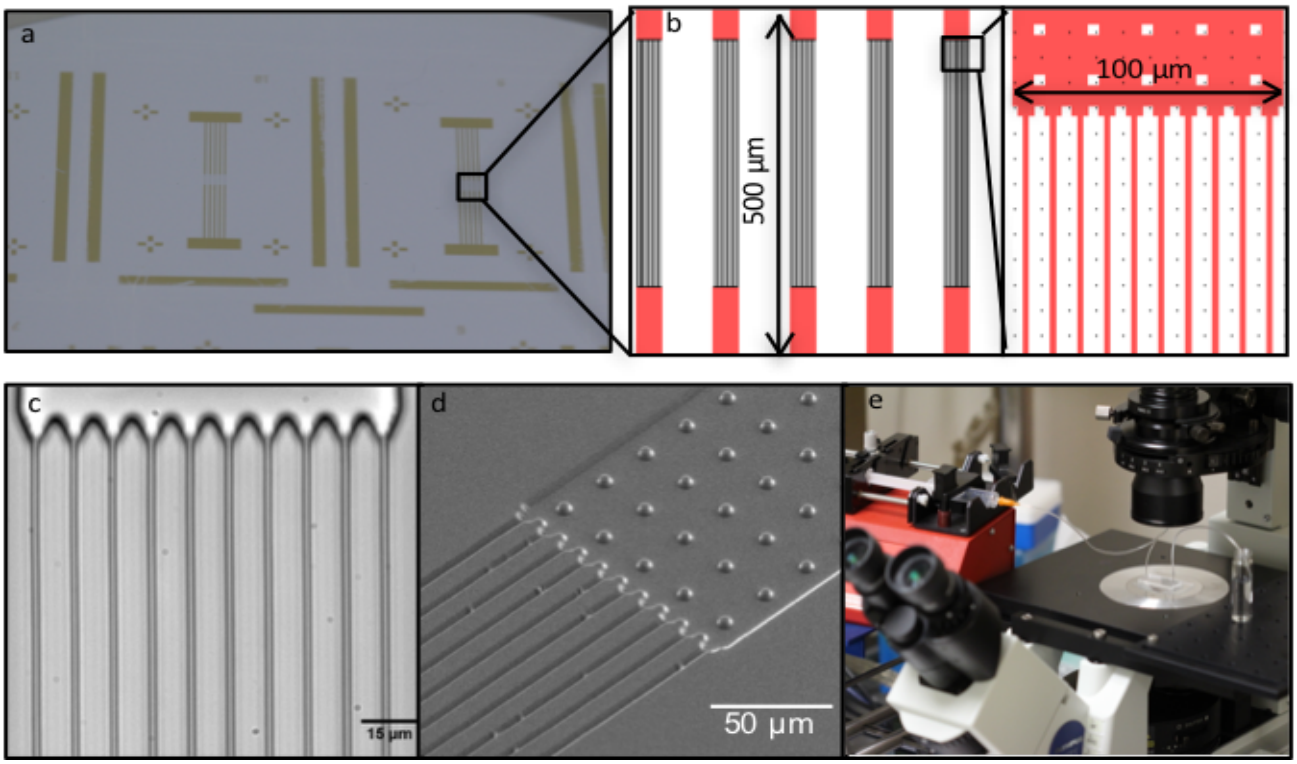

Figure 0.1: a) Fabricated mold on a Si wafer. b) An example of the mask design in L-Edit. c) bright-field image of PDMS channels. d) SEM image of PDMS channels upside down; micro-posts in the larger channel keep the wide part from collapsing. e) A typical experimental setup. (Panels c & d. adapted from (*7*) with permission from American Chemical Society)

Immobilization of Mitochondria

Mitochondria solution is introduced into the channels with a syringe pump. Individual mitochondria start to get trapped in the nanochannels and their population gradually goes up as the flow continues. In Figure 3.2, an example trapping experimental run is shown. Mitochondria stained with MTG are flown into channels with a rate of 10 μL/hour. Time-lapse microscopy of the channels is performed at the same time. In all experiments where mitochondria were imaged, their position was fixed after the initial introduction. The chemical environment can be adjusted through additional fluid flow at rates of up to a few μL per minute. This is shown, for example, in Figure 3.2. Thus, the mitochondria are gently trapped inside the nanochannels, enabling access to fluid for them but they are not moving.

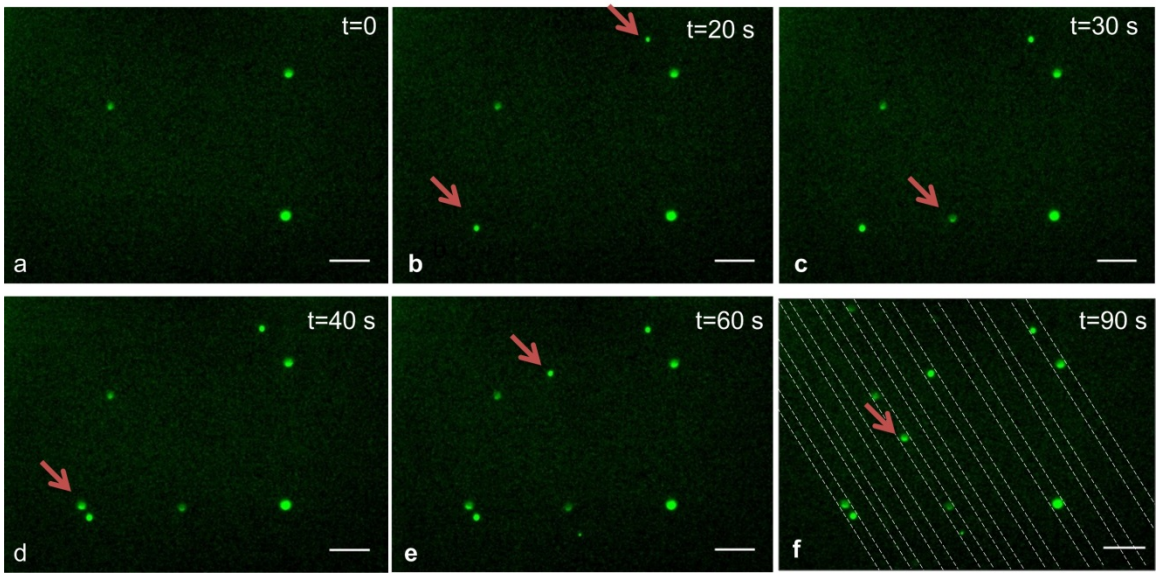

Figure 0.2: Series of time images of MTG labeled mitochondria. In each image, a new mitochondrion appears that has been flown in from the reservoir and trapped inside the nanochannel. Red arrows indicate the addition of new mitochondria. Dashed lines in panel f suggest the outline of the channels. Scale bar is 10 µm.

Trapping Mechanism

The trapping mechanism is not mitochondrial interactions with the channel sidewalls. This was shown by performing a similar experiment with larger channel sizes but otherwise nominally identical conditions. For the larger channels, the mitochondria do not stick to PDMS surfaces. It has been shown that oxidized PDMS has negative surface charge.[79] Thus, it is likely that an electrostatic repulsion between the mitochondria and the sidewalls prevents adhesion between the negatively charged mitochondrion and negatively charged channel surface.

The mitochondria are physically trapped along the channels (Figure 3.3). Since the height of the channel at the highest point is similar to the average diameter of mitochondria but the width is around two times larger, the channels act like a filter where fluid can pass through but individual mitochondria are trapped along the channels one by one. Due to variations in size of individual mitochondria and also the trapezoidal cross section of the channels, occasionally we see that one mitochondrion is trapped in some location in the channel but a smaller mitochondrion can pass along the first mitochondrion and get trapped at a further location. Exact determination of trapping locations requires mathematical simulations, but based on our experimental observations we believe that mitochondria that are already trapped at the channel entrance due to the small height of the channel behave like obstacles that disrupt the flow in the narrow channel and create vertical components in the flow direction (vertical to the channel direction).

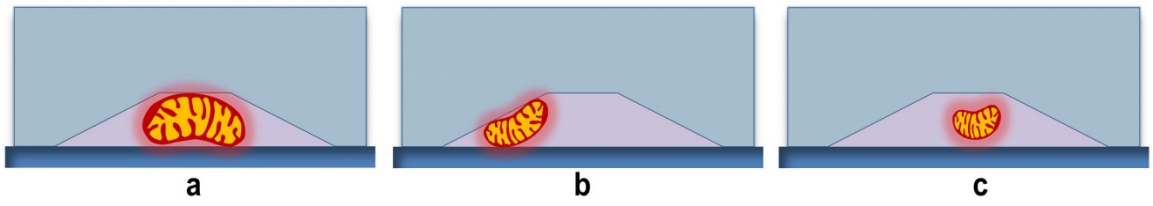

Figure 0.3: Cross section of the channels and trapping mechanism of mitochondria. a) Larger mitochondria get trapped at the middle of the channels. B) Smaller mitochondria get trapped at the corners, leaving room for other mitochondria to pass. C) Some small mitochondria will pass through

The flow direction, variations in mitochondria size and the trapezoidal cross section of the channel results in mitochondria getting trapped at random locations along the channel. We have found experimentally that for a flow rate of 10 μL/hour, the concentration of mitochondria in the flow buffer that results in an appropriate number of trapped mitochondria for our imaging setup is around 50 μg/mL of mitochondrial protein. The procedure to find this value is discussed in the following paragraph.

If the amount of mitochondria that reaches the channel entrance is too high, initially a few mitochondria are trapped in the channel, but additional mitochondria can block the entrance. It is important for imaging to use an optimized mitochondrial concentration. We tried different concentrations of mitochondrial protein from 300 μg/mL to 1 μg/mL while keeping the flow rate constant at 10 μL/hour and the flow time at 2 minutes. With a mitochondrial protein density of around 300 μg/mL, concentration of trapped mitochondria was high and we could see clogs at the entrance to the channels and also inside the channels (Figure 3.4).

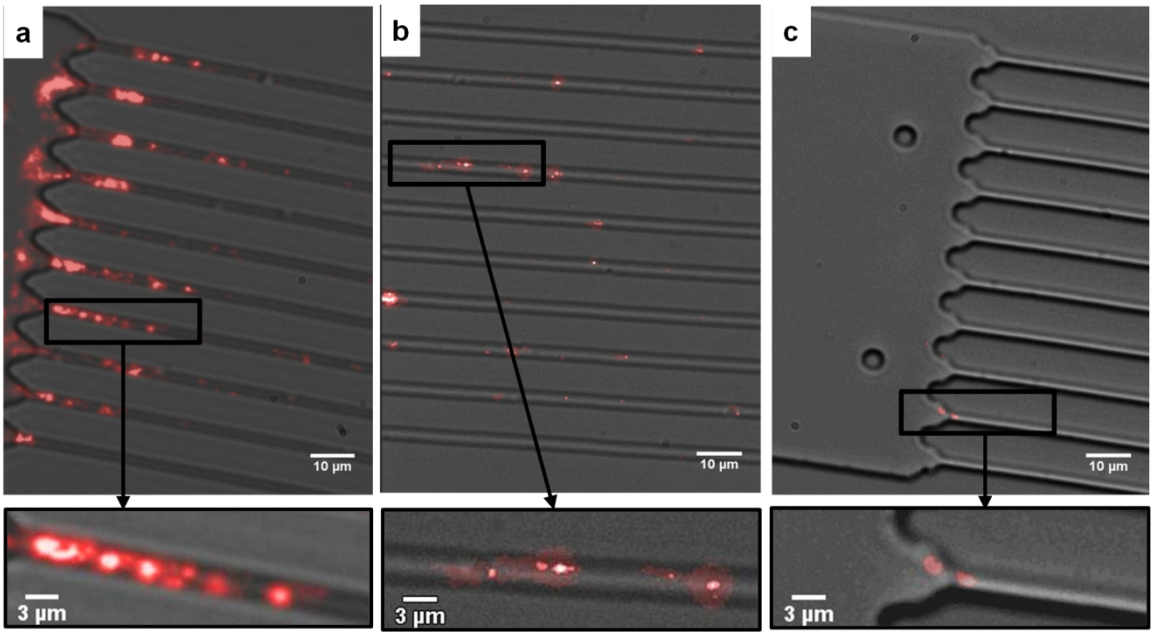

Figure 0.4: Different concentrations of trapped mitochondria (labeled with JC-1, red fluorescence shown) achieved by changing the mitochondria concentration in the filling solution. All channels have been pumped with the mitochondria solution rate of 10 µL/hour for 2 min., a) 300 µg/mL protein concentration (density too high), clogs are formed in the trap channels b) 50 µg/mL protein concentration (density optimum), c) 1 µg/mL protein concentration (density low). Bright field and fluorescence images are captured separately and merged later

While with protein concentration of 1 μg/mL we saw only four mitochondria trapped in the whole channels (Figure 3.4). Concentration of around 50 μg/mL, on average, resulted in a few mitochondria being trapped per channel (Figure 3.4b) and most of the mitochondria were far enough from each other that we could easily distinguish them with microscope. Since the "clogs" are not observed when lower concentration of mitochondria is used, we believe they are mitochondria that are packed so closely that it is difficult to distinguish between them, the smallest resolvable distance between two mitochondria depends on the specifications of the microscope and is discussed more in the imaging section. The optimum concentration also depends on the flow rate. With a smaller flow rate, there is more control over the number of trapped mitochondria, the channels can be monitored through the microscope and once an appropriate number of mitochondria are trapped the flow can be stopped, but that would increase

the loading time and due to limited lifetime of isolated mitochondria, would decrease the number of the assays that can be performed. We have kept the loading time and the flow rate constant and used a mitochondria concentration that would result in a few trapped mitochondria in each channel. The total amount of mitochondria protein that we are flowing into the channels at a concentration of 50 μg/mL and flow rate of 10 μL/hour for 2 minutes is around 16 ng. This concentration is over an order of magnitude lower than what is used in most experiments.[80,81] This can be used to estimate the appropriate concentration for different flow conditions. The number of trapped mitochondria for each experiment using the described conditions is generally 20-40 in the field of view. It is possible to increase the throughput by increasing the number of nanochannels, and using an imaging system with higher resolution and larger field of view.

$\Delta\psi_m$ Assays

The mitochondria in our channels are vital and sustain a membrane potential. This can be demonstrated using the fluorescence dye JC-1

In Figure 3.5 (a-c), separate green and red fluorescence images of the same mitochondria are shown, as well as their superposition over the bright-field image of the nanochannels. JC-1 stained mitochondria are provided with 10 mM sodium succinate and flown into channels with a rate of 10 μL/hour. After 2 minutes the flow is stopped and the channels are imaged. Clearly, the mitochondria are trapped individually in the nanochannels, and a large percentage of them are bright red, indicating the membrane potential is still large. The blue bars in Figure 3.5 (d) shows the histogram of red/green fluorescence intensity for 31 mitochondria that were in the field of imaging. Around 80% of the mitochondria have a ratio of 3 or higher. As a control we performed the same experiment with substrate deprived mitochondria that are expected to have a lower membrane potential. The distribution of red/green fluorescence intensity ratio for mitochondria

in this sample is shown by the white bars in Figure 3.5 (d). Out of 39 mitochondria, 65% have a ratio of 2 or lower.

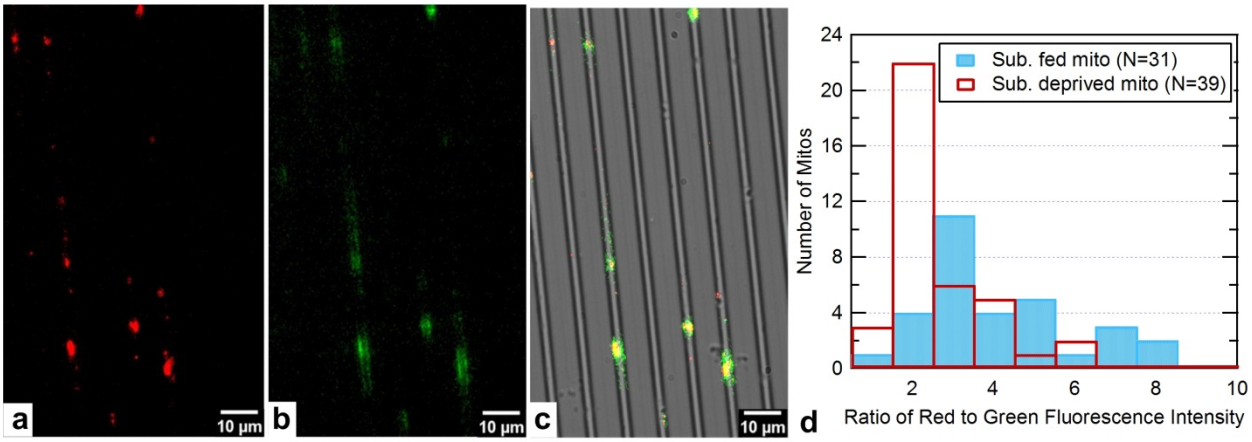

Figure 0.5: Image of JC-1 stained trapped mitochondria. a) Image taken with TRITC filter. B) Same mitochondria imaged with a FITC filter. C) Overlap of a, b and bright field image of the channels. D) Histogram of ratio of red to green fluorescence for substrate fed mitochondria) and substrate deprived mitochondria (Total number of substrate fed mitochondria is 31 and total number of substrate deprived mitochondria is 39).

Time Dependence of $\Delta\psi_m$ of Individual Mitochondria

To monitor the time dependent membrane potential we performed time-lapse microscopy of stained trapped mitochondria for over ten minutes with continuous illumination.

Mitochondria stained with 30 nM TMRM were introduced into our nanochannels, and an image was captured every 5 seconds, with an image acquisition time of 2.5 seconds per image. As can be seen in Figure 3.6, the fluorescence intensity from TMRM stained mitochondria remains relatively constant indicating that the trapped mitochondria maintain their membrane potential for a long time.

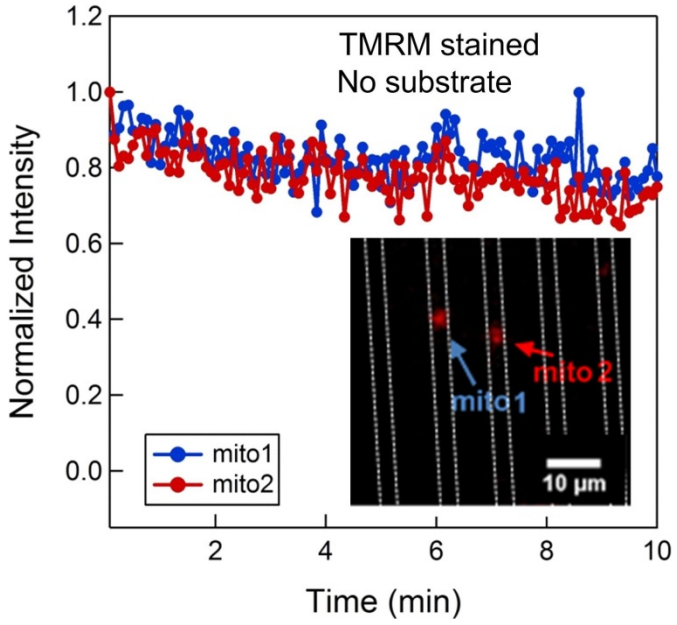

Figure 0.6. Normalized TMRM fluorescence intensity from two individual trapped mitochondria imaged every 5 s. Arrows in the inset point to the mitochondria the intensity of which is shown. Dashed lines suggest the outline of the channels.

The substrate response and MMP experiments described next were performed using JC-1. Because of our microscope setup we can only use one filter cube at a time for time-lapse fluorescence microscopy and we cannot measure both red and green simultaneously, so we only monitored the red intensity (which has been reported to be linearly correlated with membrane potential)[82]. To account for the inaccuracies such as those caused by the apparent size of mitochondria compared to their real size that might be caused by using the red fluorescence only, we are showing the normalized traces for each mitochondrion. Each trace is divided by the fluorescence intensity measured for that mitochondrion at time zero, so that all the traces start at intensity of one. This way we are not comparing different mitochondria, but we are looking at the trend of membrane potential change for one mitochondrion.

Substrate Modulation Δψm of Individual Mitochondria

Without OXPHOS substrates, the electron transport chain is idle, and the membrane potential remains in its basal, resting state. In order to demonstrate the ability to chemically modulate the electron transport chain and the 53ioenergetics state of the mitochondria in our nanochannels, we performed a series of experiments with and without OXPHOS substrates Pyruvate/Malate present in the respiration buffer.

In Figure 3.7, we show two sets of experiments in which the mitochondria are labeled and imaged with JC-1. In (a), substrates are not used. In (b), OXPHOS substrates, 5 mM Pyruvate and 5 mM Malate, are added to JC-1 stained mitochondria respiration buffer just before flowing the mitochondria in the channels. This activates the electron transport chain and initially increases the mitochondrial membrane potential $\Delta\psi_m$. As mitochondria gradually consume the substrates, the substrate concentration decreases, therefore the membrane potential and fluorescence intensity gradually drop and become identical to the sample without substrates.

Typical normalized red fluorescence intensity of JC-1 stained mitochondria is shown in Figure 3.7 (a) (each curve shows the fluorescence from a single mitochondrion.) It is observed that for JC-1 stained mitochondria the fluorescence intensity has dropped around 50% during the time span that they were continuously illuminated for photography, and we attribute this to photo-bleaching of the JC-1,(also reported by other groups)[83,84] since experiments with identical buffer but different stain (TMRM) showed no appreciable decay in the membrane potential (Figure 3.6).

Similarly, in Figure 3.7 (b), the fluorescence intensity decays with time but this time with a higher rate, due to gradual consumption of OXPHOS substrates

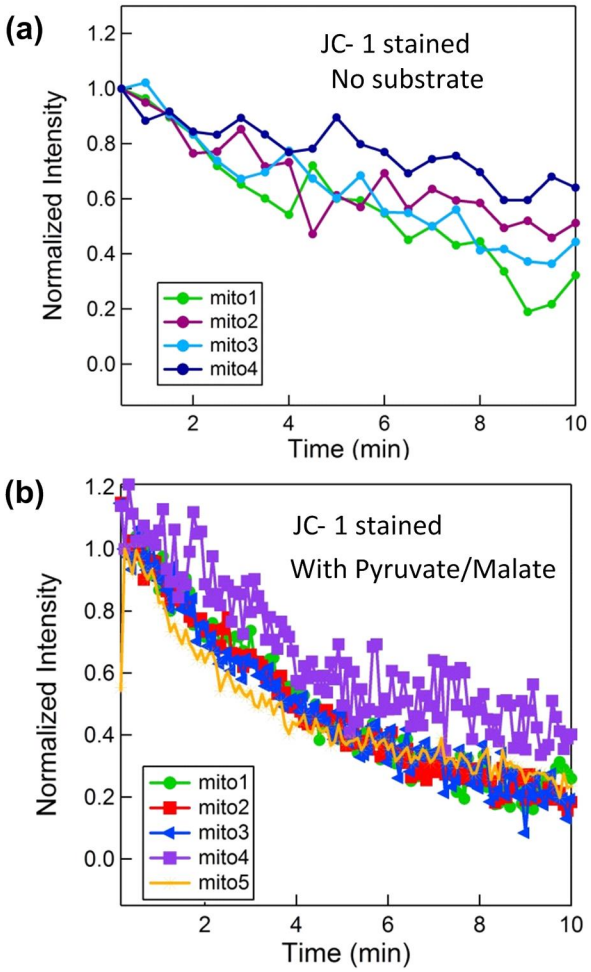

Figure 0.7. Fluorescence intensity measurement of JC-1 stained mitochondria. a) Substrates are not used. B) OXPHOS substrates (5 mM Pyruvate and 5 mM Malate) are added to respiration buffer just before flowing the mitochondria into the nanofluidic channel. This activates the electron transport chain and increases the mitochondrial membrane potential $\Delta\psi_m$ initially.

Interestingly, for one of the mitochondria (labeled mito4 in Figure 3.7 (b), we observed around 20% fluctuation in the fluorescence intensity. Fluctuations (flickering) of membrane potential of individual mitochondria from different cell types have been reported before, although the detailed conditions and causes of this flickering are not fully understood.[58,81,85,86] Our study is the first to observe such flickering in isolated mitochondria from HeLa cell line, and it is surprising that it is observed in substrate fed (rather than basal) mitochondria, which is contradictory to some other studies,[80] where removal of substrates resulted in flickering in some

mitochondria. Even though JC-1 is a slow response dye,[87] it has been shown that the observed flickering when using JC-1 is very similar to TMRM but with a slightly lower frequency.[88] It is our belief that the technique demonstrated herein could be useful for future studies to more quantitatively elucidate the flickering of the membrane potential, its causes, and modulators.

Calcium Induced MMP

Calcium in mitochondrial matrix controls the rate of energy production. In case of pathological calcium overload mitochondrial permeability transition pore opens irreversibly causing the mitochondria membrane to become abruptly permeable. This results in mitochondrial depolarization and swelling.

A solution of 10 mM $CaCl_2$ in DI water was prepared and diluted 10 times in respiration buffer to the final calcium concentration of 1 mM. The osmolarity of the final respiration buffer solution with 1 mM $CaCl_2$ is about 310 mOsm, which is well within the physiological osmolarity range for mitochondria.[89,90] We used a very high concentration of Ca^{+2} to make sure that the amount of calcium that reaches the mitochondria is enough to cause the swelling. The solution was pumped into the channels (with a relatively low flow rate of 5 μL $hour^{-1}$ to make sure it will not dislodge the trapped mitochondria) to induce depolarization. In order to avoid the photobleaching of JC-1, we imaged the mitochondria prior to the introduction of Calcium solution, started Calcium flow, stopped the light exposure and waited for 4 minutes. Then we turned on the illumination and imaged the same field again. (Figure 3.8) The red/green fluorescence intensity of most of the mitochondria had considerably decreased. This clearly indicates the membrane potential has been significantly reduced by the Ca^{2+}.

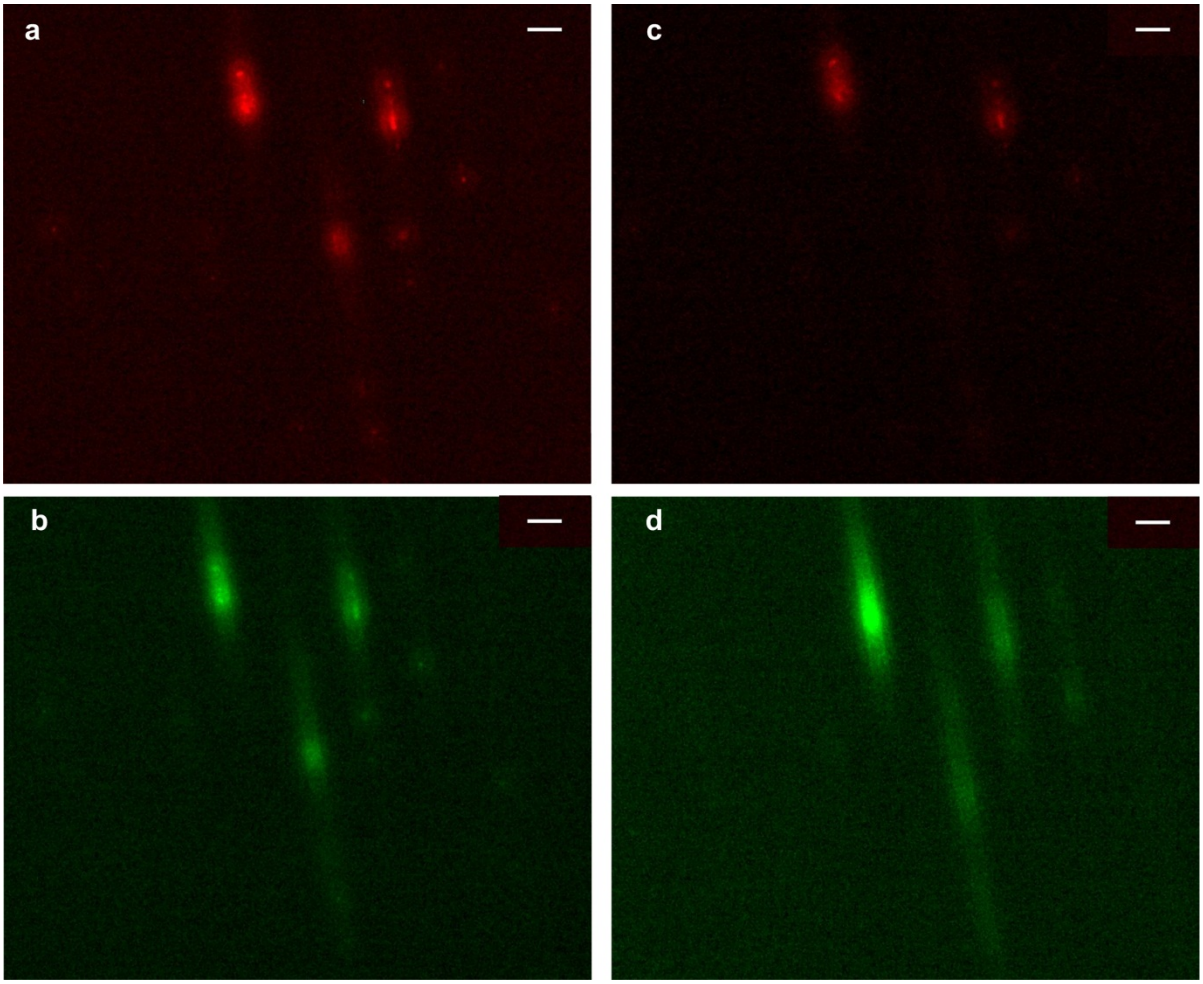

Figure 0.8. (a) and (b) Trapped mitochondria before flowing the respiration buffer with1mM Ca+2 in the channels. (c) and (d) Same mitochondria after exposure to 1mM calcium flow. Scale bar is 5 µm.

To quantify this effect, we compared the red fluorescence to green fluorescence intensity ratio prior to and after calcium treatment. The red/green ratio for all 14 mitochondria varied, but shifted to a lower value after introduction of the Calcium. In Figure 3.9, the histograms of the ratios (which is indicative of the membrane potential $\Delta\psi_m$) for the pre and post Calcium treatment are plotted. Interestingly, the results indicate the membrane potential has collapsed for all but one mitochondrion, regardless of the initial membrane potential (i.e. red/green ratio). This demonstrates the ability to study heterogeneity and statistical properties of individual mitochondria.

Comparison to State of the Art

The vast majority of assays performed on mitochondrial function are on large quantities of mitochondria, typically requiring 10^7 cells worth of sample.[87] Below we compare our work with prior art for the analysis of individual mitochondria, of which there are only a few techniques, none of them suitable for the studies envisioned with our technology.

An alternative technique to immobilize isolated mitochondria involves adhesion to a glass microscope slide.[91–93] This technique allows visualization and characterization of up to hundreds of individual mitochondria in a single field of view. A disadvantage of this approach, however, is the large fluorescence background of the fluorophore outside of the mitochondria. If one seeks to quantitatively determine $\Delta\psi_m$ using potential sensitive dyes, it is necessary to carefully measure the ratio of the dye fluorescence intensity at the inside to the outside of the mitochondria. The measurement is complicated by the large diffuse fluorescence background of the fluorophore outside of the mitochondria. In our nanochannels, the volume of solution outside the mitochondria is minimized, leading to much lower background fluorescence. Another advantage of our method is that mitochondria are physically trapped and cannot move around or move out of the plane of focus, allowing us to do accurate measurements. In glass immobilization method a large portion of the mitochondria do not stably get attached on the glass surface, preventing the accurate measurement of their fluorescence intensity since small movements of mitochondria will result in changes in the measured fluorescence intensity and disrupt the measurement. More importantly, parallel processing of multiple analytes is not possible on glass slide. In the fluidic channel array, it is possible to provide a large variety of different chemical environments (one in each channel) with suitably designed on-chip microfluidic circuits. For example, each of the 10 channels could be given a linearly varying

concentration of Ca^{2+} by suitable design of a perpendicular microfluidic Ca^{2+} gradient at the introduction of each channel. This could allow for parallel screening in response to different calcium concentrations at the single mitochondria level, which the glass slide approach cannot easily provide. Generalizations to arbitrary chemical combinatorial conditions are clearly possible.

Several studies have demonstrated the application of flow cytometry to the analysis of individual mitochondria.[94,95] Flow cytometry has the advantage of using existing commercially available instruments. Flow cytometry provides a "snap shot" of a single mitochondrial state (*e.g.* JC-1 fluorescence, forward scatter and side scatter). In this way, statistical analysis of mitochondria under various conditions and states can be obtained. Flow cytometry cannot be used to track the status of individual mitochondria over a long time. In contrast, in our approach, the response of individual mitochondria to a variety of chemical species can be tracked over a long period of time.

Similar to flow cytometry, capillary electrophoresis with laser-induced fluorescence detection allows for analysis of single mitochondria. In this technique, a 50 μm capillary guides individual mitochondria which migrate in response to a high electric field (*ca.* 200 V cm^{-1}). Using this technique, a variety of mitochondrial properties can be assayed, such as the electrophoretic mobility, the cardiolipin content, and ROS production.[96–101] As in flow cytometry, single mitochondria are analyzed at a snapshot in time as they migrate passed the detection window.

In short, the current approach supplies temporal information, the CE provides chemical information and the flow cytometry provides statistics on large populations.

Conclusion

We present for the first time a nanofluidic chip to trap and study isolated individual mitochondria. This provides a powerful stage for fluorescence imaging of isolated mitochondria in a controlled environment and real time investigation of their behavior under influence of different chemicals. Multiple applications of the new technology can be envisioned. We expect that the application of this and similar technologies to the analysis of sub-cellular organelles will have a variety of applications in cancer biology, stem cell biology, drug screening, and aging studies, because of the growing consensus of the general importance of functional metabolomics in biology and medicine.

Acknowledgements

This work was supported in part by the following grants awarded to D.C.W.: NIH-AG24373, NS21328, AG13154, DK73691, CIRM Comprehensive Grant RC1-00353, and a Doris Duke Clinical Interface Grant 2 005 057. P.B. acknowledges support of this work from NIH National Cancer Institute Grant 1R21CA143351-01, as well as support from the ARO (MURI W911NF-11-1-0024).

This chapter is a partial reprint of the material as it appears in (Zand, K., Pham, T., Davila, A., Wallace, D. C., & Burke, P. J. (2013). Nanofluidic platform for single mitochondria analysis using fluorescence microscopy. *Analytical Chemistry*, *85*(12), 6018–25). The co-authors listed in this publication directed and supervised research which forms the basis for this chapter.

This chapter is a partial reprint of the material as it appears in (Pham, T., Zand, K., Wallace, D. C., & Burke, P. J. (2015). Fluorescence analysis of Single Mitochondria with nanofluidic Channels, Mitochondria Medicine:Volume I, Probing Mitochondrial Function, pp 35-46, Springer New. The co-authors listed in this publication directed and supervised research which forms the basis for this chapter.

CHAPTER 4: CRISTAE REMODELING CAUSES ACIDIFICATION DETECTED BY INTEGRATED GRAPHENE SENSOR DURING MITOCHONDRIAL OUTER MEMBRANE PERMEABILIZATION

Overview

The intrinsic apoptotic pathway and the resultant mitochondrial outer membrane permeabilization (MOMP) via BAK and BAX oligomerization, cytochrome c (cytc) release, and caspase activation are well studied, but their effect on cytosolic pH is poorly understood. Using isolated mitochondria, we show that MOMP results in acidification of the surrounding medium. BAK conformational changes associated with MOMP activate the OMA1 protease to cleave OPA1 resulting in remodeling of the cristae and release of the highly concentrated protons within the cristae invaginations. This was revealed by utilizing a nanomaterial graphene as an optically clear and ultrasensitive pH sensor that can measure ionic changes induced by tethered mitochondria. With this platform, we have found that activation of mitochondrial apoptosis is accompanied by a gradual drop in extra-mitochondrial pH and a decline in membrane potential, both of which can be rescued by adding exogenous cytc. These findings have importance for potential pharmacological manipulation of apoptosis, in the treatment of cancer.

Introduction

The intrinsic mitochondrial pathway of apoptosis is an important target for pharmacological manipulation for a variety of diseases including cancer[23,102–107]. This pathway is regulated by the BCL-2 family proteins[22] and results in the collapse of the inner membrane electrochemical gradient. An early step in the initiation of the intrinsic apoptosis pathway is the mitochondrial outer membrane permeabilization (MOMP). MOMP can be induced by BH3-only proteins such as tBid and BIM and has been proposed to result from the oligomerization of pro-apoptotic BCL-2 family proteins BAX and BAK[22]. BAX and BAK oligomerization activates the metalloprotease, OMA1, to cleave the inner membrane protein OPA1[108]. OPA1 tethers the inner membrane cristae loops together at cristae junctions creating the inter-cristae luminal spaces into

which the electron transport chain pumps protons during oxidative phosphorylation (OXPHOS)[109]. Cleavage of OPA1 results in remodeling of the cristae and the opening of the proton-rich cristae luminal spaces[108,110]. MOMP permits the release of stored inter-membrane space pro-apoptotic proteins including cytochrome c (cytc), procaspase-9, and Smac/DIABLO into the cytoplasm, causing activation of caspases and the commitment to cell death.

It has been reported that the cytosol becomes acidified soon after the intrinsic apoptosis pathway is activated[111–113]. However, there has not been a method to quantify and thus understand the molecular and physiological basis of this phenomenon.

Here, we present an electronic method to detect extra-mitochondrial pH of isolated mitochondria, based on tethering the mitochondria to one-atom thin graphene. The mitochondria are tethered via graphene bound antibodies which recognize the mitochondrial outer membrane protein, TOM20. Graphene is an excellent conductor and changes in the pH surrounding the mitochondria can change the graphene conductance and be detected electrically. Being optically transparent, the graphene layer also permits optical interrogation of the mitochondria[72,87,114] concurrent with analysis of ionic changes. Hence, our system permits the simultaneous monitoring of changes in extra-mitochondrial pH through graphene conductance and inner membrane potential ($\Delta\Psi m$) using the potentiometric fluorescent dye tetramethylrhodamine ethyl ester perchlorate (TMRE).

Results

An overview of our experimental system is shown in Fig. 4.1. After the graphene device is fabricated and prepared, purified mitochondria can be tethered to the anti-TOM20 antibodies. The graphene conductance then permits the electronic detection of mitochondrial ion exchange and the optical properties of the graphene permit the staining and visualization of the

mitochondrial membrane potential.

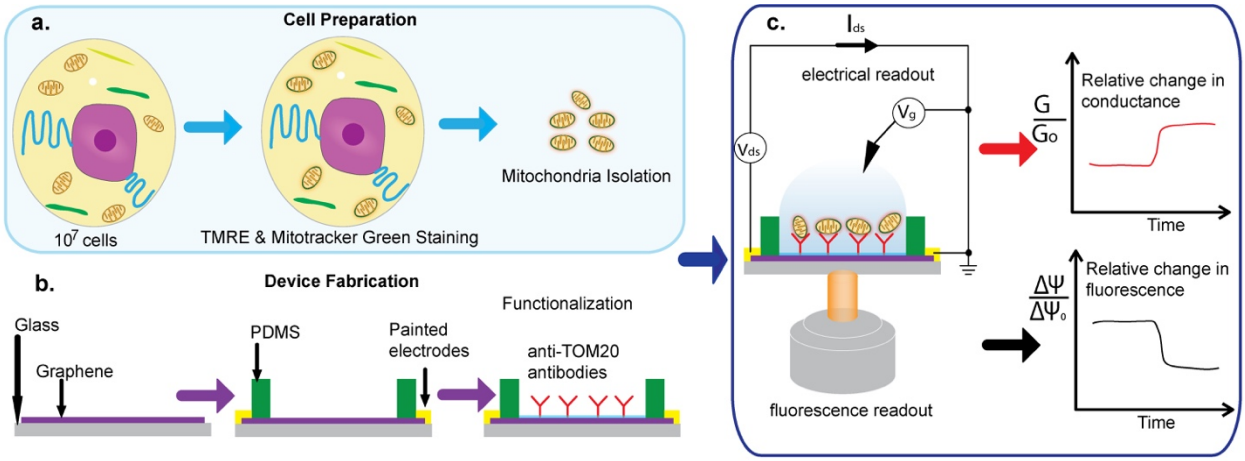

Figure 0.1: Overview of the experimental workflow. (a) Mitochondria are isolated on the day of experimentation and loaded on (b) a pre-functionalized device. (c) After a brief incubation, mitochondrial functions can be probed via electrical and fluorescent methods.

We used a bottom-up approach to deposit several layers of chemistry on the graphene surface (Fig. 4.2a). Starting with the base layer of chemical vapor deposition (CVD)-grown single-layer graphene[115] directly transferred on a glass slide, we incorporated 1-pyrenebutanoic acid succinimidyl ester (pyrene-NHS) as a linker between graphene and anti-TOM20 antibody. While pyrene exhibits a strong pi-pi interaction with the graphene, NHS provides a terminal for amide bonding of antibodies. Since TOM20 is a subunit of the translocase of outer membrane, anti-TOM20 antibody can be used to attract mitochondria[116]. Anti-TOM20 antibodies were incubated and allowed to bond with the pyrene-NHS linker. After antibody incubation, ethanolamine was added to inactivate the NHS remaining ester bonds. Finally, TWEEN20 was added to passivate the exposed graphene area, effectively shielding the exposed graphene surface from unspecific protein adsorption.

After functionalization, the device was washed with KCl buffer (140 mM KCl, 2 mM MgCl2, 10mM NaCl, 0.5mM EGTA, 0.5mM KH2PO4, 2 mM HEPES, 5 mM succinate, 2 µM

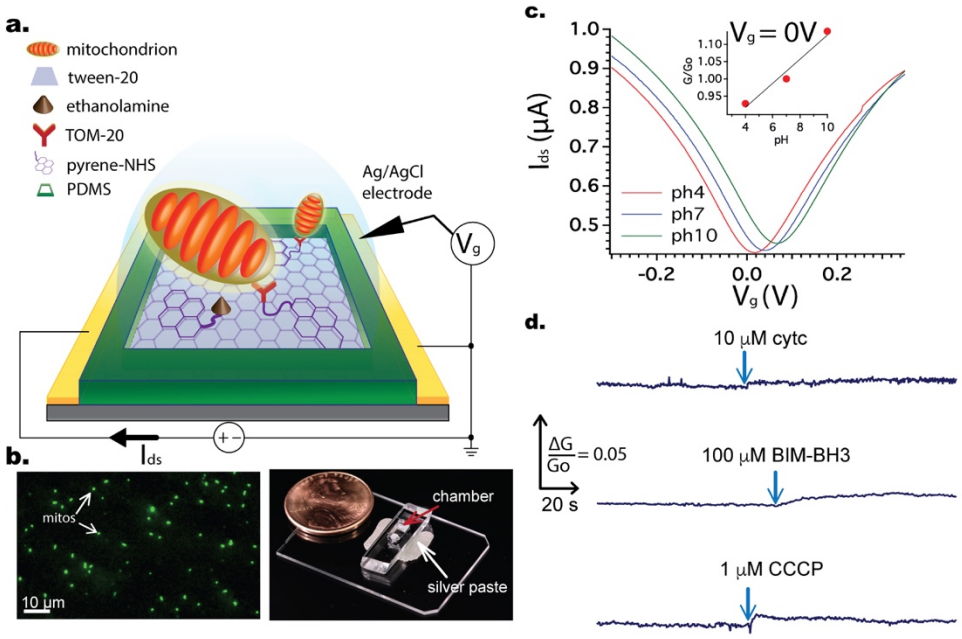

Figure 0.2: (a) Overview of the functionalization scheme (Mitochondria not to scale); (b) Immobilized mitochondria (from HeLa cells) on functionalized graphene surface, false colored from 100 nM MitoTracker® Green FM signals. A finished graphene-on-glass device; graphene is at the bottom of the chamber indicated by the red arrow; (c) I_{ds} vs V_g (electrolyte gate) characteristics with different pH KCl buffers; (b). Insignificant fluctuations of graphene conductance following the additions of various substrates.

rotenone, pH 7.2 adjusted with KOH) twice before 40 µl of 0.14 µg/µl isolated HeLa mitochondria (0.07 µg/µl for RS4;11) was incubated in the device's chamber for 15 minutes at 4°C. After incubation, the device was gently washed with fresh KCl buffer and then mounted on the inverted microscope. Because graphene was directly transferred on the glass slide, the focusing distance from the objective to the graphene was minimal, allowing visualization of single isolated mitochondria with fluorescence stains such as MitoTracker® Green FM. Figure 4.2b shows mitochondria, previously stained with MitoTracker® Green FM, are immobilized on top of the graphene layer at the bottom of the device. Gentle insertions of experimental reagents did not disturb the mitochondria. In a similar fashion, a graphene device without anti-TOM20 antibody or just bare graphene was incubated with isolated mitochondria but did not result in any mitochondria attachment on the graphene surface after the wash step.

The density of mitochondria attachment was calculated to be 4237 ± 279 mitochondria/mm2 for HeLa cells and 1418/mm2 ± 328 for RS4:11 cells; the sample sizes were three. We used ImageJ particle analysis to count the number of mitochondria within 0.25-1 μm2 under the assumption that a mitochondrion's area would fall in this range. Since the chamber's bottom area is 20 mm2, we can compute that a device would have approximately 85,000 mitochondria at the upper limit. If we assumed that 1 μg of mitochondrial protein yields 106 particles of isolated mitochondria[51], after washing, our device would require at most 0.1 μg of mitochondrial protein. This quantity is much smaller than the number of mitochondria that would be included in more conventional solution biochemistry assays, ranging from 3-20 μg mitochondrial protein for assays of cytc release[117], single mitochondria membrane potential[80], and respiration studies[24]. In addition, this work pushes the minimal mitochondrial quantity requirement even further compared with our previous reports[73,118], which used 0.75 μg of mitochondrial protein per assay. Using our typical yield of 140 μg mitochondrial protein from 107 HeLa cells, 0.1 μg of mitochondrial protein amounts to around 7000 cells worth of mitochondria, a slight improvement to the 10,000-cell requirement imposed for plate-based assays of mitochondrial functions[114].

Functionalized Graphene devices are pH-sensitive, but insensitive to CCCP, BIM-BH3, and cytc, and are only mildly sensitive to succinate and K+ ions

We measured the depletion curves, defined as the graphene current vs. electrolyte gate voltage curve (Ids vs. Vg), of the functionalized graphene devices with KCl buffer at different pH values. 1 M HCl and 1 M KOH were used to adjust the pH of the KCl buffer from pH 4 to 10. Figure 4.2c shows that the depletion curve shifts right with increasing pH, and at zero gate voltage the current increases. The gate in these experiments is the electrolyte (buffer) in the

chamber. The pH sensitivity of graphene is consistent with previous reports[119,120]. From the inset of Fig. 4.2c, at zero gate voltage an increase in one unit change in pH corresponds to approximately 4% increase in conductance. This calibration, however, only applies to functionalized devices without mitochondria. For the devices with tethered isolated mitochondria, the situation is more complicated and is discussed in Supplementary Fig. 4.3.

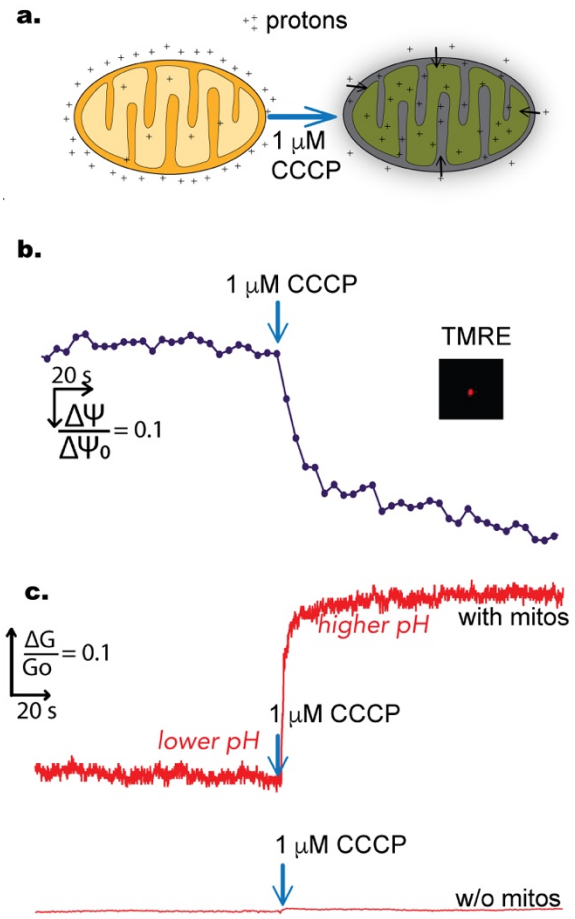

Figure 0.3: a) Illustrations of protons movement after CCCP addition; (b) Time-lapse of TMRE fluorescence, an indicator of the mitochondrial membrane potential, before and after the addition of CCCP; (c) The corresponding change in graphene conductance (measured simultaneously with the fluorescence) and the control; after CCCP, the concentration of protons changes dramatically in the extra-mitochondrial buffer.

Additionally, we carried out a series of control experiments to confirm that the dominant response of the graphene was to pH, and not other chemicals used in the buffer or likely to have been modified by the mitochondria (Fig. 4.2d.). Having established a relatively low sensitivity of

graphene to experimental substrates (as compared to the pH sensitivity), we set out to test the graphene response in the presence of isolated mitochondria.

CCCP causes ΔΨm to decrease and buffer pH to increase

The mitochondrial proton motive force is defined as $\Delta p = \Delta\Psi m - 59\Delta pH$, where ΔΨm denotes the mitochondrial inner membrane potential and ΔpH indicates the proton gradient across the inner membrane. The mitochondrial inner membrane potential can generally be monitored by lipophilic cations or indicator dyes. We chose 40 nM TMRE[121] as the membrane potential indicator. The concentration of the charged dyes (in this case, TMRE) changes with membrane potential in accordance with the Nernst equation (1), which states the concentration ratio is given by:

$$\frac{[TMRE]_{in}}{[TMRE]_{out}} = e^{-\frac{\Delta\Psi_m}{kT}} \quad (1)$$

This means at higher potentials (defined as the matrix is more negative), more TMRE accumulates inside the mitochondrial matrix. As a result, TMRE fluorescence intensity from inside the mitochondria can indicate qualitatively the mitochondrial membrane potential i.e. the higher the intensity, the higher the membrane potential. Assessing ΔΨm quantitatively requires the TMRE intensity outside of the mitochondria[74,87]; however, most studies on mitochondrial membrane potential report only the TMRE intensity inside the mitochondria[58,122]. In addition to TMRE fluorescence, we performed concurrent electrical detection on the isolated mitochondria using graphene and correlated the electrical signal to the observed fluorescent readout. The experiments were performed in the dark with the excitation LEDs intermittently turned on to monitor TMRE fluorescence. Hence, graphene photo-conductance was minimal and no interference from the LEDs was observed from the recorded electrical signal.

Figure 4.3 shows the normalized change in both the graphene conductance and TMRE signal after the addition of 1 μM CCCP, a strong uncoupling agent that can abruptly depolarize the membrane potential. CCCP works as an efficient proton transfer agent that effectively short circuits the proton (pH) gradient as well as the membrane potential (charge gradient). Compared to the starting fluorescence, after addition of CCCP, the fluorescent signal, defined as TMRE intensity of one mitochondrion, dropped about fifty percent. At the same time, the graphene conductance increased by almost twenty percent, indicating a buffer pH increase.

The results for the CCCP experiment were reproduced five times yielding a statistics of increased conductance at 13 ± 8 %. The average reduction in TMRE intensity after CCCP addition was 69 ±7% (N=3). In addition, we also performed the same experiment but with another, albeit weaker, uncoupling agent namely 10 μM 2,4-Dinitrophenol and observed a similar change in electrical and fluorescence signals (Supplementary Fig. 4.4). Meanwhile, the control electrical experiments, performed on the same day with the other experiments on identically fabricated devices but without any mitochondria, yielded at most 0.8% difference in graphene conductance.

In order to confirm the alkalization of the buffer on CCCP addition, and to rule out the possibility that the graphene pH response was an artifact of the relatively novel and new graphene pH detector in the context of tethered mitochondria, we used a traditional, commercial pH meter to measure the pH change in a mitochondrial suspension. The response time of the pH meter was around 3 seconds. We diluted 200 μg isolated HeLa mitochondria in 2 mL of KCl buffer and measured the pH with an Oakton Instruments pH meter and an OrionTM ROSS pH electrode. Before CCCP, our buffer pH was 7.21± 0.01 which increased to 7.23 ± 0.01 after

CCCP (N=3). Although this measurement was right at the limit of the sensitivity of the commercial pH meter, the results were consistent with our much more sensitive graphene results.

BIM-BH3-induced MOMP causes oligomycin-independent buffer acidification (↓ pHbuffer) and ΔΨm decay

We utilized BIM-BH3 peptide (derived from BIM protein, see Methods for sequence) as a known activator of BAX/BAK to induce MOMP. In whole cells, BAX is soluble in the cytosol while BAK is present on the outer membrane. In our experiments, because we used isolated mitochondria where only BAK is present and no BAX in the buffer, BIM-BH3 could only affect BAK. Previous studies[22,105,123] have demonstrated that BIM-BH3 can directly induce BAK homo-oligomerization, which forms pores in the mitochondrial outer membrane causing MOMP, leading to the release of cytc and other pro-death factors with a side effect being the eventual collapse of the inner membrane potential. The experiments by Letai and colleagues[105] tested BIM-BH3 on wildtype and BAK deficient liver mitochondria and demonstrated that BIM-BH3 activates BAK oligomerization. Because BIM-BH3 can cause MOMP, one potential concern is that BIM-BH3 can disrupt the binding between the antiTOM20 antibodies and the mitochondria, thus releasing the mitochondria away from the graphene surface. This possibility is unlikely, however, since BIM-BH3 can integrate into the outer membrane without TOM20[124].

Also for the experiments with BIM-BH3, we chose RS4;11 isolated mitochondria due to their well-demonstrated outer membrane composition of BCL-2 family proteins particularly BAK[125]. Addition of CCCP to RS4;11 mitochondria caused a comparable increase in buffer pH as seen for HeLa cell. Upon introduction of 100 μM BIM-BH3 to the RS4;11 mitochondria, we observed a distinct acidification of the buffer (measured via decreased graphene conductance, Fig. 4.4a), a result confirmed with HeLa mitochondria as well as a decline in the membrane

potential (Fig. 4.4b). Both of these effects were observed with and without 2 μg/ml oligomycin (which blocks the transport of protons by ATP synthase) in KCl buffer

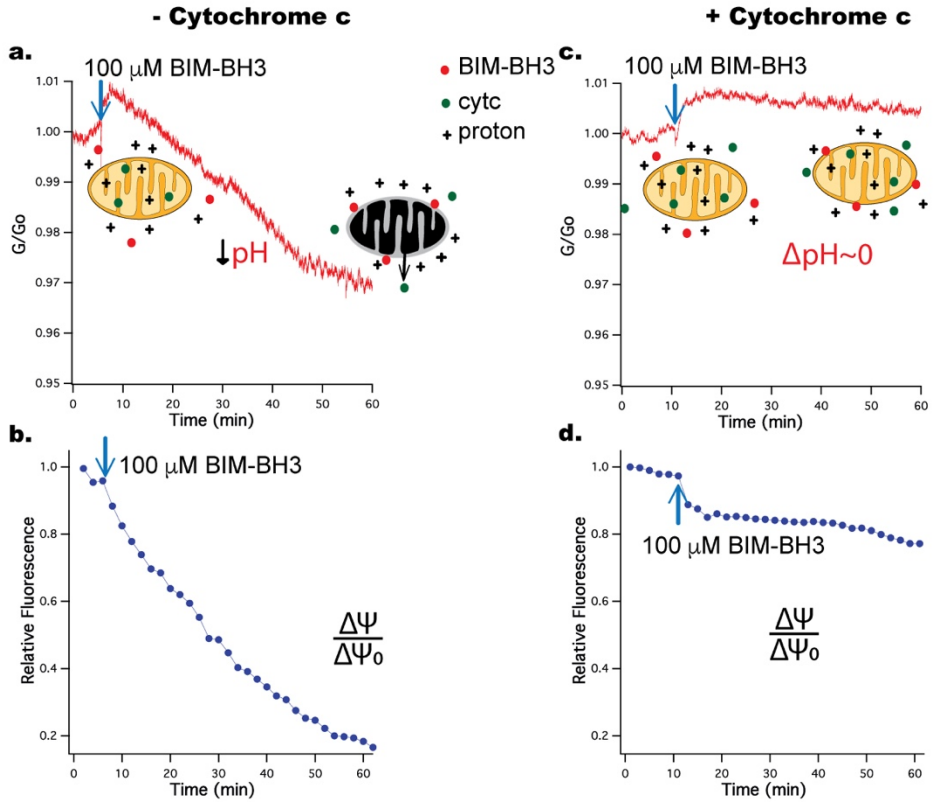

Figure 0.4: (a, b) Addition of 100 μM BIM-BH3 causes graphene conductance and membrane potential to decrease. The fluorescence signal was defined as the average of three mitochondria. Results are representative of three independent experiments. (c,d) A similar experiment with 100 μM BIM-BH3 but with 10 μM cytc added to the buffer. The results show less reduction in both graphene conductance and membrane potential. Results are representative of two independent experiments.

The induced pH changes following BIM-BH3 addition occurred over a longer timescale than that resulting from CCCP exposure.

Again, as a check to confirm that the measured acidification was not an artifact of the novel graphene biosensor, we measured the buffer pH with a commercial pH meter on introduction of BIM-BH3 to a mitochondrial suspension (140 μg of RS4;11 mitochondria in 500

μL total volume) under otherwise identical conditions. Our measurements showed an average pH reduction of 0.05 ± 0.01 (N=3) after 60 min of incubation with the peptide.

Exogenous cytc blocks buffer acidification and rescues ΔΨm after BIM-BH3 induced MOMP

During MOMP, cytc is released to the buffer so the lack of cytc results in loss of cytc mediated electron transfer between complex III and IV in the electron transport chain (ETC). This stalls the ETC, leading to a gradual decline in membrane potential and loss of respiration[126–128]. Consistent with this hypothesis, following MOMP, respiration can be restored by adding exogenous cytc[127–129]. Motivated by this observation, we decided to test the effect of exogenous cytc on buffer acidification and membrane potential in our system. The presence of cytc in the buffer does not affect the graphene sensor (Fig. 4.2d).

We tested the effect of including 10 μM cytc in the buffer on the graphene signal upon treating the mitochondria with 100 μM BIM-BH3 (Fig. 4.4 c,d). The addition of exogenous cytc following BIM-BH3-induced MOMP blocks the decline of TMRE fluorescence (or ΔΨm) and also greatly reduces the effect of buffer acidification. To our knowledge, this inhibition of buffer acidification by exogenous cytc following MOMP is a new observation for isolated mitochondria. Separate pH measurements of mitochondrial suspensions in the presence of cytc confirm this observation, showing only 0.02 ± 0.01 reduction in buffer pH with cytc as compared to 0.05 ± 0.01 ($p<0.05$ student t-test, N=3) in the case without cytc. Figure 4.5 summarizes our

experimental observations without any hypothesis about the mechanisms.

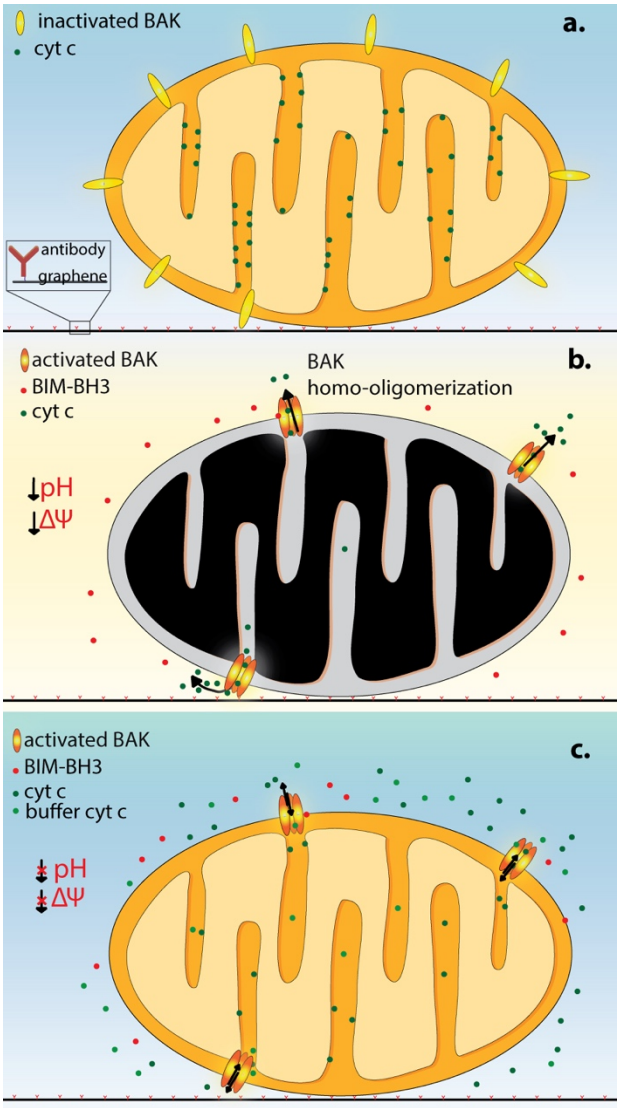

Figure 0.5: BIM-BH3-induced MOMP in tethered, vital, isolated mitochondria. The mitochondrion (0.5-1 µm in diameter) is drawn to scale with the antibody (~10 nm). (a) without BIM-BH3, BAK stays inactive; (b) with BIM-BH3, BAK is activated and oligomerize to form pores in the outer membrane, causing cytc release. This is observed to result in buffer acidification and membrane potential decline; (c) With exogenous cytc in the buffer, the mitochondrion maintains inner membrane potential with a reduced change in the buffer pH.

Discussion

We have created a novel system for assessing functional changes in mammalian mitochondria. Our system employs an optically transparent, single atom thin graphene layer onto

which the mitochondria are tethered using a graphene-bound antibody against the outer membrane protein TOM20 to which isolated mitochondria adhere. Because the graphene electrode is optically transparent, single bound mitochondria can be functionally analyzed using analytical fluorescent dyes at the same time that the mitochondrial outer membrane can be monitored in real time by changes in the conductance of the graphene. The electrical properties of the graphene have been found to detect subtle changes in the proton concentration on the outside of the mitochondrial outer membrane as the mitochondrial inner membrane electrochemical gradient changes. The acute sensitivity of this system is permitting the dissection of alterations in the mitochondrial membrane status during various mitochondrial processes such as uncoupled depolarization of OXPHOS and the induction of the intrinsic pathway of apoptosis initiated by the pro-apoptotic peptide BIM-BH3. Using our graphene biosensor platform, we have been able to make three important observations pertaining to the mitochondrial inner membrane electrochemical gradient and its changes during the BIM-BH3 initiated intrinsic pathway of apoptosis. First, we found that CCCP addition to respiring mitochondria causes buffer alkalization along with membrane potential depolarization. Second, we observed that treatment of respiring mitochondria with BIM-BH3 results in external buffer acidification and membrane potential decline. Third, we found that the BIM-BH3-induced acidification and membrane potential decline of respiring mitochondria can be blocked by the addition of exogenous cytc to the external mitochondrial buffer.

BH3.

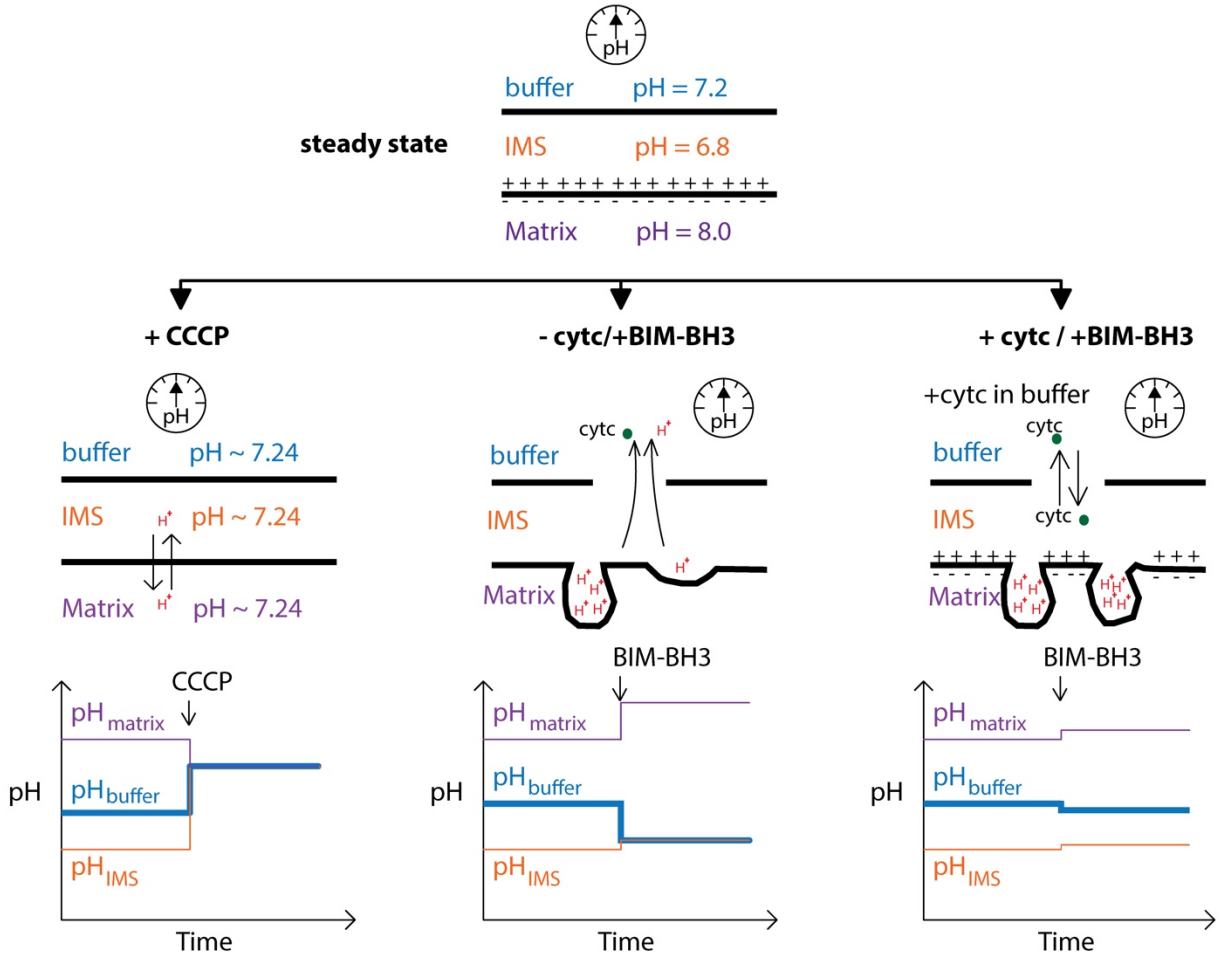

Figure 0.6: Schematic diagrams of membrane morphology and compartmental pHs for the three experiments performed. The steady state of the mitochondria is shown at the top with buffer pH (indicated as measured) and the other pHs as inferred from the literature[130,131]. In the case of CCCP, pH is equilibrated across the three compartments. The bottom shows the qualitative changes in pH vs. time (not to absolute scale) with the bolded line being the measured variable while the other lines are inferred. For the next two cases, the top two figures correspond to our proposal that the cristae remodel and release protons and cytc from the invaginations and the absence of such a mechanism when exogenous cytc is added. The bottom figures indicate again the qualitative assessment of the pHs

Our first observation of buffer alkalization can be attributed to CCCP allowing protons to rapidly enter the matrix. When immersed in isotonic buffer containing the mitochondrial respiratory chain complex II substrate, succinate, and the complex I inhibitor, rotenone, mitochondria rapidly oxidize the succinate passing the electrons from complex II, to coenzyme

Q, to complex III, to cytc, to complex IV, and finally to O2 to reduce it to H2O. The flux of electrons through complex III and IV is coupled to the transport of protons from the mitochondrial matrix out across the mitochondrial inner membrane to the inter membrane space rendering the outside of the mitochondrial inner membrane acidic and positively charged and the inside negatively charged and alkaline[21]. Addition of uncouplers to the respiring mitochondria result in the rapid flux of protons back into the mitochondrial matrix, rendering the inter-membrane space more alkaline[132–134] (Fig. 4.6). Given that the mitochondrial outer membrane voltage dependent ion channel[135] (VDAC or porin) is freely permeable to protons this would result in the pH of the surrounding buffer to become more alkaline, exactly as we observed, a result consistent with Mitchell's chemiosmosis theory[136] for oxidative phosphorylation (OXPHOS) coupling.

We propose that buffer acidification with BIM-BH3 in our second observation is caused by release of protons from the lumina created by the invaginations of the mitochondrial inner membrane. At first glance, the acidification of the surrounding mitochondrial buffer on treatment of respiring mitochondria with the inducer of the intrinsic pathway of apoptosis, BIM-BH3, would seem contrary to the chemiosmosis theory of OXPHOS. However, recent discoveries[108,110,137] about structure and function of the mitochondrial inner membrane and the changes that occur during the induction of the intrinsic pathway of apoptosis render the observation of acidification explicable.

The mitochondrial inner membrane is highly invaginated and with the tips of the invaginations closest to the outer membrane held together by the mitochondrial inner membrane integral membrane protein OPA1[109] located within the mitochondrial contact site and cristae organizing system (MICOS). This creates multiple internal lumina in which the interior of each

lumen is equivalent to the outside of the mitochondrial inner membrane. Hence, within these lumina the cytc and proton concentration can become very high.

When the mitochondrial membrane potential declines or the intrinsic pathway of apoptosis is activated mitochondrial inner membrane proteases including OMA1 become activated and cleave OPA1 resulting in the opening of the inner membrane lumina to the mitochondrial intermembrane space[108,110]. Since most of the cytc is encompassed within the lumina of the inner membrane[138,139] this process is central to the release of cytc from the mitochondria observed as the intrinsic pathway of apoptosis progresses. Because protons are much smaller in diameter than cytc, it follows that as OPA1 is cleaved, the first event is the escape of the protons into the mitochondrial inter membrane space and out through the permeabilized outer membrane and into the surrounding buffer (Fig. 4.6). This would cause the gradual acidification of the surrounding medium detected by the graphene electrodes. Treatments of the mitochondria with BH3 peptides often require 60-90 min incubation[114,140] before any functional measurements can detect a change. This time frame is consistent with the completion of the pH change that we detected with the graphene sensor which occurred at about 60 minutes.

Given that the decline in the mitochondrial inner membrane potential is an important prerequisite for the activation of inner membrane proteases and the cleavage of OPA1, it follows that the release of cytc from the mitochondrial inter membrane space following BIM-BH3 induced BAK activation could locally activate the proteases that cleave OPA1. This possibility follows from the conceptualization of the distribution of the respirasomes across the mitochondrial inner membrane. The respirasomes would fall into two categories: those that are located on the mitochondrial inner membranes that form the cristae invagination-generated lumina and pump protons into the cristae lumina and those respirasomes that are located in the

inner membrane which faces the intermembrane space. This later set of respirasomes would be responsible for maintaining the pH acidification of the intermembrane space and thus would control the activation of the outer membrane proteases that can cleave OPAI. When BIM-BH3 activates BAK to open the outer membrane, the first cytc to be released would be that in the inter membrane space resulting in localized drop in the mitochondrial membrane potential, activating OMA1, and initiating the cleavage of OPA1. Once OPA1 is cleaved the invaginated cristae lumina would open to the inner membrane space and the remaining cytc would be released stopping all further respiration. Addition of exogenous cytc to the medium surrounding the mitochondria would sustain the respiration required for maintaining the intermembrane space pH and membrane potential thus stabilizing OPA1 and blocking detectable changes in proton and cytc release (Fig. 4.6), which is our third observation.

Although previous studies have shown that cytosolic acidification is associated with apoptosis in whole cells[111,112,141], its role, timing, and mechanism has remained until now a mystery. One proposed mechanism (ATP synthase reversal[113]) has been ruled out on thermodynamic grounds[142]. Our observation of acidification even in the presence oligomycin (which blocks ATP synthase activity) also rules out ATP synthase involvement. Furthermore, our results provide a plausible mechanism that is consistent with recent discoveries of OMA1/OPA1 based cristae remodeling, Although it is generally believed that mitochondria remodel during apoptosis[143], to directly measure cristae structure during apoptosis is technically challenging, and beyond the scope of this work. Our hypothesis that cristae remodeling causes buffer acidification is the most consistent hypothesis with our data, as well as all of the data in the literature on this subject[143].

Furthermore, it is still highly plausible that the physiological role of pH change is to enhance caspase activities during apoptosis, as the caspases are known to have pH-dependent activation[141]. These questions have led to a "renaissance" of interest in mitochondrial pH[144]. In addition, because the tumor microenvironment also exhibits significant pH alterations, studying mitochondrial mediated pH changes would make for fruitful future studies.

As with any new bio-assay technology, it is important to benchmark results against known standards, and to compare and contrast advantages and disadvantages of the new vs. traditional methods. For pH sensing, there are two traditional approaches: Electrochemical sensors and genetically encoded pH sensitive fluorescent proteins such as pHluorin, SypHer, and pHred. We have chosen to benchmark our results against a conventional pH meter (Oakton Instruments pH meter and an OrionTM ROSS pH electrode), and found the results to be consistent. We found this to be more expedient than engineering a separate strain with pH sensitive fluorescent proteins. However, the conventional pH meter has barely sufficient pH resolution (0.01 pH) and a slow response time, as compared to our integrated graphene detectors. Consequently, we had to use significantly more sample (140 μg vs 0.1 μg) with the pH meter, and probably because of 0.01 pH resolution we could only detect pH changes after 60 min of mitochondrial incubation with BIM-BH3. In contrast, the intimate contact between the graphene and the mitochondria allows our graphene devices to detect an estimated 4.0x10-4 relative change in pH unit (Supplementary Information) with 0.2 s temporal resolution. The enhanced sensitivity comes with a drawback that the pH calibration for the graphene devices is not absolute (Supplementary Information).

In principle, a genetically engineered mitochondrial pH sensor based approach has the advantage that an absolute calibration can be performed for pH sensing. However, this approach

has resulted in some uncertainties in the literature about the proton motive force dynamics during apoptosis[113],49.. Still, recent advances in live cell imaging have enabled detailed (and calibrated) studies of mitochondrial and cytosolic pH under different metabolic conditions[145,146]. While advantageous in many ways, genetically encoded mitochondrial pH sensors do have some disadvantages, including restricted applicability to established transformed cell lines.

What our ultrasensitive graphene system for analyzing isolated mitochondria has revealed is a model where there are two totally different mitochondrial inner membrane electrochemical gradients. One of these is the proton gradient between the mitochondria matrix and the intermembrane space. This gradient appears to be an important mediator for the regulation of OMA1 and the resulting regulation of OPA1 cleavage, the important factor in linking the opening of MOMP with the initiation of the intrinsic pathway of apoptosis. However, the second inner membrane electrochemical gradient is between the mitochondrial matrix and the enclosed lumina of the cristae invaginations which are isolated from the intermembrane space electrochemical gradient by closure of the cristae lumina by MICOs and OPA1. This structure potentially permits a much higher concentration of protons to be generated, since the pH cannot be buffered by the cytoplasm surrounding the mitochondrion. Furthermore, by confining the protons in a small volume, the electrostatic potential can be much higher increasing the energetic capacity of the system.

In conclusion, by taking advantage of our ability to study isolated mitochondria using our graphene sensor, we have been able to separate two fundamentally different classes of mitochondrial inner membrane, respirosomes, and electrochemical gradients, resulting in a strikingly new perspective of the role of the mitochondrial electrochemical gradient and thus of the biophysics associated with the Mitchell's chemiosmosis hypothesis[136].

The development of the graphene-based system for monitoring changes in the mitochondrial function permitted us to investigate events associated with mitochondrial OXPHOS coupling and the intrinsic pathway of apoptosis. However, we have only begun to monopolize on the exquisite time and sensitivity resolution that our new system permits. Further miniaturization of the technology from millimeter to micrometer dimensions (a straightforward process using photolithography) could enable assays on single mitochondria. In addition to the studies presented herein, this platform could enable new studies of mitochondrial biology and medicine that were heretofore inaccessible. The first possibility is the parallelization from one to thousands of on-chip devices. Such a system could permit for the first time the analysis of 1) mitochondrial heterogeneity within a single cell, say as mtDNA mutations in heteroplasmy[28] leading to functional heterogeneity, an unexplored frontier in mitochondrial biology; 2) massively parallel screening for peptides and drugs that could modulate mitochondrial respiration or the intrinsic pathway of apoptosis. For example, it has recently been shown that mitochondrial sensitivity to apoptosis/MOMP/cytc release in response to chemotherapies in tumor biopsies (in vitro) is directly correlated with patient survival rate[147]. Further investigation has led to a proposed "profile" of each tumor, defined as its qualitative response (defined as cytc release) to a panel of peptides, entitled "BH3 profiling"[114]. Another potential application is high temporal resolution, high pH resolution studies of mitochondrial flashes[146,148]. The role of these flashes, and their relationship to signaling pathways, metabolism, bioenergetics, apoptosis and the mitochondrial permeability transition pore is only now beginning to be understood.

Methods

Graphene transfer and device fabrication

Graphene was transferred on to glass substrates using a modified protocol from what we described previously[115]. Briefly, a 5 cm x 5 cm copper foil containing CVD grown single-layer graphene on one side was cut into 0.6 cm x 1.0 cm sheets. The side of the sheet containing graphene was pressed lightly against a block of pre-cured PDMS. The Cu-graphene-PDMS structure was then placed and left floating in a Cu-etchant bath (5 mg/ml ammonium persulfate in DI water). After the copper was completely etched away, the graphene-PDMS structure was washed three times with DI H2O for one hour to eliminate any residual ions from the copper etching step. The wet PDMS/graphene block was then pressed against a 1-mm thick glass slide that had been cleaned for one hour with 1:3 (v/v) H2O2: H2SO4 solution. The glass-graphene-PDMS slide was kept under a slight pressure overnight to promote graphene-glass adhesion and allow the interfacial water to evaporate. When the device was completely dry, the PDMS was carefully peeled off, leaving large-area single-layer graphene on the glass slide. Although many transfer steps were essentially similar to the protocol[115], the deposition of graphene directly on glass was the modification in the study.

Following graphene transfer, we needed to create an experimental chamber on top of the graphene, fabricate drain and source electrodes to measure the graphene in-plane conductance, and insulate the electrodes from the experimental liquid. To accomplish these goals, a simple, freshly cured PDMS slab with an inner cut-out was placed directly on top of the graphene (Fig. 4.2b). Specifically, the cutout, measured 4 mm x 5 mm x 3 mm in length x width x height, serves as the experimental chamber. Additionally, due to having narrow width, the PDMS slab, although covering most graphene area, still leaves some exposed graphene where quick-dry silver paste (Ted Pella) can be painted to establish electrical connection. As depicted in Fig. 4.2b, the silver paste electrodes are conveniently insulated from the experimental chamber.

Graphene functionalization

After the silver-paste electrodes were completely dry, graphene functionalization was carried out using a series of solution deposition, incubation and wash. Each step in the series employed 50 μL volume. First, 3.81 mg of pyrene-NHS was mixed with 2 mL dimethylformamide (DMF), and added to the PDMS chamber of each graphene device. Incubation with pyrene-NHS ensued for one hour at room temperature. The device was then washed sequentially with fresh DMF, DI water and PBS pH 7.2. Anti-TOM20 antibody (Santa Cruz Biotechnology) solution is added at 33.3 g/mL concentration and incubated overnight at 4°C. After two wash steps with PBS then DI H2O, 0.1 M ethanolamine diluted in DI H2O was added and incubated for one hour at room temperature then washed with DI H2O. The next incubation with 0.1% TWEEN-20 was set for one hour at room temperature to deactivate the exposed graphene area by preventing unspecific protein adsorption. The functionalization scheme was partially adapted from[149]. Finally, the devices were washed with DI H2O then KCl buffer for immediate use.

While the fabrication and functionalization steps might at first seem straightforward, our device yield was around fifty percent. The limiting factor here was the bonding strength between the final PDMS and glass slide, which often resulted in leakage at the DMF step or the overnight incubation at 4°C. DMF is an organic solvent, which might affect the integrity of PDMS; hence, we remedied by taking extreme care not to spill the solvent anywhere outside of the chamber. Furthermore, we attributed the failing rate at 4°C step to the humidity inside the refrigerator, so putting the device in a desiccator did increase our yield. We consider fifty percent yield was reasonably robust for our experiments because we would have at least three working (with electrical connections and no liquid leakage) devices on the days of the experiment.

Cell culture

The mammalian cell lines: HeLa and RS4;11 (American Type Culture Collection) were maintained in the log growth phase using the appropriate tissue culture protocols for adherent and suspension cells, respectively. All cell culture related supplies such as media, fetal bovine serum, PBS pH 7.2, mitochondria staining dyes and trypsin were obtained from Life Technologies. On the days of the experiment, 107 cells were typically harvested for mitochondria isolation. We used more cells if we needed more mitochondria.

Mitochondria Staining

Before isolation, the confluent cells were stained with 100 nM MitoTracker®Green FM and 40 nM TMRE for 1 hour. Subsequent isolation steps used solutions with 40 nM TMRE because TMRE is a potentiometric dye, which fluctuates in and out of the mitochondria depending on their inner membrane potential. 40 nM was determined as the optimal concentration for our experiments.

Mitochondria Isolation

Our complete isolation buffer contains 225mM mannitol, 75 mM sucrose, 0.5 mM EGTA, 20 mM HEPES, 0.5% (w/v) BSA, 1X protease inhibitor, pH 7.2 with 1 M KOH. All chemicals were purchased from Sigma Aldrich. The stock isolation buffer was prepared without BSA and the protease inhibitor and stored at 4°C. Mitochondria from the cultured cells were isolated using differential centrifugation. After collection, the cells were transferred to a glass homogenization tube in 3 mL of complete isolation buffer and homogenized with 30 strokes on ice for HeLa cells and 40 strokes for RS4;11. The cells were then transferred into 2-ml Eppendorf tubes and centrifuged at a low speed of 2000xg for 4min at 4°C. The resulting

supernatant was collected and centrifuged at a high speed of 12,000xg x 10min at 4°C. After this step, the supernatant as well as the light-colored fluffy sediment containing damaged mitochondria were aspirated and the resulting pellet was resuspended in KCl buffer (140 mM KCl, 2 mM MgCl2, 10mM NaCl, 0.5mM EGTA, 0.5mM KH2PO4, 2mM HEPES, 5 mM succinate, 2 μM rotenone, pH 7.2 adjusted with KOH). However, for mitochondria protein analysis, the mitochondria were resuspended in KCl buffer without EGTA. The protein analysis was done with BCA assay kit supplied by Thermo Fisher Scientific. A typical mitochondrial preparation with this protocol exhibits a respiratory control ratio of 3.1 (measured with a Hansatech Oxytherm), which is good for cultured cells[32].

Fluorescence measurement

Using an Olympus IX71 inverted microscope with two LED excitation sources (490nm & 565 nm), we observed the red and green fluorescence signals from MitoTracker® Green FM and TMRE. Our field of view from our 20X objective is 200 μm x 300 μm, and we monitored the fluorescence from this field of view by controlling the microscope with NIH Micromanager software, which also set the exposure time to one second.

To process and analyze the images, ImageJ software was used. For the entire field of view analysis, we measured the fluorescence intensity from the field of view. In contrast, for single mitochondrion analysis, we defined regions of interest enclosing the mitochondria and three more identical copies of that region of interest to define the background noise. We then assigned the fluorescence signal of the mitochondria as the measured signal subtracting the noise average.

Experimental design and electrical measurement

After mitochondria isolation, we loaded about 6 μg of mitochondrial protein of isolated mitochondria to a graphene device and incubated the device for 15 min at room temperature. Following two gentle washes with KCl buffer, the device was secured on the microscope stage, and the focus was adjusted. We then attached electrical contacts to the drain and source terminals of the devices using nickel (type) probes. The gate electrode was a Ag/AgCl electrode. An Agilent sourcemeter B2902A was used to apply the drain-source and gate voltages and to measure the currents. When both optical focus and electrical connection were satisfactory, we proceeded with taking MitoTracker® Green FM images and Ids versus Vg curve, and then started both the electrical measurement of Ids versus time and the fluorescence time-lapse measurement of TMRE signal. The electrical data sampling rate was 200 ms/point. In contrast, fluorescence images were taken once every 5 s for the experiments with CCCP or every 2 min for the experiments with BIM-BH3.

The starting volume of our chamber was 45 μL. During the experiment, we added 4.5 μL of the appropriate experimental substrate to achieve its final concentration. Extreme care was taken not to disturb the gate electrode. CCCP and cytc were obtained from Sigma Aldrich. BIM-BH3 peptide (sequence: MRPEIWIAQELRRIGDEFNA) was purchased from Synpeptide with a confirmation of >95% purity.

Control experiments were carried out in a similar manner with the only difference being the lack of isolated mitochondria. IGOR software was used to analyze all electrical data and the fluorescence data that were exported from ImageJ software.

Our KCl buffer contains 5 mM succinate as a carbon source for the mitochondria, facilitating the maintenance of $\Delta\Psi m$). Since the electrons derived from succinate doesn't go through complex I, we also added rotenone. Our choice of succinate and rotenone aimed to limit

ROS production by complex I [150]. We also intentionally left out ADP in our respiration buffer to avoid ATP synthase activation. In other words, we maximized $\Delta\Psi m$, maintaining a functional but not functioning ETC, and also limiting ROS production by complex I.

Additional Discussion

Immobilization of mitochondria on glass substrate

As shown in Figure 0.7**Error! Reference source not found.**c), a three-layer structure is sequentially grown on glass or quartz surface via (i) self-assembly of silane, (ii) ring addition reaction of epoxy group with primary amine, (iii) EDC/NHS chemistry for amide bond formation, and (iv) streptavidin-biotin interaction for binding biotinylated antibodies. The silane molecular is 3-glycidyloxypropyltrimethoxysilane (GOPS), which provides epoxy group terminated surface. The second hydrophilic layer is a commercial oligo (ethylene glycol) molecular with amino and carboxyl groups in the ends and the layer thickness can be precisely tuned by the number of ethylene glycol units.

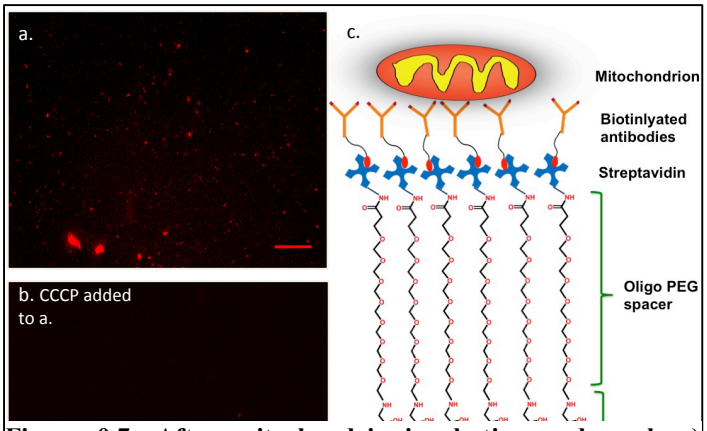

Figure 0.7: After mitochondria incubation and wash a) mitochondria stained with TMRE were immobilized on the functionalized glass surface; b) addition of 20 nM CCCP completely depolarized the mitochondrial membrane potential, indicated by loss of red fluorescence. Scale bar is 50 µm; c) overview of our surface chemistry

The key process in our bottom-up functionalization approach is to covalently tether streptavidin in aqueous solution and under a mild condition. The water-soluble carbodiimde (EDC) as a "zero-length" cross linker has been widely used to couple carboxyl groups to primary amines in bioconjugation methods. Introducing N-

hydroxysulfosuccinimide (NHS) into reaction will increase the stability of active intermediate and thus enhance the coupling efficiency. Therefore, a standard EDC/NHS two-step reaction is performed to immobilize streptavidin on spacer surface. 0.622 pM streptavidin, alexa fluor 488 conjugate was used to incubate the substrate for overnight at 4°C.The commercial rabbit anti-mouse-anti-TOM20 is biotinylated using the EZ-link NHS-LC-LC (succinimidyl-6-(biotinamido)-6-hexanamide hexanoate) kit purchased from Thermo Scientific, US. The biotinylated TOM20 antibody is allowed to react with the streptavidin before the deposition of isolated mitochondria. Mitochondria were isolated from Hela cells and stained with 100 nM TMRE as previously published in [70]. 100 μL of the mitochondria suspension was dropped onto the substrate. After incubation at room temperature, the substrate is washed with our respiration buffer. We can observe that mitochondria were retained on the substrate with functionalization vs. none on a bare glass slide subjected to the same mitochondrial incubation and wash. Our results are shown in

Compared with Kayo et al.'s method employing a gentle flow rate of 1-5 μl min^{-1}, our method uses manual pipetting for all steps, proving that our functionalization scheme is extremely stable and can withstand repeated harsh washing. Our functionalization is also extremely efficient because we only used 0.622 pM of streptavidin, alexa fluor conjugate, which is a three order of magnitude lower than in [151].

Analysis of genetically encoded mitochondrial pH sensors

A detailed estimate of the pH change measured using the graphene electrode with tethered mitochondria shows that our devices are much more sensitive than commercial pH meters. The intimate contact between the mitochondria and the graphene leads to dramatically

enhanced sensitivity of the graphene conductance to small changes in pH, even above and beyond the sensitivity in the "bulk pH change" calibration curve (Fig. 2c). Therefore, the sign of the conductance change indicates acidification or alkalization, but the magnitude of the conductance change (although not quantitatively calibrated) is a much more sensitive measurement of pH than existing commercial pH meters (see below).

Estimate of # of protons per mg of mitochondria taken up during CCCP induced depolarization:

Based on the commercial pH meter measurement, the measured pH change in the bulk suspension of mitochondria can be used to determine the # of protons taken up per mg of mitochondria upon introduction of CCCP.

We apply the Henderson-Hasselbalch equation and account for the movement of protons. In the case of CCCP where a net loss of protons to the mitochondrial inner membrane space, the equation is as follows:

$$pH = pKa + log\frac{[A^-]}{[HA]} \qquad (1)$$

$$\Delta pH = log\frac{n_{A^-} + n_{H^+}}{n_{HA} - n_{H^+}} - log\frac{n_{A^-}}{n_{HA}} \qquad (2)$$

$$A^-: weak\ acid$$

$$HA: conjugate\ base$$

$$n_{HA}: original\ moles\ of\ the\ weak\ acid\ and\ its\ conjgate\ base$$

$$n_{H^+}: moles\ of\ protons\ loss\ from\ the\ buffer$$

The KCl buffer contains 2 mM HEPES as the majority buffer with a pKa of 7.5. The original buffer pH is 7.2. In the bulk suspension experiments, 200 μg of mitochondrial protein in 2 mL volume induces a pH change from 7.21 to 7.23 after the addition of CCCP (as measured by

the commercial pH electrode). Hence, the number of protons transferred to the inner membrane space is 20.7 pmoles/0.1μg.

In the tethered mitochondria experiments, we used 0.1 μg of mitochondrial protein in a 50 μL volume. If we estimate the # of protons taken up based on the bulk measurements above, such a quantity of mitochondria would induce a pH change of ~$4x10^{-4}$ in the entire 50 μL solution volume, much too small to be measured by commercial pH electrodes. Such a change would also give rise to a small conductance change in the graphene if it occurred in the bulk solution volume (estimated to be 0.001% change from Fig. 4.2c). However, because of the intimate contact between the graphene and mitochondria, a much larger (few %) change in graphene conductance is measured, indicating the exquisite sensitivity of our devices to mitochondrial induced pH changes compared to existing techniques. A similar analysis in the case of BIM induced release of protons can be carried out, and yields similar conclusions.

Using our numbers, we can perform a calculation to check if fluorescent pH sensor can report similar changes we saw. Our previous calculation estimates 0.015-0.06 pmol protons would be extruded to the cytosol. Assuming 2 pL for the cytosol volume, this change equates to 7.5 mM to 30 mM protons. Given the buffering capacity of the cytosol is between 20 mM to 100 mM (meaning the amount requires to change pH by 1 unit), the pH decrease would be 0.375 to 1.5 in the cytosol. This range is well within the resolution of fluorescent pH probes.

CHAPTER 5: FUTURE IMPROVEMENTS

Overview

Overall, the three developments in the previous chapters improve on the core measurements on mitochondrial function. However, possible improvements exist for all three technologies to further their capabilities. First, for the single mitochondrial respiration assay, fluidic exchanges incorporation will allow modulating the mitochondrial respiration state. Along with lifetime measurement, the respiration assay will be robust and readily applicable in clinical settings. Then, a method to deterministic trapping of the mitochondria for the nano-channels will be implemented to allow precise immobilization of mitochondria for fluorescence detection with microplate readers. Finally, on the graphene platform, miniaturization to micrometer scale will be the first step to achieve single mitochondrial resolution.

REFERENCES

(1) Nicholls, D. G.; Ferguson, S. J. *Bioenergetics 3*; 3rd ed.; Academic Press, 2002.

(2) Chance, B.; Williams, G. R. Respiratory Enzymes in Oxidative Phosphorylation. *J Biol Chem* **1955**, *217*, 409–428.

(3) Frezza, C.; Cipolat, S.; Scorrano, L. Organelle Isolation: Functional Mitochondria from Mouse Liver, Muscle and Cultured Fibroblasts. *Nat. Protoc.* **2007**, *2*, 287–295.

(4) Clark, L. C.; Wolf, R.; Granger, D.; Taylor, Z. Continuous Recording of Blood Oxygen Tensions by Polarography. *J. Appl. Physiol.* **1953**, *6*, 189–193.

(5) Hutter, E.; Unterluggauer, H.; Garedew, A.; Jansen-Durr, P.; Gnaiger, E. High-Resolution Respirometry - A Modern Tool in Aging Research. *Exp. Gerontol.* **2006**, *41*, 457.

(6) Instruments, W. Warner Instruments - Mitocell Miniature Respirometer (MT-200, MT-200A) http://www.warneronline.com/product_info.cfm?id=386.

(7) Vollmer, A. P.; Probstein, R. F.; Gilbert, R.; Thorsen, T. Development of an Integrated Microfluidic Platform for Dynamic Oxygen Sensing and Delivery in a Flowing Medium. *Lab Chip* **2005**, *5*, 1059–1066.

(8) Wu, C.-C.; Luk, H.-N.; Lin, Y.-T. T.; Yuan, C.-Y. A Clark-Type Oxygen Chip for in Situ Estimation of the Respiratory Activity of Adhering Cells. *Talanta* **2010**, *81*, 228–234.

(9) Papkovsky, D. B. Methods in Optical Oxygen Sensing: Protocols and Critical Analyses. *Methods Enzymol.* **2004**, *381*, 715–735.

(10) Skolimowski, M.; Nielsen, M. W.; Emnéus, J.; Molin, S.; Taboryski, R.; Sternberg, C.; Dufva, M.; Geschke, O. Microfluidic Dissolved Oxygen Gradient Generator Biochip as a Useful Tool in Bacterial Biofilm Studies. *Lab Chip* **2010**, *10*, 2162–2169.

(11) Rumsey, W. L.; Vanderkooi, J. M.; Wilson, D. F. Imaging of Phosphorescence: A Novel Method for Measuring Oxygen Distribution in Perfused Tissue. *Science.* **1988**, *241*, 1649–1651.

(12) Dmitriev, R. I.; Papkovsky, D. B. Optical Probes and Techniques for O2 Measurement in Live Cells and Tissue. *Cell. Mol. Life Sci.* **2012**, *69*, 2025–2039.

(13) Wu, C.; Bull, B.; Christensen, K.; McNeill, J. Ratiometric Single-Nanoparticle Oxygen Sensors for Biological Imaging. *Angew. Chem. Int. Ed. Engl.* **2009**, *48*, 2741–2745.

(14) Gao, X. P. A.; Zheng, G.; Lieber, C. M. Subthreshold Regime Has the Optimal Sensitivity for Nanowire FET Biosensors. *Nano Lett.* **2010**, *10*, 547–552.

(15) Ferrer-Anglada, N.; Kaempgen, M.; Roth, S. Transparent and Flexible Carbon Nanotube/polypyrrole and Carbon Nanotube/polyaniline pH Sensors. *Phys. Status Solidi Basic Res.* **2006**, *243*, 3519–3523.

(16) Mailly-Giacchetti, B.; Hsu, A.; Wang, H.; Vinciguerra, V.; Pappalardo, F.; Occhipinti, L.; Guidetti, E.; Coffa, S.; Kong, J.; Palacios, T. pH Sensing Properties of Graphene Solution-Gated Field-Effect Transistors. *J. Appl. Phys.* **2013**, *114*, 84505.

(17) Rajan, N. K.; Routenberg, D. a; Reed, M. a. Optimal Signal-to-Noise Ratio for Silicon Nanowire Biochemical Sensors. *Appl. Phys. Lett.* **2011**, *98*, 264107–2641073.

(18) Gao, X. P. A.; Zheng, G.; Lieber, C. M. Subthreshold Regime Has the Optimal Sensitivity for Nanowire FET Biosensors. *Nano Lett.* **2010**, *10*, 547–552.

(19) Wallace, D. C.; Fan, W.; Procaccio, V. Mitochondrial Energetics and Therapeutics. *Annu. Rev. Pathol.* **2010**, *5*, 297–348.

(20) Wallace, D. C. Bioenergetic Origins of Complexity and Disease. *Cold Spring Harb. Symp. Quant. Biol.* **2011**, *76*, 1–16.

(21) Nicholls, D.; Ferguson, S. *Bioenergetics*; 4th ed.; 2013.

(22) Chipuk, J. E.; Moldoveanu, T.; Llambi, F.; Parsons, M. J.; Green, D. R. The BCL-2 Family Reunion. *Mol. Cell* **2010**, *37*, 299–310.

(23) Wallace, D. C. Mitochondria and Cancer. *Nat. Rev. Cancer* **2012**, *12*, 685–698.

(24) Rogers, G. W.; Brand, M. D.; Petrosyan, S.; Ashok, D.; Elorza, A. A.; Ferrick, D. a; Murphy, A. N. High Throughput Microplate Respiratory Measurements Using Minimal Quantities of Isolated Mitochondria. *PLoS One* **2011**, *6*, e21746.

(25) Sharpley, M. S.; Marciniak, C.; Eckel-Mahan, K.; McManus, M.; Crimi, M.; Waymire, K.; Lin, C. S.; Masubuchi, S.; Friend, N.; Koike, M.; *et al.* Heteroplasmy of Mouse mtDNA Is Genetically Unstable and Results in Altered Behavior and Cognition. *Cell* **2012**, *151*, 333–343.

(26) Fan, W.; Waymire, K. G.; Narula, N.; Li, P.; Rocher, C.; Coskun, P. E.; Vannan, M. a; Narula, J.; Macgregor, G. R.; Wallace, D. C. A Mouse Model of Mitochondrial Disease Reveals Germline Selection against Severe mtDNA Mutations. *Science (80-.).* **2008**, *319*, 958–962.

(27) Li, M.; Schönberg, A.; Schaefer, M.; Schroeder, R.; Nasidze, I.; Stoneking, M. Detecting Heteroplasmy from High-Throughput Sequencing of Complete Human Mitochondrial DNA Genomes. *Am. J. Hum. Genet.* **2010**, *87*, 237–249.

(28) Payne, B. A. I.; Wilson, I. J.; Yu-wai-Man, P.; Coxhead, J.; Deehan, D.; Horvath, R.; Taylor, R. W.; Samuels, D. C.; Santibanez-koref, M.; Chinnery, P. F. Universal Heteroplasmy of Human Mitochondrial DNA. *Hum. Mol. Genet.* **2013**, *22*, 384–390.

(29) Wu, R.; Galan-Acosta, L.; Norberg, E. Glucose Metabolism Provide Distinct Prosurvival Benefits to Non-Small Cell Lung Carcinomas. *Biochem. Biophys. Res. Commun.* **2015**, *460*, 572–577.

(30) Smiley, S. T.; Reers, M.; Mottola-Hartshorn, C.; Lin, M.; Chen, A.; Smith, T. W.; Steele, G. D.; Chen, L. B. Intracellular Heterogeneity in Mitochondrial Membrane Potentials Revealed by a J-Aggregate-Forming Lipophilic Cation JC-1. *Proc. Natl. Acad. Sci. U. S. A.* **1991**, *88*, 3671–3675.

(31) Nagrath, S.; Sequist, L. V; Maheswaran, S.; Bell, D. W.; Ryan, P.; Balis, U. J.; Tompkins, R. G.; Haber, D. A. Isolation of Rare Circulating Tumour Cells in Cancer Patients by Microchip Technology. *Nature* **2011**, *450*, 1235–1239.

(32) Frezza, C.; Cipolat, S.; Scorrano, L. Organelle Isolation: Functional Mitochondria from Mouse Liver, Muscle and Cultured Fibroblasts. *Nat. Protoc.* **2007**, *2*, 287–295.

(33) Deegan, R. D.; Bakajin, O.; Dupont, T. F.; Huber, G.; Nagel, S. R.; Witten, T. A. Capillary Flow as the Cause of Ring Stains from Dried Liquid Drops. *Nature* **1997**, *389*,

827–829.

(34) Quaranta, M.; Borisov, S. M.; Klimant, I. Indicators for Optical Oxygen Sensors. *Bioanal. Rev.* **2012**, *4*, 115–157.

(35) Dmitriev, R. I.; Papkovsky, D. B. Intracellular Probes for Imaging Oxygen Concentration: How Good Are They? *Methods Appl. Fluoresc.* **2015**, *3*, 34001.

(36) van Dam, M. Solvent-Resistant Elastomeric Microfluidic Devices and Applications, California Institute of Technology, 2006.

(37) Celina, M.; Gillen, K. T. Oxygen Permeability Measurements on Elastomers at Temperatures up to 225 °C. *Macromolecules* **2005**, *38*, 2754–2763.

(38) Peacock, R. N. Practical Selection of Elastomer Materials for Vacuum Seals. *J. Vac. Sci. Technol.* **1980**, *17*, 330.

(39) *Comprehensive Membrane Science and Engineering*; Drioli, E.; Giorno, G., Eds.; 1st ed.; Elsevier, 2010.

(40) Molter, T. W.; McQuaide, S. C.; Suchorolski, M. T.; Strovas, T. J.; Burgess, L. W.; Meldrum, D. R.; Lidstrom, M. E. A Microwell Array Device Capable of Measuring Single-Cell Oxygen Consumption Rates. *Sensors Actuators B* **2009**, *135*, 678–686.

(41) Grad, L. I.; Sayles, L. C.; Lemire, B. D. Introduction of an Additional Pathway for Lactate Oxidation in the Treatment of Lactic Acidosis and Mitochondrial Dysfunction in Caenorhabditis Elegans. *Proc. Natl. Acad. Sci. U. S. A.* **2005**, *102*, 18367–18372.

(42) Hansatech Instruments. Oxygen Electrode & Chlorophyll Fluorescence Measurement Systems http://www.hansatech-instruments.com/oxyg1.htm.

(43) Wu, R.; Galan-Acosta, L.; Norberg, E. Glucose Metabolism Provide Distinct Prosurvival Benefits to Non-Small Cell Lung Carcinomas. *Biochem. Biophys. Res. Commun.* **2015**, *460*, 572–577.

(44) O'Riordan, T. C.; Buckley, D.; Ogurtsov, V.; O'Connor, R.; Papkovsky, D. B. A Cell Viability Assay Based on Monitoring Respiration by Optical Oxygen Sensing. *Anal. Biochem.* **2000**, *278*, 221–227.

(45) Will, Y.; Hynes, J.; Ogurtsov, V. I.; Papkovsky, D. B. Analysis of Mitochondrial Function Using Phosphorescent Oxygen-Sensitive Probes. *Nat. Protoc.* **2006**, *1*, 2563–2572.

(46) Nock, V.; Blaikie, R. J.; David, T. Patterning, Integration and Characterisation of Polymer Optical Oxygen Sensors for Microfluidic Devices. *Lab Chip* **2008**, *8*, 1300–1307.

(47) Nock, V.; Alkaisi, M.; Blaikie, R. J. Photolithographic Patterning of Polymer-Encapsulated Optical Oxygen Sensors. *Microelectron. Eng.* **2010**, *87*, 814–816.

(48) Molter, T. W.; McQuaide, S. C.; Holl, M. R.; Meldrum, D. R.; Dragavon, J. M.; Anderson, J. B.; Young, C. A.; Burgess, L. W.; Lidstrom, M. E. A New Approach for Measuring Single-Cell Oxygen Consumption Rates. *IEEE Trans. Autom. Sci. Eng.* **2008**, *5*, 32–42.

(49) Grist, S.; Schmok, J.; Liu, M.-C.; Chrostowski, L.; Cheung, K. Designing a Microfluidic Device with Integrated Ratiometric Oxygen Sensors for the Long-Term Control and Monitoring of Chronic and Cyclic Hypoxia. *Sensors* **2015**, *15*, 20030–20052.

(50) Dragavon, J.; Molter, T.; Young, C.; Strovas, T.; McQuaide, S.; Holl, M.; Zhang, M.; Cookson, B.; Jen, a.; Lidstrom, M.; *et al.* A Cellular Isolation System for Real-Time Single-Cell Oxygen Consumption Monitoring. *J. R. Soc. Interface* **2008**, *5*, S151–S159.

(51) Gear, A. R.; Bednarek, J. M. Direct Counting and Sizing of Mitochondria in Solution. *J. Cell Biol.* **1972**, *54*, 325–345.

(52) Dmitriev, R. I.; Kondrashina, A. V.; Koren, K.; Klimant, I.; Zhdanov, A. V.; Pakan, J. M. P.; McDermott, K. W.; Papkovsky, D. B. Small Molecule Phosphorescent Probes for O2 Imaging in 3D Tissue Models. *Biomater. Sci.* **2014**, *2*, 853.

(53) Liu, H.; Yang, H.; Hao, X.; Xu, H.; Lv, Y.; Xiao, D.; Wang, H.; Tian, Z. Development of Polymeric Nanoprobes with Improved Lifetime Dynamic Range and Stability for Intracellular Oxygen Sensing. *Small* **2013**, *9*, 2639–2648.

(54) Kurokawa, H.; Ito, H.; Inoue, M.; Tabata, K.; Sato, Y.; Yamagata, K.; Kizaka-Kondoh, S.; Kadonosono, T.; Yano, S.; Inoue, M.; *et al.* High Resolution Imaging of Intracellular Oxygen Concentration by Phosphorescence Lifetime. *Sci. Rep.* **2015**, *5*, 10657.

(55) Dmitriev, R. I.; Papkovsky, D. B. Intracellular Probes for Imaging Oxygen Concentration: How Good Are They? *Methods Appl. Fluoresc.* **2015**, *3*, 34001.

(56) Collins, T. J.; Berridge, M. J.; Lipp, P.; Bootman, M. D. Mitochondria Are Morphologically and Functionally Heterogeneous within Cells. *Eur. Mol. Biol. Organ. J.* **2002**, *21*, 1616–1627.

(57) Picard, M.; White, K.; Turnbull, D. M. Mitochondrial Morphology, Topology, and Membrane Interactions in Skeletal Muscle: A Quantitative Three-Dimensional Electron Microscopy Study. *J. Appl. Physiol. (Bethesda, Md 1985)* **2013**, *114*, 161–171.

(58) Huser, J.; Blatter, L. A. Fluctuations in Mitochondrial Membrane Potential Caused by Repetitive Gating of the Permeability Transition Pore. *Biochem. J.* **1999**, *343*, 311–317.

(59) Lascaratos, G.; Ji, D.; Wood, J. P. M.; Osborne, N. N. Visible Light Affects Mitochondrial Function and Induces Neuronal Death in Retinal Cell Cultures. *Vision Res.* **2007**, *47*, 1191–1201.

(60) Ma, Q.; Fang, H.; Shang, W.; Liu, L.; Xu, Z.; Ye, T.; Wang, X.; Zheng, M.; Chen, Q.; Cheng, H. Superoxide Flashes: Early Mitochondrial Signals for Oxidative Stress-Induced Apoptosis. *J. Biol. Chem.* **2011**, *286*, 27573–27581.

(61) Wallace, D. C. A Mitochondrial Paradigm of Metabolic and Degenerative Diseases, Aging, and Cancer: A Dawn for Evolutionary Medicine. *Annu. Rev. Genet.* **2005**, *39*, 359–407.

(62) Wallace, D. C.; Lott, M. T.; Procaccio, V. Mitochondrial Genes in Degenerative Diseases, Cancer and Aging. In *Emery and Rimoin's Principles and Practice of Medical Genetics*; Rimoin, D. L.; Connor, J. M.; Pyeritz, R. E.; Korf, B. R., Eds.; Churchill Livingstone Elsevier: Philadelphia, PA, 2007; Vol. Volume 1, pp. 194–298.

(63) Bandy, B.; Davison, A. J. Mitochondrial Mutations May Increase Oxidative Stress: Implications for Carcinogenesis and Aging? *Free Radic. Biol. Med.* **1990**, *8*, 523–539.

(64) Harman, D. The Biologic Block: The Mitochondria? *J. Am. Geriatr. Soc.* **1972**, *20*, 145–147.

(65) Wallace, D. C.; Singh, G.; Lott, M. T.; Hodge, J. A.; Schurr, T. G.; Lezza, A. M.; Elsas, L. J.; Nikoskelainen, E. K. Mitochondrial DNA Mutation Associated with Leber's Hereditary Optic Neuropathy. *Science (80-.).* **1988**, *242*, 1427–1430.

(66) Schaefer, A. M.; Taylor, R. W.; Turnbull, D. M.; Chinnery, P. F. The Epidemiology of Mitochondrial Disorders--Past, Present and Future. *Biochim. Biophys. Acta* **2004**, *1659*, 115–120.

(67) Elliott, H. R.; Samuels, D. C.; Eden, J. A.; Relton, C. L.; Chinnery, P. F. Pathogenic Mitochondrial DNA Mutations Are Common in the General Population. *Am. J. Hum. Genet.* **2008**, *83*, 254–260.

(68) Vives-Bauza, C.; Przedborski, S. Mitophagy: The Latest Problem for Parkinson's Disease. *Trends Mol. Med.* **2011**, *17*, 158–165.

(69) Gilkerson, R. W.; De Vries, R. L. a; Lebot, P.; Wikstrom, J. D.; Torgyekes, E.; Shirihai, O. S.; Przedborski, S.; Schon, E. a. Mitochondrial Autophagy in Cells with mtDNA Mutations Results from Synergistic Loss of Transmembrane Potential and mTORC1 Inhibition. *Hum. Mol. Genet.* **2012**, *21*, 978–990.

(70) Zand, K.; Pham, T.; Davila, A.; Wallace, D. C.; Burke, P. J. Nanofluidic Platform for Single Mitochondria Analysis Using Fluorescence Microscopy. *Anal. Chem.* **2013**, *85*, 6018–6025.

(71) Zhang, J.; Nuebel, E.; Wisidagama, D. R. R.; Setoguchi, K.; Hong, J. S.; Van Horn, C. M.; Imam, S. S.; Vergnes, L.; Malone, C. S.; Koehler, C. M.; *et al.* Measuring Energy Metabolism in Cultured Cells, Including Human Pluripotent Stem Cells and Differentiated Cells. *Nat. Protoc.* **2012**, *7*, 1068–1085.

(72) Brand, M. D.; Nicholls, D. G. Assessing Mitochondrial Dysfunction in Cells. *Biochem. J.* **2011**, *435*, 297–312.

(73) Lim, T.-S.; Davila, A.; Zand, K.; Wallace, D. C.; Burke, P. J. Wafer-Scale Mitochondrial Membrane Potential Assays. *Lab Chip* **2012**, *12*, 2719–2725.

(74) Gerencser, A. A.; Chinopoulos, C.; Birket, M. J.; Jastroch, M.; Vitelli, C.; Nicholls, D. G.; Brand, M. D. Quantitative Measurement of Mitochondrial Membrane Potential in Cultured Cells: Calcium-Induced de- and Hyperpolarization of Neuronal Mitochondria. *J. Physiol.* **2012**, *590*, 2845–2871.

(75) Klima, J. *Cytologie Eine Einf. F. Studierende D. Naturwiss. U. Medizin*; Stuttgart G. Fischer , 1967.

(76) Qin, D.; Xia, Y.; Whitesides, G. M. Soft Lithography for Micro- and Nanoscale Patterning. *Nat. Protoc.* **2010**, *5*, 491–502.

(77) Liang, X. G.; Chou, S. Y. Nanogap Detector inside Nanofluidic Channel for Fast Real-Time Label-Free DNA Analysis. *Nano Lett.* **2008**, *8*, 1472–1476.

(78) Xia, D.; Yan, J.; Hou, S. Fabrication of Nanofluidic Biochips with Nanochannels for Applications in DNA Analysis. *Small* **2012**, *8*, 1–15.

(79) Duffy, D. C.; McDonald, J. C.; Schueller, O. J.; Whitesides, G. M. Rapid Prototyping of Microfluidic Systems in Poly(dimethylsiloxane). *Anal. Chem.* **1998**, *70*, 4974–4984.

(80) Vergun, O.; Votyakova, T. V; Reynolds, I. J. Spontaneous Changes in Mitochondrial

Membrane Potential in Single Isolated Brain Mitochondria. *Biophys. J.* **2003**, *85*, 3358–3366.

(81) Hattori, T.; Watanabe, K.; Uechi, Y.; Yoshioka, H.; Ohta, Y. Repetitive Transient Depolarizations of the Inner Mitochondrial Membrane Induced by Proton Pumping. *Biophys. J.* **2005**, *88*, 2340–2349.

(82) Cossarizza, A.; Ceccarelli, D.; Masini, A. Functional Heterogeneity of an Isolated Mitochondrial Population Revealed by Cytofluorometric Analysis at the Single Organelle Level. *Exp. Cell Res.* **1996**, *222*, 84–94.

(83) Lecoeur, H.; Chauvier, D.; Langonné, A.; Rebouillat, D.; Brugg, B.; Mariani, J.; Edelman, L.; Jacotot, E. Dynamic Analysis of Apoptosis in Primary Cortical Neurons by Fixed- and Real-Time Cytofluorometry. *Apoptosis* **2004**, *9*, 157–169.

(84) McGill, A.; Frank, A.; Emmett, N.; Turnbull, D. M.; Birch-Machin, M. a; Reynolds, N. J. The Anti-Psoriatic Drug Anthralin Accumulates in Keratinocyte Mitochondria, Dissipates Mitochondrial Membrane Potential, and Induces Apoptosis through a Pathway Dependent on Respiratory Competent Mitochondria. *FASEB J.* **2005**, *19*, 1012–1014.

(85) Duchen, M. R.; Leyssens, A.; Crompton, M. Transient Mitochondrial Depolarizations Reflect Focal Sarcoplasmic Reticular Calcium Release in Single Rat Cardiomyocytes. *J. Cell Biol.* **1998**, *142*, 975–988.

(86) Kurz, F. T.; Aon, M. a; O'Rourke, B.; Armoundas, A. a. Spatio-Temporal Oscillations of Individual Mitochondria in Cardiac Myocytes Reveal Modulation of Synchronized Mitochondrial Clusters. *Proc. Natl. Acad. Sci. U. S. A.* **2010**, *107*, 14315–14320.

(87) Nicholls, D. G. Fluorescence Measurement of Mitochondrial Membrane Potential Changes in Cultured Cells. *Methods* **2012**, *810*, 119–133.

(88) Buckman, J. F.; Reynolds, I. J. Spontaneous Changes in Mitochondrial Membrane Potential in Cultured Neurons. *J. Neurosci.* **2001**, *21*, 5054–5065.

(89) Halestrap, A. The Regulation of the Matrix Volume of Mammalian Mitochondria in Vivo and in Vitro and Its Role in the Control of Mitochondrial Metabolism. *Biochim. Biophys. Acta* **1989**, *973*, 355–382.

(90) Trounce, I. A.; Kim, Y. L.; Jun, A. S.; Wallace, D. C. Assessment of Mitochondrial Oxidative Phosphorylation in Patient Muscle Biopsies, Lymphoblasts, and Transmitochondrial Cell Lines. *Methods Enzymol.* **1996**, *42*, 484–508.

(91) Huser, J.; Rechenmacher, C. E.; Blatter, L. A. Imaging the Permeability Pore Transition in Single Mitochondria. *Biophys. J.* **1998**, *74*, 2129–2137.

(92) Uechi, Y.; Yoshioka, H.; Morikawa, D.; Ohta, Y. Stability of Membrane Potential in Heart Mitochondria: Single Mitochondrion Imaging. *Biochem. Biophys. Res. Commun.* **2006**, *344*, 1094–1101.

(93) Higuchi, Y.; Miura, T.; Kajimoto, T.; Ohta, Y. Effects of Disialoganglioside GD3 on the Mitochondrial Membrane Potential. *FEBS Lett.* **2005**, *579*, 3009–3013.

(94) Medina, J. M.; López-Mediavilla, C.; Orfao, A. Flow Cytometry of Isolated Mitochondria during Development and under Some Pathological Conditions. *FEBS Lett.* **2002**, *510*, 127–132.

(95) Lecoeur, H. H.; LangonnÈ, A.; Baux, L.; Rebouillat, D.; Rustin, P.; PrÈvost, M.-C.; Brenner, C.; Edelman, L. Lè. L.; Jacotot, E.; Langonne, A.; *et al.* Real-Time Flow Cytometry Analysis of Permeability Transition in Isolated Mitochondria. *Exp. Cell Res.* **2004**, *294*, 106–117.

(96) Strack, A.; Duffy, C. F.; Malvey, M.; Arriaga, E. A. Individual Mitochondrion Characterization: A Comparison of Classical Assays to Capillary Electrophoresis with Laser-Induced Fluorescence Detection. *Anal. Biochem.* **2001**, *294*, 141–147.

(97) Fuller, K. M.; Arriaga, E. A.; Ã, E. A. A. Advances in the Analysis of Single Mitochondria. *Curr. Opin. Biotechnol.* **2003**, *14*, 35–41.

(98) Duffy, C. F.; MacCraith, B.; Diamond, D.; O'Kennedy, R.; Arriaga, E. A. Fast Electrophoretic Analysis of Individual Mitochondria Using Microchip Capillary Electrophoresis with Laser Induced Fluorescence Detection. *Lab Chip* **2006**, *6*, 1007–1011.

(99) Johnson, R. D.; Navratil, M.; Poe, B. G.; Xiong, G.; Olson, K. J.; Ahmadzadeh, H.; Andreyev, D.; Duffy, C. F.; Arriaga, E. A. Analysis of Mitochondria Isolated from Single Cells. *Anal. Bioanal. Chem.* **2007**, *387*, 107–118.

(100) Kostal, V.; Arriaga, E. A. Recent Advances in the Analysis of Biological Particles by Capillary Electrophoresis. *Electrophoresis* **2008**, *29*, 2578–2586.

(101) Kostal, V.; Katzenmeyer, J.; Arriaga, E. A. Capillary Electrophoresis in Bioanalysis. *Anal. Chem.* **2008**, *80*, 4533–4550.

(102) Sarosiek, K. A.; Chonghaile, T. N.; Letai, A. Mitochondria: Gatekeepers of Response to Chemotherapy. *Trends Cell Biol.* **2013**, *23*, 612–619.

(103) Rustin, P.; Kroemer, G. Mitochondria and Cancer. *Ernst Shering Found. Symp. Proc.* **2008**, *4*, 1–21.

(104) Peixoto, P. M.; Teijido, O.; Mirzalieva, O.; Dejean, L. M.; Pavlov, E. V.; Antonsson, B.; Kinnally, K. W. MAC Inhibitors Antagonize the pro-Apoptotic Effects of tBid and Disassemble Bax / Bak Oligomers. *J. Bioenerg. Biomembr.* **2015**.

(105) Letai, A.; Bassik, M. C.; Walensky, L. D.; Sorcinelli, M. D.; Weiler, S.; Korsmeyer, S. J. Distinct BH3 Domains Either Sensitize or Activate Mitochondrial Apoptosis, Serving as Prototype Cancer Therapeutics. *Cancer Cell* **2002**, *2*, 183–192.

(106) Kluck, R. M.; Bossy-Wetzel, E.; Green, D. R.; Newmeyer, D. D. The Release of Cytochrome c from Mitochondria: A Primary Site for Bcl-2 Regulation of Apoptosis. *Science.* **1997**, *275*, 1132.

(107) Kroemer, G.; Galluzzi, L.; Brenner, C. Mitochondrial Membrane Permeabilization in Cell Death. *Physiol. Rev.* **2007**, *87*, 99–163.

(108) Jiang, X.; Jiang, H.; Shen, Z.; Wang, X. Activation of Mitochondrial Protease OMA1 by Bax and Bak Promotes Cytochrome c Release during Apoptosis. *Proc. Natl. Acad. Sci. U. S. A.* **2014**, *111*, 14782–14787.

(109) Frezza, C.; Cipolat, S.; Martins de Brito, O.; Micaroni, M.; Beznoussenko, G. V; Rudka, T.; Bartoli, D.; Polishuck, R. S.; Danial, N. N.; De Strooper, B.; *et al.* OPA1 Controls Apoptotic Cristae Remodeling Independently from Mitochondrial Fusion. *Cell* **2006**, *126*,

177–189.

(110) Head, B.; Griparic, L.; Amiri, M.; Gandre-Babbe, S.; van der Bliek, A. M. Inducible Proteolytic Inactivation of OPA1 Mediated by the OMA1 Protease in Mammalian Cells. *J. Cell Biol.* **2009**, *187*, 959–966.

(111) Gottlieb, R. A.; Nordberg, J.; Skowronski, E.; Babior, B. M. Apoptosis Induced in Jurkat Cells by Several Agents Is Preceded by Intracellular Acidification. *Proc. Natl. Acad. Sci. U. S. A.* **1996**, *93*, 654–658.

(112) Khaled, A. R.; Kim, K.; Hofmeister, R.; Muegge, K.; Durum, S. K. Withdrawal of IL-7 Induces Bax Translocation from Cytosol to Mitochondria through a Rise in Intracellular pH. *Proc. Natl. Acad. Sci. U. S. A.* **1999**, *96*, 14476–14481.

(113) Matsuyama, S.; Llopis, J.; Deveraux, Q. L.; Tsien, R. Y.; Reed, J. C. Changes in Intramitochondrial and Cytosolic pH: Early Events That Modulate Caspase Activation during Apoptosis. *Nat. Cell Biol.* **2000**, *2*, 318–325.

(114) Ryan, J.; Letai, A. BH3 Profiling in Whole Cells by Fluorimeter or FACS. *Methods* **2013**, *61*, 156–164.

(115) Wang, Y. Y.; Burke, P. J. A Large-Area and Contamination-Free Graphene Transistor for Liquid-Gated Sensing Applications. *Appl. Phys. Lett.* **2013**, *103*, 52103.

(116) Kayo, S.; Bahnemann, J.; Klauser, M.; Pörtner, R.; Zeng, A.-P. A Microfluidic Device for Immuno-Affinity-Based Separation of Mitochondria from Cell Culture. *Lab Chip* **2013**, *13*, 4467–4475.

(117) Ryan, J.; Brunelle, J. K.; Letai, A. Heightened Mitochondrial Priming Is the Basis for Apoptotic Hypersensitivity of CD4+ CD8+ Thymocytes. *Proc. Natl. Acad. Sci.* **2010**, *107*, 12895–12900.

(118) Lim, T.-S.; Davila, A.; Wallace, D. C.; Burke, P. J. Assessment of Mitochondrial Membrane Potential Using an on-Chip Microelectrode in a Microfluidic Device. *Lab Chip* **2010**, *10*, 1683–1688.

(119) Ohno, Y.; Maehashi, K.; Yamashiro, Y.; Matsumoto, K. Electrolyte-Gated Graphene Field-Effect Transistors for Detecting pH and Protein Adsorption. *Nano Lett.* **2009**, *9*, 3318–3322.

(120) Wang, Y. Y.; Burke, P. J. Polyelectrolyte Multilayer Electrostatic Gating of Graphene Field-Effect Transistors. *Nano Res.* **2014**, *7*, 1650–1658.

(121) Scaduto, R. C.; Grotyohann, L. W. Measurement of Mitochondrial Membrane Potential Using Fluorescent Rhodamine Derivatives. *Biophys. J.* **1999**, *76*, 469–477.

(122) Collins, T. J.; Berridge, M. J.; Lipp, P.; Bootman, M. D. Mitochondria Are Morphologically and Functionally Heterogeneous within Cells. *EMBO J.* **2002**, *21*, 1616–1627.

(123) Ren, D.; Tu, H.-C.; Kim, H.; Wang, G. X.; Bean, G. R.; Takeuchi, O.; Jeffers, J. R.; Zambetti, G. P.; Hsieh, J. J.-D.; Cheng, E. H.-Y. BID, BIM, and PUMA Are Essential for Activation of the BAX- and BAK-Dependent Cell Death Program. *Science* **2010**, *330*, 1390–1393.

(124) Frank, D. O.; Dengjel, J.; Wilfling, F.; Kozjak-Pavlovic, V.; Häcker, G.; Weber, A. The

pro-Apoptotic BH3-Only Protein Bim Interacts with Components of the Translocase of the Outer Mitochondrial Membrane (TOM). *PLoS One* **2015**, *10*, e0123341.

(125) Del, V.; Moore, G.; Schlis, K. D.; Sallan, S. E.; Armstrong, S. A.; Letai, A. BCL-2 Dependence and ABT-737 Sensitivity in Acute Lymphoblastic Leukemia BCL-2 Dependence and ABT-737 Sensitivity in Acute Lymphoblastic Leukemia. *Leukemia* **2008**, *111*, 2300–2309.

(126) Ow, Y. P.; Green, D. R.; Hao, Z.; Mak, T. W. Cytochrome c: Functions beyond Respiration. *Nat. Rev. Mol. Cell Biol.* **2008**, *9*, 532–542.

(127) Mootha, V. K.; Wei, M. C.; Buttle, K. F.; Scorrano, L.; Panoutsakopoulou, V.; Mannella, C. A.; Korsmeyer, S. J. A Reversible Component of Mitochondrial Respiratory Dysfunction in Apoptosis Can Be Rescued by Exogenous Cytochrome c. *EMBO J.* **2001**, *20*, 661–671.

(128) Waterhouse, N. J.; Goldstein, J. C.; Von Ahsen, O.; Schuler, M.; Newmeyer, D. D.; Green, D. R. Cytochrome c Maintains Mitochondrial Transmembrane Potential and ATP Generation after Outer Mitochondrial Membrane Permeabilization during the Apoptotic Process. *J. Cell Biol.* **2001**, *153*, 319–328.

(129) Giordano, A.; Calvani, M.; Petillo, O.; Grippo, P.; Tuccillo, F.; Melone, M. A. B.; Bonelli, P.; Calarco, A.; Peluso, G. tBid Induces Alterations of Mitochondrial Fatty Acid Oxidation Flux by Malonyl-CoA-Independent Inhibition of Carnitine Palmitoyltransferase-1. *Cell Death Differ.* **2005**, *12*, 603–613.

(130) Cortese, J. D.; Voglino, A. L.; Hackenbrock, C. R. The Ionic Strength of the Intermembrane Space of Intact Mitochondria Is Not Affected by the pH or Volume of the Intermembrane Space. *Biochim. Biophys. Acta* **1992**, *1100*, 189–197.

(131) Porcelli, A. M.; Ghelli, A.; Zanna, C.; Pinton, P.; Rizzuto, R.; Rugolo, M. pH Difference across the Outer Mitochondrial Membrane Measured with a Green Fluorescent Protein Mutant. *Biochem. Biophys. Res. Commun.* **2005**, *326*, 799–804.

(132) Heytler, P. G. Uncoupling of Oxidative Phosphorylation on Carbonyl Cyanide Phenlhydrazones. *Biochemistry* **1963**, *2*, 357–361.

(133) Kasianowicz, J.; Benz, R.; McLaughlin, S. The Kinetic Mechanism by Which CCCP (Carbonyl Cyanide M-Chlorophenylhydrazone) Transports Protons across Membranes. *J. Membr. Biol.* **1984**, *82*, 179–190.

(134) Hirose, S.; Yaginuma, N.; Inada, Y. Disruption of Charge Separation Followed by that of the Proton Gradient in the Mitochondrial Membrane by CCCP. *J. Biochem.* **1974**, *76*, 213–216.

(135) McCommis, K. S.; Baines, C. P. The Role of VDAC in Cell Death: Friend or Foe? *Biochim. Biophys. Acta* **2012**, *1818*, 1444–1450.

(136) Mitchell, P. Coupling of Phosphorylation to Electron and Hydrogen Transfer by a Chemi-Osmotic Type of Mechanism. *Nature* **1961**, *191*, 144–148.

(137) Kim, T.-H.; Zhao, Y.; Wen-Xing Ding, J. N. S.; Xi He, Y.-W. S.; Chen, J.; Hannah Rabinowich, Andrew A. Amoscato, and X.-M. Y. Bid–cardiolipin Interaction at Mitochondrial Contact Site Contributes to Mitochondrial Cristae Reorganization and Cytochrome c Release. *Mol. Biol. Cell* **2004**, *15*, 3061–3072.

(138) Perotti, E.; Anderson, Wi.; Swift, H. Quantitative Cytochemistry of the Diaminobenzidine Cytochrome Oxidase Reaction Product in Mitochondria of Cardiac Muscle and Pancreas. *J. Histochem. Cytochem.* **1985**, *31*, 351–365.

(139) Scorrano, L.; Ashiya, M.; Buttle, K.; Weiler, S.; Oakes, S. a.; Mannella, C. a.; Korsmeyer, S. J. A Distinct Pathway Remodels Mitochondrial Cristae and Mobilizes Cytochrome c during Apoptosis. *Dev. Cell* **2002**, *2*, 55–67.

(140) Renault, T. T.; Floros, K. V; Chipuk, J. E. BAK/BAX Activation and Cytochrome c Release Assays Using Isolated Mitochondria. *Methods* **2013**, *61*, 146–155.

(141) Park, H. J.; Lyons, J. C.; Ohtsubo, T.; Song, C. W. Acidic Environment Causes Apoptosis by Increasing Caspase Activity. *Br. J. Cancer* **1999**, *80*, 1892–1897.

(142) Nicholls, D. G.; Bernardi, P.; Brand, M. D.; Halestrap, A.; Lemasters, J. J.; Reynolds, I. J. Apoptosis and the Laws of Thermodynamics. *Nat. Cell Biol.* **2000**, *2*, E172.

(143) Perkins, G. A.; Ellisman, M. H. Remodeling of Mitochondria in Apoptosis. In *Mitochondria and Cell Death*; Hockenbery, D., Ed.; Humana Press, 2016; pp. 85–110.

(144) Santo-Domingo, J.; Demaurex, N. The Renaissance of Mitochondrial pH. *J. Gen. Physiol.* **2012**, *139*, 391–393.

(145) Poburko, D.; Santo-domingo, J.; Demaurex, N. Dynamic Regulation of the Mitochondrial Proton Gradient during Cytosolic Calcium Elevations * □. **2011**, *286*, 11672–11684.

(146) Santo-Domingo, J.; Giacomello, M.; Poburko, D.; Scorrano, L.; Demaurex, N. OPA1 Promotes pH Flashes That Spread between Contiguous Mitochondria without Matrix Protein Exchange. *EMBO J.* **2013**, *32*, 1927–1940.

(147) Ni Chonghaile, T.; Sarosiek, K.; Vo, T.-T.; Ryan, J.; Tammareddi, A.; Moore, V. D. G.; Deng, J.; Anderson, K. C.; Richardson, P.; Tai, Y.-T.; *et al.* Pretreatment Mitochondrial Priming Correlates with Clinical Response to Cytotoxic Chemotherapy. *Science.* **2011**, *334*, 1129–1133.

(148) Wang, X.; Zhang, X.; Huang, Z.; Wu, D.; Liu, B.; Zhang, R.; Yin, R.; Hou, T.; Jian, C.; Xu, J.; *et al.* Protons Trigger Mitochondrial Flashes. *Biophys. J.* **2016**, *111*, 386–394.

(149) Huang, Y.; Dong, X.; Liu, Y.; Li, L.-J.; Chen, P. Graphene-Based Biosensors for Detection of Bacteria and Their Metabolic Activities. *J. Mater. Chem.* **2011**, *21*, 12358.

(150) Brand, M. D. The Sites and Topology of Mitochondrial Superoxide Production. *Exp. Gerontol.* **2010**, *45*, 466–472.

(151) Tero, R.; Misawa, N.; Watanabe, H.; Yamamura, S.; Nambu, S.; Nonogaki, Y.; Urisu, T. Fabrication of Avidin Single Molecular Layer on Silicon Oxide Surfaces and Formation of Tethered Lipid Bilayer Membranes. *e-Journal Surf. Sci. Nanotechnol.* **2005**, *3*, 237–243.